Structural and Petrological Survey of Peridotite at Almklovdalen, Norway

Master`s Thesis in Geoscience

Johannes Vik Seljebotn

Department of Earth Science

University of Bergen

31. August 2016

Abstract

The Western Gneiss Region (WGR) HP-UHP metamorphic terrain is a part of the Baltic continental crust generated during the Gothian orogeny and re-mobilized during the Sveconorwegian and the Caledonian orogenies. During its geological evolution hundreds of m^3 to km^3 scale peridotite bodies were emplaced into the crustal gneisses. These peridotites represent subcontinental lithospheric mantle (SCLM) consisting dominantly of chromite-bearing depleted dunites and harzburgites occurring as E-W elongated massifs and lenses throughout the whole WGR. Discrete zones of eclogite, garnet pyroxenite and garnet peridotite occur within some of the peridotites and these zones are suggested to represent zones of Proterozoic refertilization or layered cumulates. The garnet-bearing assemblages and their retrograded equivalents are suggested to be genetically related to both each other and the depleted dunite in which they occur. Garnet-bearing assemblages and their retrograded equivalents provides kinematic indicators which are used to deduce deformation processes that affected the peridotite throughout its geological evolution. Extensive folding of these lithological elements which occur within a restricted field area are analyzed and related to processes of formation. Two competing models of emplacement differs in terms of age, provenance and time and process of emplacement. These models are by this survey tested against new structural and geochemical analytical results. The up-trusting model suggests Baltic provenance and emplacement during the Gothian orogeny. The sinking intrusion model suggests Laurentian provenance and emplacement during the Gothian orogeny. General mapping of the Almklovdalen peridotite and detailed mapping of selected field areas provide new geological maps of the of the entire massif and the selected area.

Acknowledgements

Special thanks to my supervisor Haakon Fossen, co-supervisor Rolf Birger Pedersen and other employees at The Institute of Earth Science, University of Bergen. Their excellent assistance, contribution and dedication have been commendable. The large proportions of inspiration and professional support provided by William L. Griffin, Suzanne Y. O`Reilly, Herman Van Roermund, Torgeir T. Garmo, Jan Kihle and Håkon Austheim was of essential importance. Support and professional assistance provided by co-supervisor Roar Sandøy at the SIBELCO Nordic office in Norway and staff at the SIBELCO Nordic plant at Åheim were also essential to the outcomes of the Master`s Thesis. Steinar Slagenes, Jermund Rekkedal, Mannie Mehu, Odd Westerås, Rolf Kristiansen, Marianne Storeide, Anders Bakkebø and Inge Hellebust deserves special thanks, but many other employees also provided important contributions. SIBELCO Nordic deserves a special thanks for providing me with a summer job. Terje Osnes which provided a place to stay during the summer of 2014 and Jetmund Gjesteheim which provided a place to stay during the summer of 2015 deserves great thanks for good service. I also want to thank my supportive family for their patience and inestimable help to complete five years of studies at UiB. Last but not least a special thanks to Eline Sandal for all her great support and friendship during the final stage of this Master` Thesis.

Table of Contents

1. Introduction

1.1 Aims of the thesis

This Master`s thesis has been formulated by the University of Bergen (UiB) in cooperation with the mining company SIBELCO. The aim of this project was to gain further practical and academic knowledge about the peridotite massif at Almklovdalen located near the village Åheim at Sunnmøre, Norway (Figure 1.1.1).

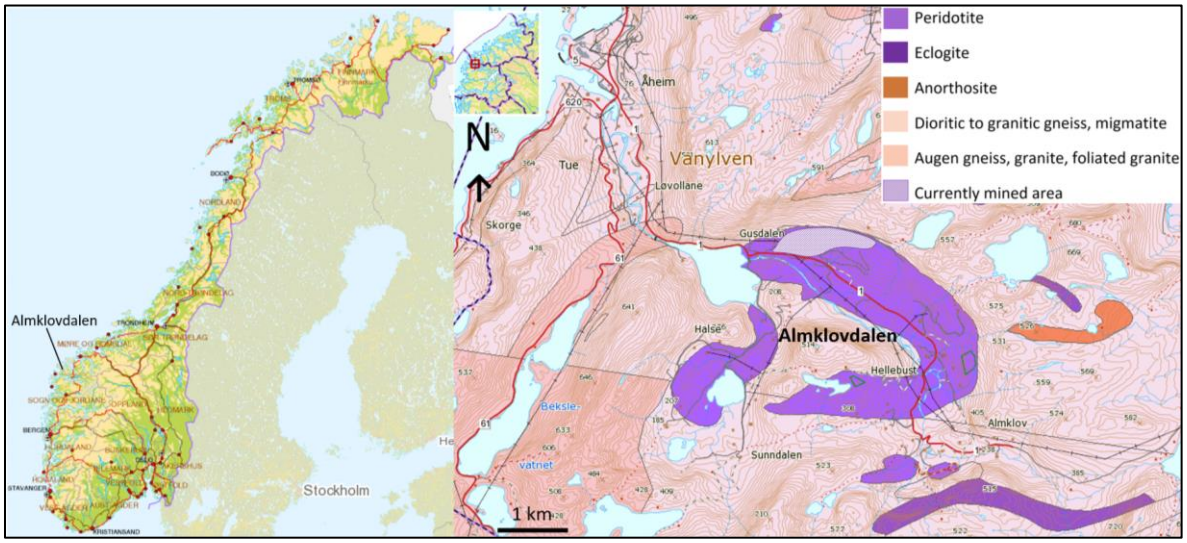

Figure 1.1.1: Geological map of the Almklovdalen area (http://www.norgeskart.no/#4/502779/7157838, accessed: 18.09.2015; http://geo.ngu.no/kart/berggrunn/, accessed: 18.09.2015).

The most important aim is to contribute to a better scientific documentation and understanding of the Almklovdalen peridotite and related peridotites in the Western Gneiss Region. The estimates of the timing of emplacement and the provenance of the ultramafic bodies vary widely among two competing models. Structural, mineralogical and geochemical research on selected localities provided by this Master`s Thesis will contribute to answering these questions, although a conclusive answer would require more in-depth research than can be provided in a thesis of this scope.

Another aim is to provide SIBELCO Nordic with information related to their commercial interests in olivine. SIBELCO Nordic is currently operating an open pit mine in the northern part of the massif, from which the company extracts approximately 2-3 million metric tons of olivine per year (Figure 1.1.1). A range of olivine-based products for various fields of application is exported worldwide. The most important applications of olivine are foundry sand and slag conditioner in metal production, refractory products, filler sand in metallurgical processes, heavy concrete additive, sandblasting materials, mineral wool, ballast for oil drilling platforms and covering of subsea pipelines. The latest products developed by SIBELCO Nordic at Åheim include sorbents in filter systems used for purifying water sources polluted by heavy metals and as capping material used to cover sediments polluted with heavy metals in hydrous, atmospheric and sub-surface environments. Predictable and stable access to olivine is essential for future innovation and development of new products. Better knowledge about the peridotite massifs from which SIBELCO Nordic extracts the raw material will therefore be an important contribution to product development and continued mining.

1.2 Specific problems

The specific problems addressed in this Master`s Thesis are:

- Can new lithological elements be found by field mapping of the peridotite at Almklovdalen which is suitable for research that potentially can produce new knowledge about geological processes within subcontinental lithospheric mantle?
- Why do compositional layering and deformation features in the selected field area near Helghornsvatnet deviate from those in the rest of the peridotite body?
- Is there a genetic relationship between the depleted dunites, the fresh garnet-bearing assemblages and the clinochlore layers/bands at the selected field area near Helghornsvatnet?
- What processes generated the garnet bearing assemblages and the clinochlore layers/bands at the selected field area near Helghornsvatnet?
- What relationship does the dunites and the garnet-bearing assemblages have relative to primitive mantle (PM)?
- What implications do the structural and geochemical evolution within the Almklovdalen have for the competing emplacement models?

2. Geological framework

2.1 The Western Gneiss Region (WGR)

The field area selected for this Master`s Thesis is located within the Western Gneiss Region and a general description of regional geological settings is provided in the first part of this section. The Western Gneiss region is abbreviated as WGR throughout the rest of this document.

The WGR represents the western continental margin of the Baltic shield and the deepest root zone of the Scandian mountain belt. A simplified illustrating the extent of the WGR Precambrian basement and relations to the allochthons and Devonian basins are provided in Figure 2.1.1. The Scandian phase represent the late phase of the Caledonian orogeny which occurred between 480-380 Ma; the Scandian phase extended from 425 to 380 Ma (Figure 2.1.3) (Hacker et al., 2010).

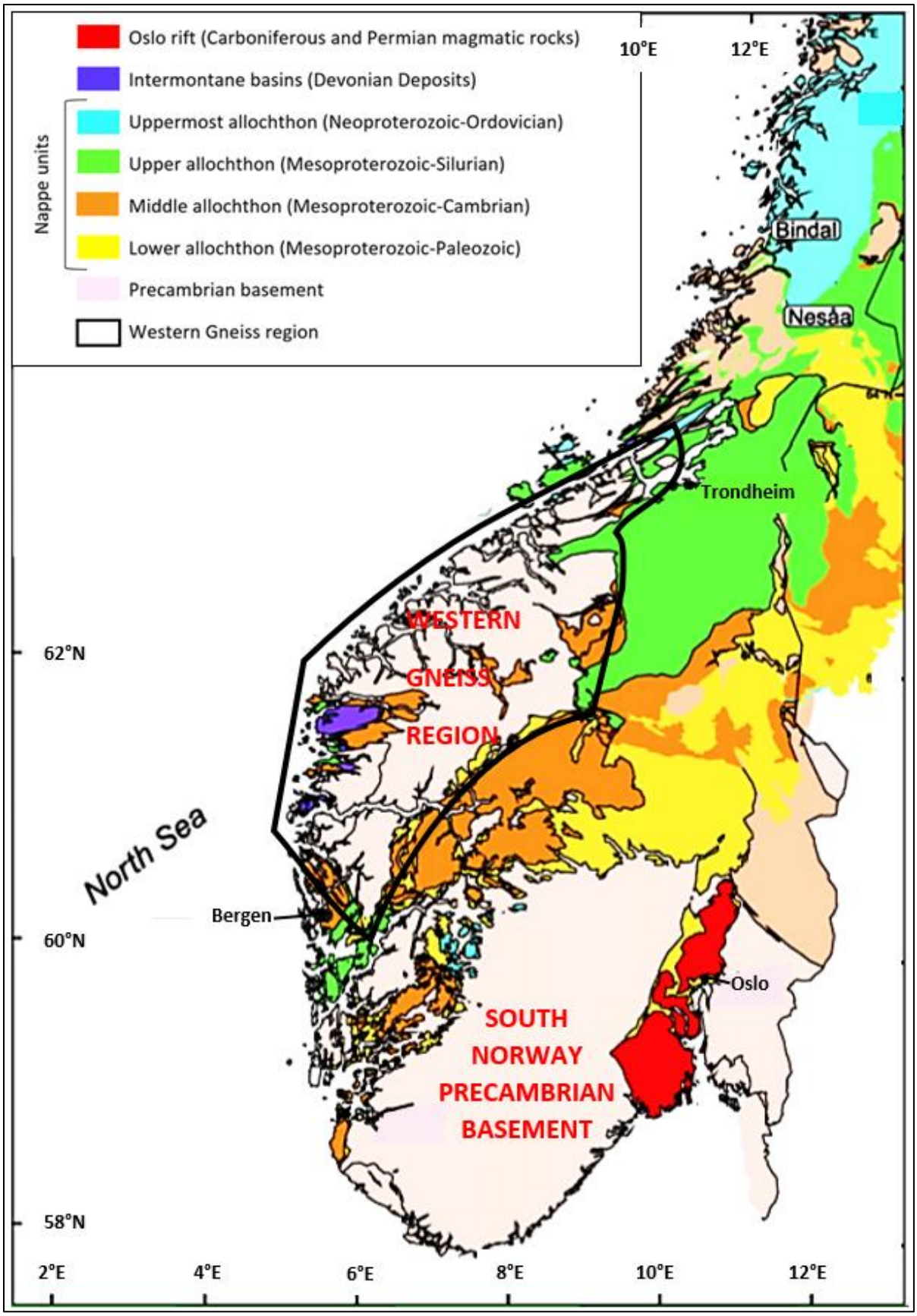

Figure 2.1.1: Simplified geological map of Southern Norway showing the extent of the WGR. (Modified from (Slagstad et al., 2011)).

The dominant rock types exposed in the WGR basement window are Proterozoic high-pressure (HP) to ultra-high pressure (UHP) quartzofeltspathic gneiss, migmatitic gneiss, augen gneiss, granitic gneiss, amphibolite, mangerite, anorthosite, eclogite, pyroxenite and peridotite. This Thesis is devoted to the peridotites and pyroxenites. Most of the autochthonus-parautochthonus crystalline rocks of the Baltic shield were originally generated during the Gothian orogeny (~1690-1620 Ma), overprinted and remobilized during the Grenvillian-Sveconorwegian orogeny (1100-950 Ma) (Fossen, 2010; Gordon et al., 2016) and finally strongly remobilized by the subduction of the Baltic continental crust beneath Laurentia during the Caledonian orogeny (480-380 Ma) (Hacker et al., 2010). Some granitic, gabbroic and anorthositic intrusions were emplaced into the WGR during the Sveconorwegian orogeny and represent minor volumetric contributions compared to the dominant Gothian basement rocks. A series of nappe units thrusted on to and folded into the basement rocks was emplaced during the Caledonian orogeny. The last major rock-forming event occurred during the Devonian when the wearing down of the Scandian mountain chain filled several intermontane basins with sediments. These sediments are today present as metasandstones and conglomerates. A chronological description of this geological evolution of the WGR is provided in this section. Figure 2.1.2 provides an overview of the major orogenies that effected the WGR and Figure 2.1.3 provides an estimate of pressure-temperature conditions during Grenvillian-Sveconorwegian, Caledonian orogeny and the Scandian phase of the Caledonian orogeny.

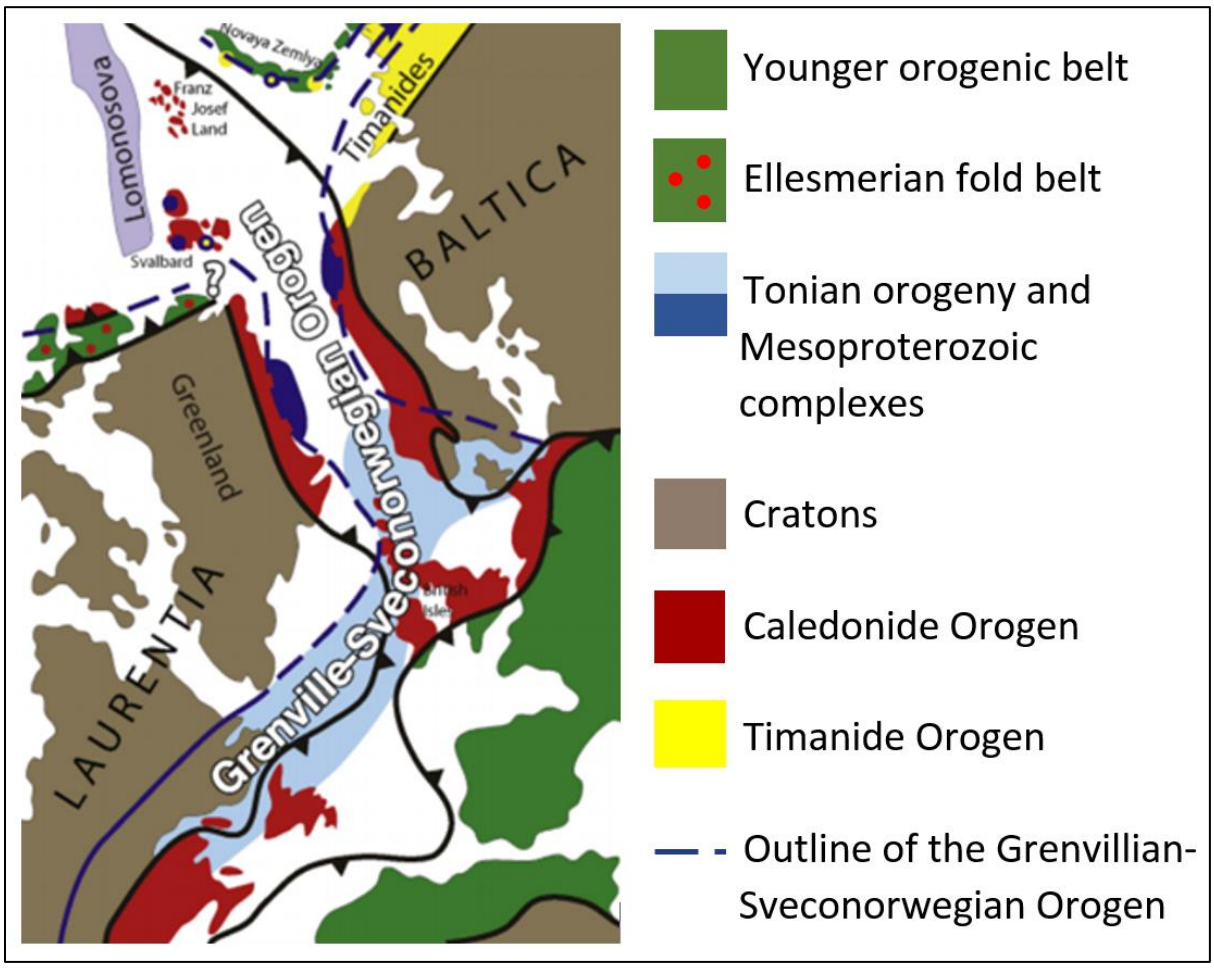

Figure 2.1.2: Overview map illustrating the extent of the Grenvillian-Sveconorwegian, Tonian, Timinide and Caledonian orogenies (Piñán Llamas et al., 2015).

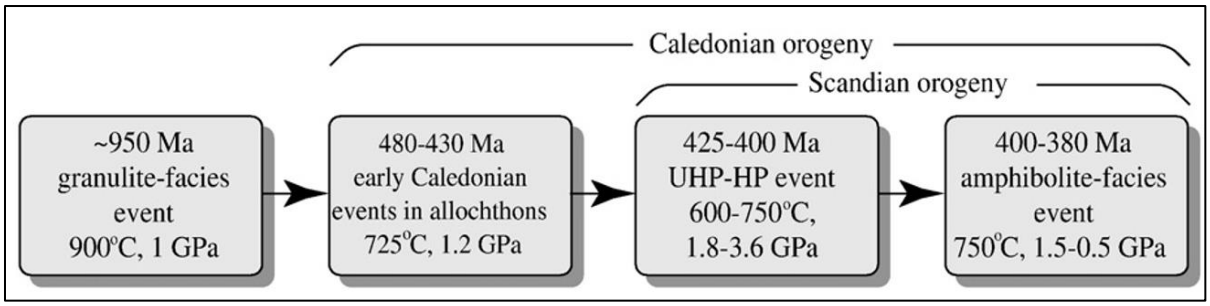

Figure 2.1.3: Estimates of pressure-temperature conditions during Grenvillian-Sveconorwegian, Caledonian orogeny and the Scandian phase of the Caledonian orogeny (Hacker et al., 2010).

Gothian orogeny

There are no presently described remnants of Archean crustal rocks or rocks that contain inherited Archean zircons in the WGR. U-Pb zircon ages representing bulk of orthogneiss protoliths are Gothian, ranging from 1.7-1.5 Ga and Sveconorwegian ranging from 1,2-0,9 Ga (Austrheim et al., 2003; Root et al., 2005; Root et al., 2004; SkÅr and Pedersen, 2003; Tucker et al., 1990; Tucker et al., 1987; Tucker et al., 2004). These works also detected minor groups of U-Pb zircon ages at approximately 1455 Ma and 1250 Ma. The crust-forming events during the Gothian and Sveconorwegian orogenies are confirmed by ages determined by Rb-Sr whole rock methods (Brueckner, 1972). Brueckner et al. (2010) states that zircon U-Pb ages from none of the crustal rocks in the WGR and Precambrian shield in SW Sweden exceeds 1850 Myrs with only one exception. This exception is a single zircon from a metapelite that gave a U-Pb age 2.1 Ga and is presently the oldest age found in zircons from the crustal rocks of Baltica (Beyer et al., 2012; Walsh et al., 2007). These age determinations indicate that the formation of the crust in this part of the Fennoscandic shield occurred during the Gothian orogeny with additional magmatic intrusions during the Sveconorwegian orogeny. Remobilization and deformation during later events has strongly overprinted structures and textures from the crust-forming processes. In early hypotheses related to emplacement of the peridotite bodies in the WGR it was suggested that they were thrust vertically from the Baltic lithospheric mantle into lower Baltic crust at the time of its formation (Carswell, 1968; Cordellier et al., 1981; Eskola, 1921; Lappin, 1966; Mercy and O'Hara, 1965a; Mercy and O'Hara, 1965b). This would imply a relatively long vertical transport through crustal rocks.

Grenvillian-Sveconorwegian orogeny

The Grenvillian-Sveconorwegian mountain chain developed by tectonic plate collisions west of the Fennoscandic shield as it appeared after the Gothian orogeny (Figure 2.1.2) (Ramberg et al., 2006). Peak metamorphism is estimated to be amphibolite to granulite facies (900°C, 1 GPa) at approximately 950 Ma (Figure 2.1.3) (Hacker et al., 2010). Regional tectonic events in this period were related to formation of the supercontinent Rodinia by collision of continental plates. (Ramberg et al., 2006) further states that an early stage of this event occurred in the Bamble-Kongsberg area by development of a collision zone and movement of the Bamble area towards the northeast along the Porsgrunn-Kristiansand shear zone, which caused high pressure-temperature metamorphic alteration of the Bamble rocks as they were thrust onto the Telemark area. During further evolution of this orogenic event, a large area was involved in the collision and experienced metamorphic alteration and deformation that seem to increase from the east towards west-southwest. The western part of the Baltic crust experienced high-grade metamorphism as its thickness increased and crustal blocks of Paleo to Meso-Proterozoic age were thrust sideways and sutured on to the Fennoscandic shield (Ramberg et al., 2006). A series of plutonic intrusions was emplaced into the area during

development of the mountain chain forming granitic and anorthositic massifs that make up the youngest component of the WGR basement rocks. The peak of the orogenic process is set at approximately 970 Ma (Ramberg et al., 2006) and the further evolution occurred in an extensional regime during break up of Rodinia. Breakup is suggested to have been triggered by a super plume underneath the South China Craton at approximately 825-800 Ma (Li et al., 1999) which resulted in opening of the Iapetus ocean approximately at 650-550 Ma (Cawood et al., 2001; Pisarevsky et al., 2008).

Caledonian orogeny

The development of a subduction zone along the Laurentian continental margin and possibly in an island arc setting triggered a contractional regime. This further caused the divergence that led to closure of the Iapetus ocean and development of the Caledonian orogeny (480-380 Ma) (Figure 2.1.3). During the closure of the Iapetus ocean a series of allochthonous nappe units was thrust on-to the autochthonous crystalline basement of the Baltic shield. These nappes derived from oceanic crust, micro-continents and island arcs that formed in the Iapetus ocean in addition to blocks of Laurentian and Baltic continental margin. The WGR is presently partly overlaid by remnants of these allochthonous nappe units, which are stratigraphically grouped into the lower-, middle-, upper- and uppermost allochthons (Figure 2.1.1) (Roffeis and Corfu, 2014). Each of these stratigraphic units consists of several individual nappes. A more detailed map of thrust nappes and their relation to other geological elements in south-west Norway is provided in Figure 2.1.4. A fifth autochthonous and para-autochthonous unit consisting of Archean (only in northern Norway) to Proterozoic Fennoscandian Baltic basement rocks and the sedimentary cover of Late-Proterozoic to Lower-Paleozoic sediments are also described (Roberts and Gee, 1985).

The lower allochthons consist of meta-sedimentary rocks derived from the Baltic margin before collision in addition to fragments of basement rock incorporated from the Baltic margin during thrusting (Andersen and Austrheim, 2008; Roberts and Gee, 1985). The Middle Allochthon consists of Proterozoic crystalline complexes partly unconformably covered by Late Proterozoic to Lower Paleozoic metasediments from the Iapetus ocean (Andersen and Austrheim, 2008; Roberts and Gee, 1985). These workers further state that the crystalline complexes are stacked by thrusting, and rift-related magmatic dyke swarms of late Proterozoic age are found locally in the nappe unit. Andersen and Austrheim (2008) describe Caledonian granitoids related to intrusions during the Scandian collisional event in the Jotun nappes and Bergen arcs. The crystalline rocks in the Middle Allochthon are described as remains of micro continents, shallow basement columns or fragments of the Baltic continental margin (Ramberg et al., 2006). The upper allochthons consist of a wide selection of rocks types with large compositional variation, which has been exposed to various degrees of alteration and deformation. The dominating elements in the upper allochthons are ophiolites and island arc complexes of Ordovician to Early Silurian age (Andersen and Austrheim, 2008; Roberts and Gee, 1985). Other elements described in these publications are Precambrian gneisses, metasedimentary rocks, amphibolites and partly eclogitized mafic dikes and volcanic rocks, partly derived from the rifted Baltic continental-oceanic transition. The uppermost allochthons contain oceanic crust, meta-volcanic rocks and meta-sedimentary rocks (http://geo.ngu.no/kart/berggrunn/) derived from the Laurentian eastern margin or proximate micro-continents (Ramberg et al., 2006). Major parts of these nappe units are present in northern Norway. Middle Ordovician batholitic intrusions are wide-spread in the complex and the Tromsø region contains Ordovician eclogite-facies rocks (Andersen and Austrheim, 2008; Roberts and Gee, 1985).

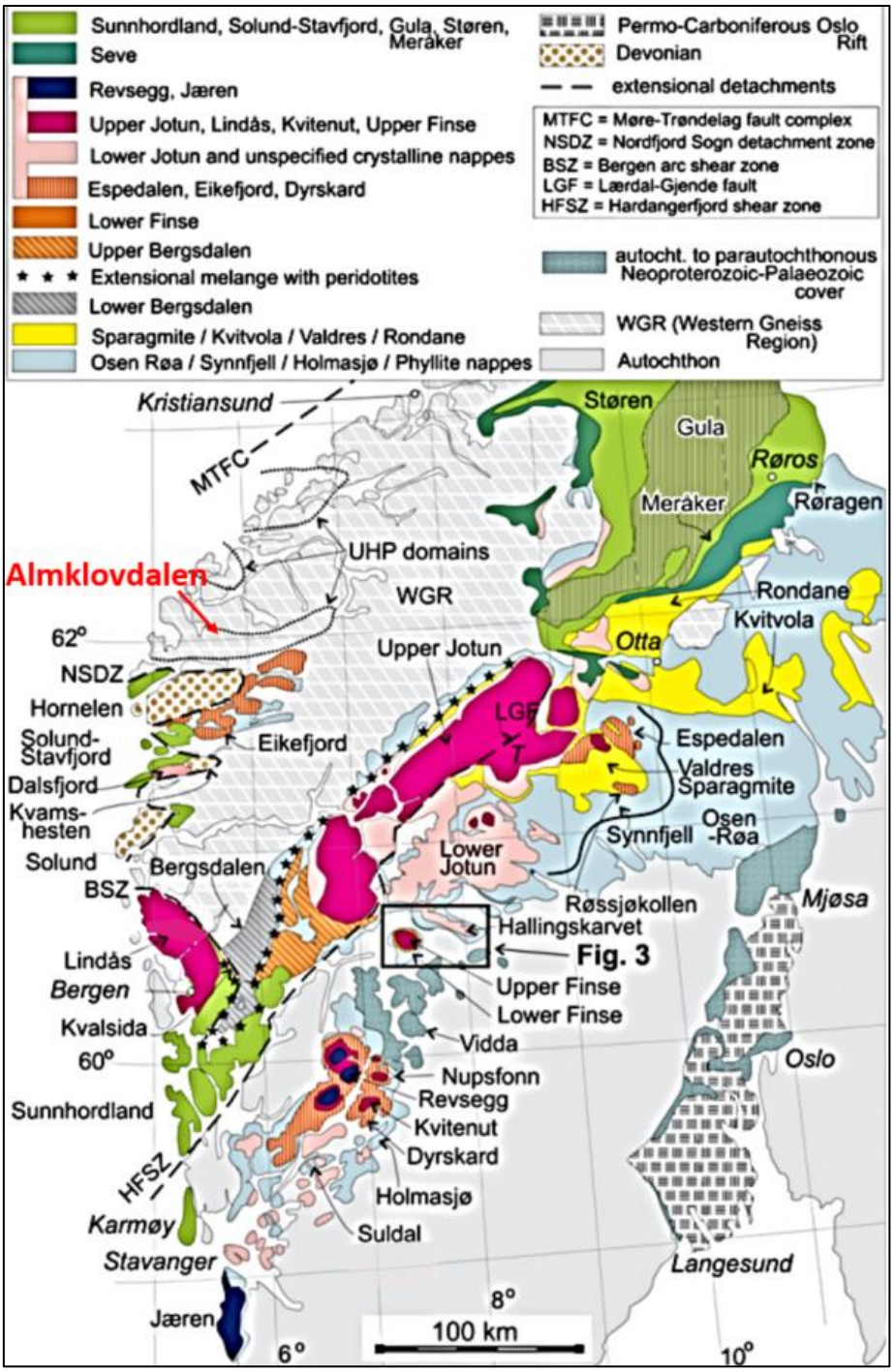

Figure 2.1.4: Stratigraphic map of tectonic units in South-West Norway including the UHP domains in the WGR (Roffeis and Corfu, 2014). The location of Almklovdalen is indicated in red.

Baltica and Laurentia collided during the early Scandian phase and during this continent-continent collision the light western part of the Baltic continental margin was subducted underneath Laurentia to a depth of more than 120 km. This was possibly a consequence of a slab-pull effect from previously subducted heavier oceanic crust and subsequent delamination of the oceanic crustal slab is suggested to have caused the following eduction and exhumation of the Baltic continental margin (William L. Griffin, pers. comm. 15.08.16). The following polyphase metamorphic evolution includes prograde metamorphism during the subduction event, minor retrograde metamorphism during eduction and exhumation of the continental slab generated the present-day mineralogy and texture

of the WGR. An interpretation of the Late- to post-Caledonian orogenic evolution is presented in Figure 2.1.5. Structural elements that formed by deformation during these conditions include lineation, foliation and microscopic to mesoscopic folds, shear- and fault zones. Boudinage is widespread at all scales and eclogite-facies boudins are important indicators of fluid-related metamorphism. A diagram illustrating the estimated pressure-temperature path during the Caledonian subduction event is provided in Figure 2.1.6. Estimated peak metamorphism is amphibolite- to granulite facies in (600-750°C, 1,8-3,6 GPa) at approximately 425-400 Ma (Hacker et al., 2010). PT conditions in the WGR increases from the south to the north and are estimated to have been approximately 3.2 GPa and 700°C in the Almklovdalen area (Figure 2.1.7.). Local eclogite-facies rocks are widespread through the WGR and are mainly linked to metasomatism. Shear and fault zones provide the porosity and connectivity sufficient for fluids to circulate. Eclogite-facies rocks are dominantly found within such settings surrounded by granulite-facies lithologies. Scandian-eclogite facies structures derived from an early brittle to late ductile regime deformation are dominated by ductile lineation, foliation and folds (Andersen et al., 1994; Hacker et al., 2010). Amphibolite-facies structures such as ENE-WSW to ESE-WNW lineation and isoclinal parallel folds are dominant and reflect a coaxial strain history (Andersen et al., 1994). The protoliths of the eclogite are suggested to be felsic gabbroic to anorthositic intrusives and mafic layered intrusions (Håkon Austrheim, pers. comm. 15.08.16).

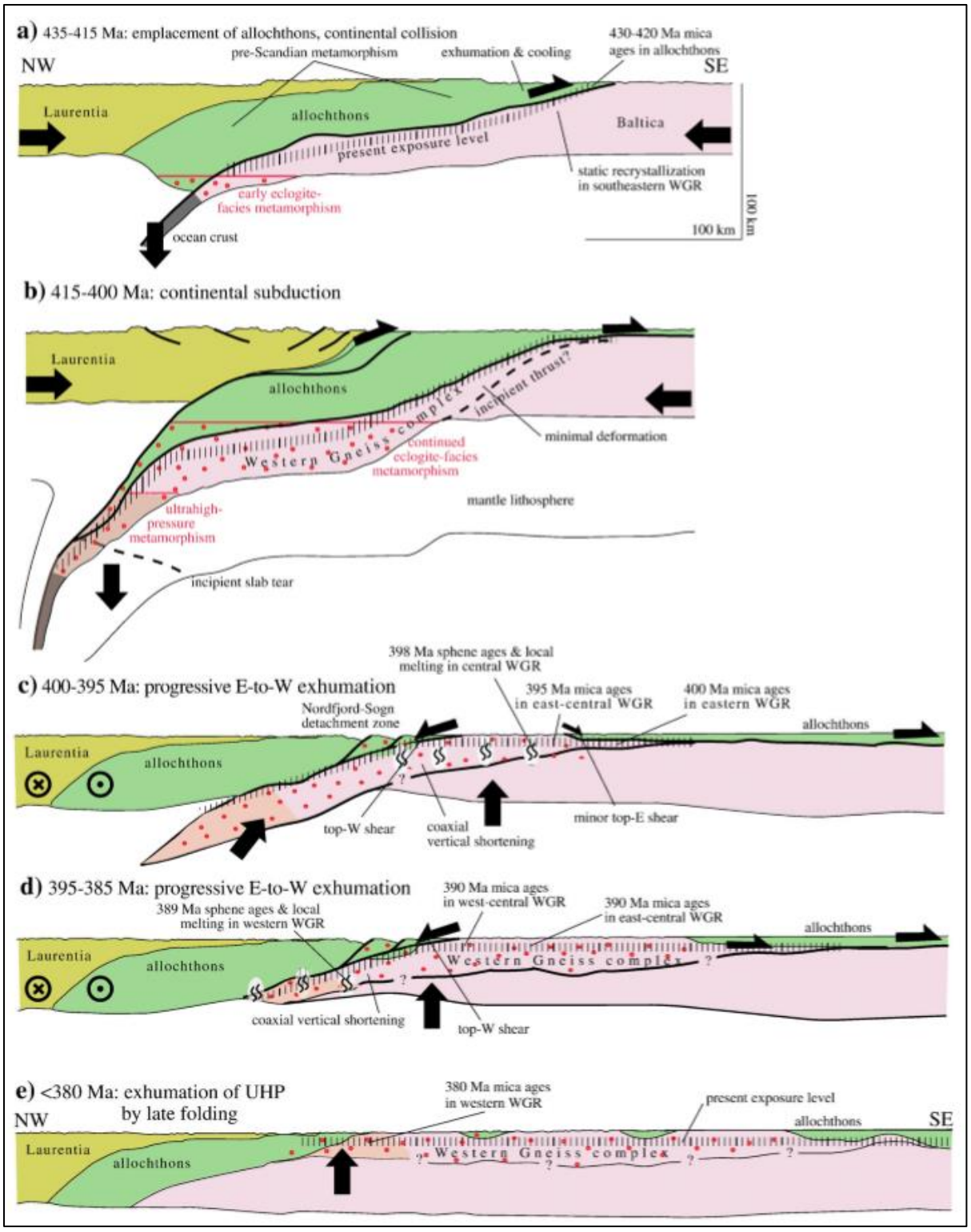

Figure 2.1.5: Evolution of the Caledonian to post-Caledonian orogenic event, as interpreted by Hacker et al., 2010. a) Allochthonous nappe units were emplaced onto the Baltic continental margin during collision with Laurentia. b) Baltic continental margin including the overlying allochthonous nappe units were subducted underneath the Laurentian continental plate to ultrahigh pressure conditions. c) and d) Extension-related exhumation triggers decompression melting and cooling, first in the east then propagating towards the west. e) Cooling of ultrahigh pressure domains to temperatures below 400°C occurred after 380 Ma.

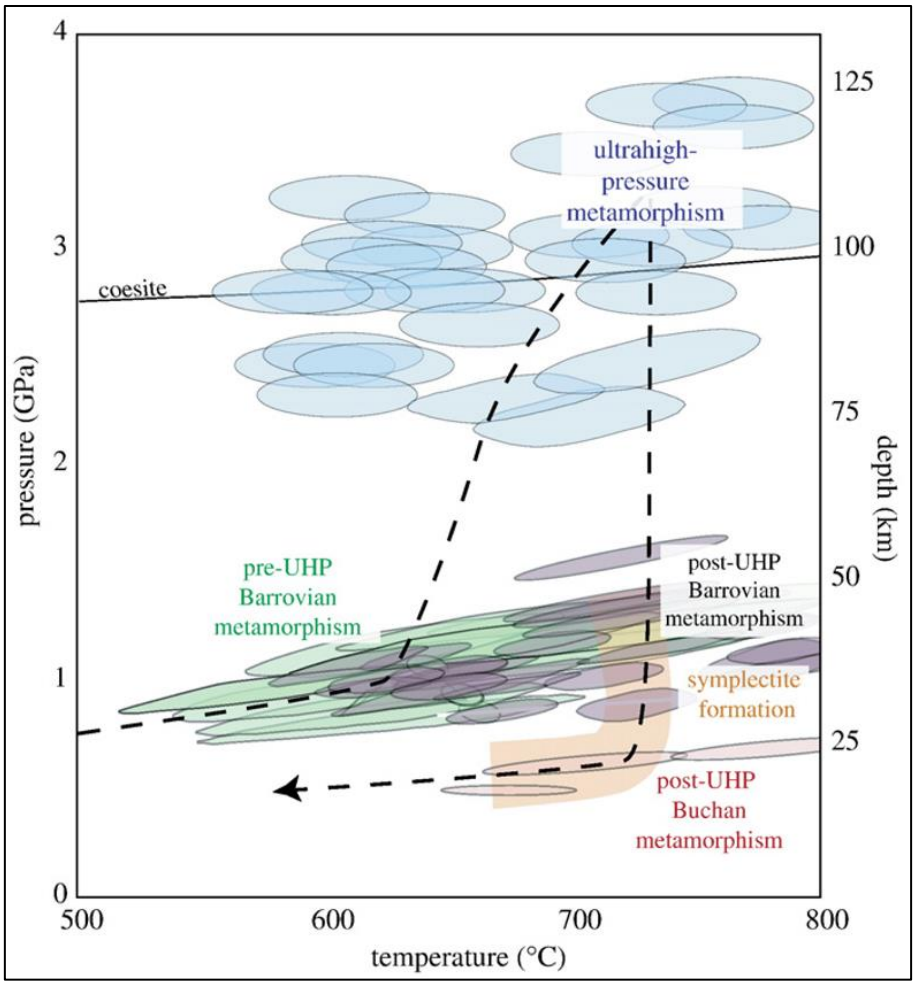

Figure 2.1.6: Diagram illustrating the estimated pressure-temperature path of polyphase metamorphic evolution during the Caledonian subduction event (Hacker et al., 2010).

The WGR contains approximately 5000 km^2 of ultrahigh-pressure terrain (UHP) which is surrounded by approximately 30 000 km^2 of high-pressure (HP) terrain, both generated by Caledonian-Scandian orogenic processes (Hacker et al., 2010). This is the best exposed UHP terrain worldwide. Hacker et al. (2010) divided the UHP terrains into four separate domains described as the Nordøyane-, Haram-, Sørøyane- and Nordfjord domains (Figure 2.1.7). Others consider only the Nordøyane, Sørøyane and Nordfjord domains as UHP terrains (van Roermund, 2009). During peak metamorphism these domains were in the stability fields of coesite which is an important indicator of these conditions. Pseudomorphs after coesite can be found in eclogite-facies rocks throughout the UHP domains (Brueckner, 1998; Roermund, 1998). Majoritic garnets (Van Roermund et al., 2001) and microdiamonds (Brueckner, 1998; Dobrzhinetskaya et al., 1995; Roermund, 1998; Spengler et al., 2009; van Roermund et al., 2002; Vrijmoed et al., 2006; Wain, 1997) are further important mineralogical evidence of UHP pressure-temperature conditions and are found in the garnet-bearing assemblages within the Nordøyane UHP domain. Spengler et al. (2009) estimated peak UHP metamorphism in garnet-bearing assemblages in the Nordøyane UHP domain to have reached 6.3 GPa and 870° at 429.5±3.1 Ma. The WGR UHP domains are suggested to represent the cores of large-amplitude east-west-trending antiformal folds formed during a north-south deformation event. Such an event explains the outcrop patterns of the UHP domains, which are further suggested to occur as a continuous layer at depth (Young et al., 2007). The field area at Almklovdalen selected for this

Thesis is part of the Nordfjord UHP domain and is located approximately at the 3.2 GPa isobar and the 700°C isotherm on the map in Figure 2.1.7.

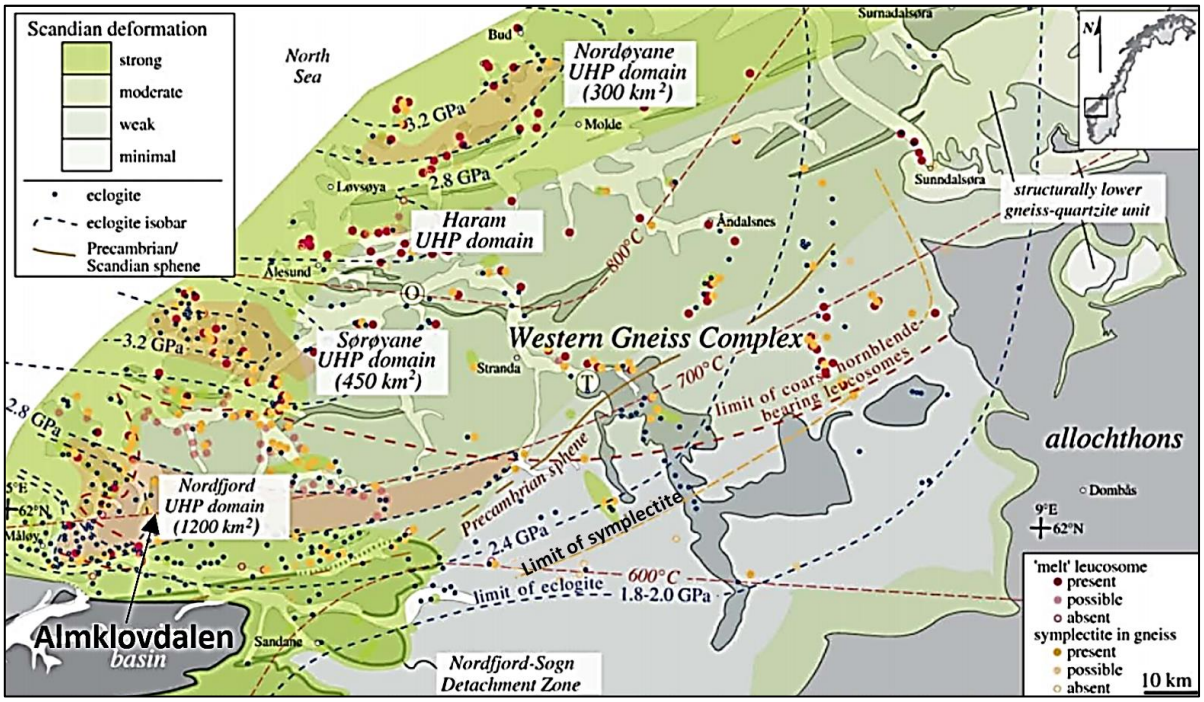

Figure 2.1.7: Map of the WGR defining the Caledonian ultrahigh-pressure domains and the surrounding high-pressure terrain (Hacker et al., 2010).

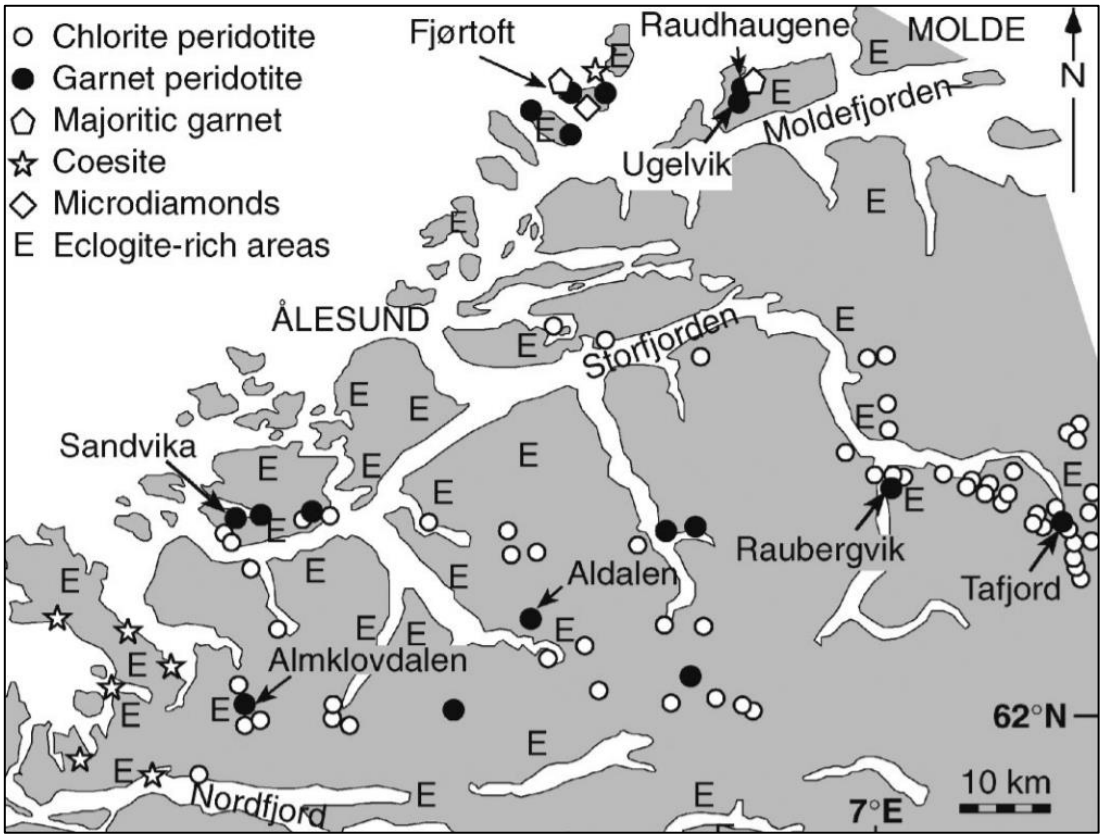

Figure 2.1.8: Simplified map of the WGR basement window illustrating the distribution of ultramafic rocks and eclogites (Beyer et al., 2004).

More than a hundred peridotite bodies and lenses from m^3 to km^3 in size are widely distributed through much of the WGR basement window (Figure 2.1.8). The peridotites consist dominantly of dunite and harzburgite which in restricted areas contain garnet-bearing assemblages such as garnet pyroxenites, garnet peridotites and eclogites. Individual garnet-free pyroxenites are also present in the gneiss but are rare compared to the olivine-rich varieties.

In recent publications it is suggested that the peridotite bodies in the WGR represent fragments of Laurentian subcontinental mantle, derived from the mantle wedge in the lower part of the hanging wall during the Caledonian continental subduction event (Beyer et al., 2004; Beyer et al., 2012; Beyer et al., 2006; Brueckner, 1998; Brueckner et al., 2010; Cuthbert et al., 1983; Medaris Jr, 1984; Van Roermund et al., 2001; Wang et al., 2013). The emplacement mechanism is suggested to be sinking intrusion of peridotite blocks from the hanging wall into subducted continental slabs by both mechanical and ductile processes. This hypothesis implies that relics of subcontinental mantle are exposed on the surface due to eduction and exhumation of the Baltic margin from a deep section of the subduction zone. A schematic illustration of the sinking intrusion model is provided in Figure 2.1.9.

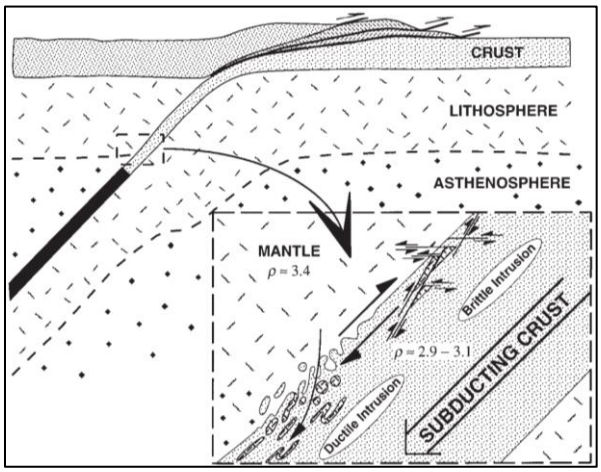

Figure 2.1.9: Schematic illustration of the sinking intrusion model (Brueckner, 1998).

Evidence of this complex structural deformation history is preserved throughout the WGR. All lithologies were remobilized and deformed to a certain degree during the Caledonian orogeny. Proterozoic igneous elements presently outcrop as relatively sparsely to strongly deformed anorthosites, granitoids and granitic gneisses (Austrheim and Griffin, 1985). The field area at Almklovdalen is located just north of and in proximity to the west-dipping Nordfjord-Sogn detachment zone, an amphibolite- to greenschist facies monolithic shear zone. This shear zone was formed by top-to-west shearing in an extensional regime that developed during the eduction and exhumation that followed peak Caledonian orogenic convergence (Andersen and Jamtveit, 1990; Hacker et al., 2010; Norton, 1987). This late Caledonian event gradually overprinted earlier textures and the present deformation features in the WGR are dominantly associated with coaxial east-west stretching. Dominant strain orientations represented by reconstructed trajectories for high temperature lineation and foliation during Caledonian orogeny are illustrated in Figure 2.1.10.

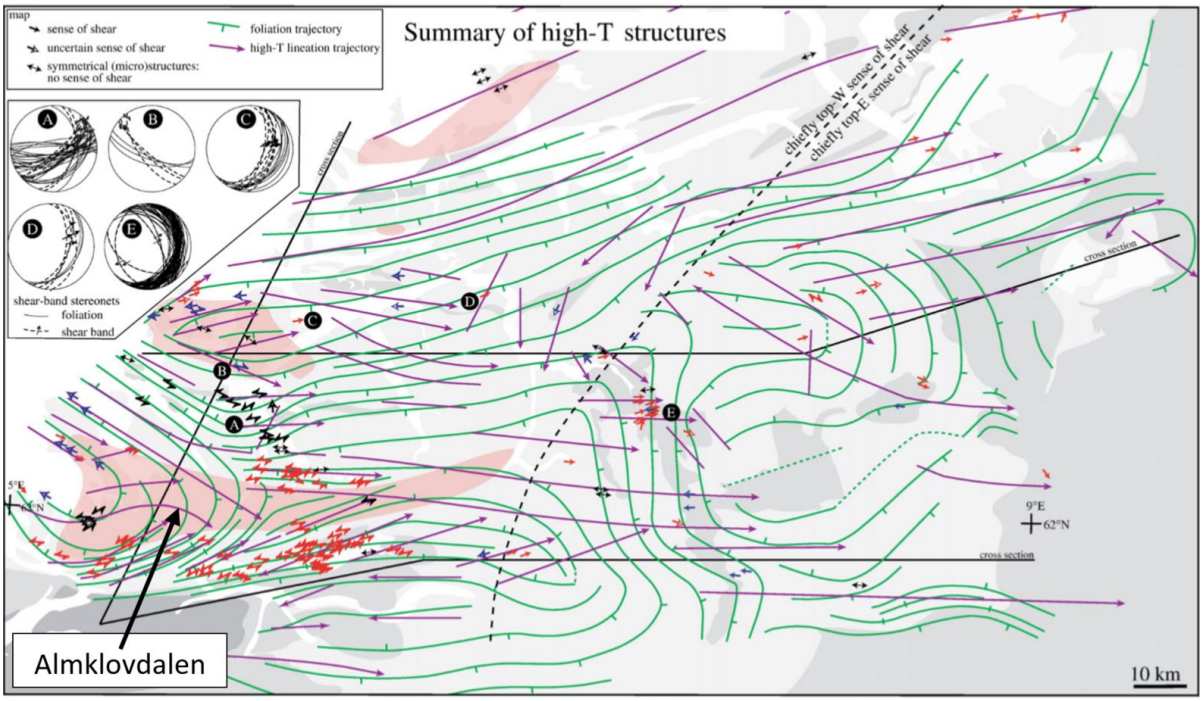

Figure 2.1.10: Dominant strain orientation represented by reconstructed trajectories for high temperature lineation and foliation during the Caledonian orogeny. This reconstruction was conducted by Hacker et al., 2010 by using previously published data (Barth et al., 2010; Chauvet and Seranne, 1989; Labrousse et al., 2002; Robinson, 1995; Terry and Robinson, 2003).

The weathering and wearing down of the Caledonian mountain chain covered parts of the westernmost WGR with sedimentary basins during the middle to late Devonian (393-359 Ma). Lithified and metamorphosed sediments from this last major rock-forming event generated sheets of meta-sandstone and conglomerate resting on sections of the thrust nappes. Exhumation continued in varying climatic conditions from late Devonian-early Carboniferous to present day. The cyclic glaciations during the last 2.6 Myrs enhanced the weathering and erosional processes to form the rugged present day topography of Scandinavia, including the WGR.

2.2 The field area

The location of the field area is indicated in the regional overview map provided in Figure 2.2.1.

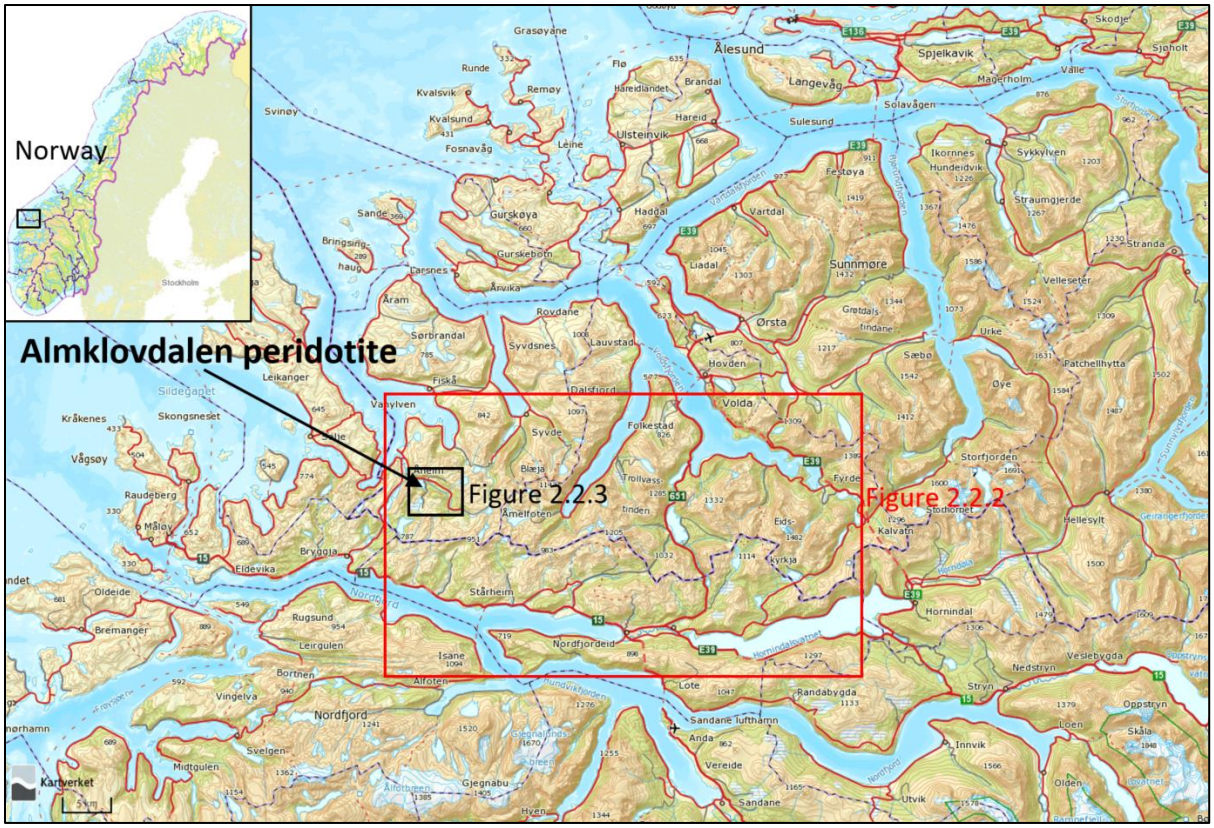

Figure 2.2.1: Regional overview map where the field area is indicated (http://www.norgeskart.no/#8/39258/6913899, accessed: 22.10.2015).

The two largest exposed peridotite bodies in the WGR are located along a large-scale shear zone at the northern limit of the Nordfjord-Sogn detachment zone (NSDZ) (Figure 2.1.4). A geological map showing their location, extent and field relation is provided in Figure 2.2.2. Geological mapping of this area has only been done at surface levels and large scale peridotite massifs may exist at deeper subsurface levels. The western of these two large peridotite massifs is the Almklovdalen peridotite which was selected as field area for this Master`s Thesis (Figure 2.2.3). The Thesis is devoted to the peridotite massif but some relevant data and observations from the contact zone within the adjacent gneiss are also presented. This choice was made due to the large naturally well exposed outcrops and the areas exposed from more than 50 years of continuous open pit mining activity within the peridotite. In addition, the Almklovdalen peridotite is the most studied ultramafic massif in the WGR. The large quantities of data available from previous research conducted both by the mining company and independent researchers provide a valuable theoretical fundament for further investigations. These data in addition to results and hypotheses presented in previous works will be further evaluated in this Master`s Thesis.

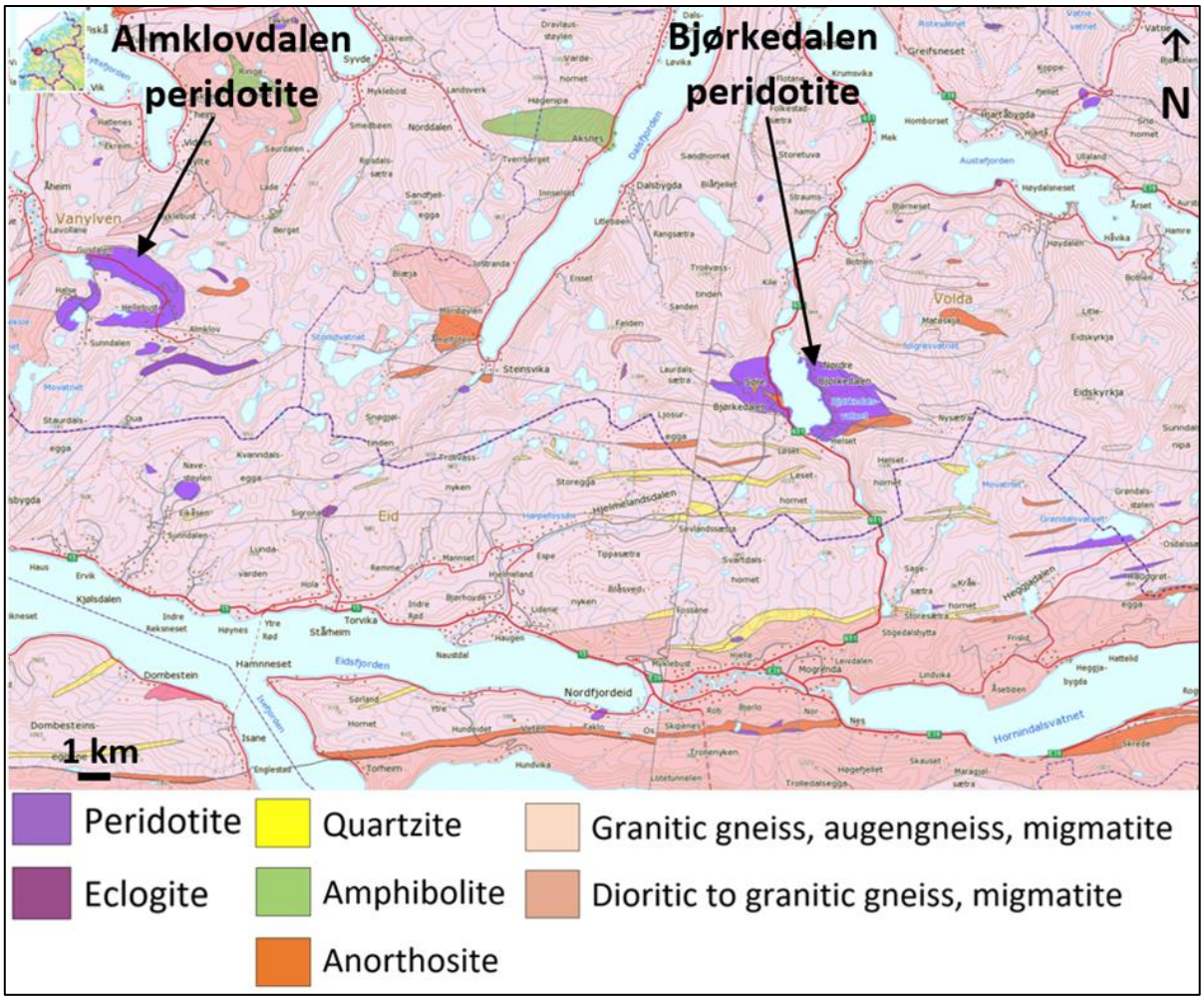

Figure 2.2.2: Geological map of the two largest peridotites in WGR illustrating geological context (http://geo.ngu.no/kart/berggrunn/, accessed: 13.10.2015).

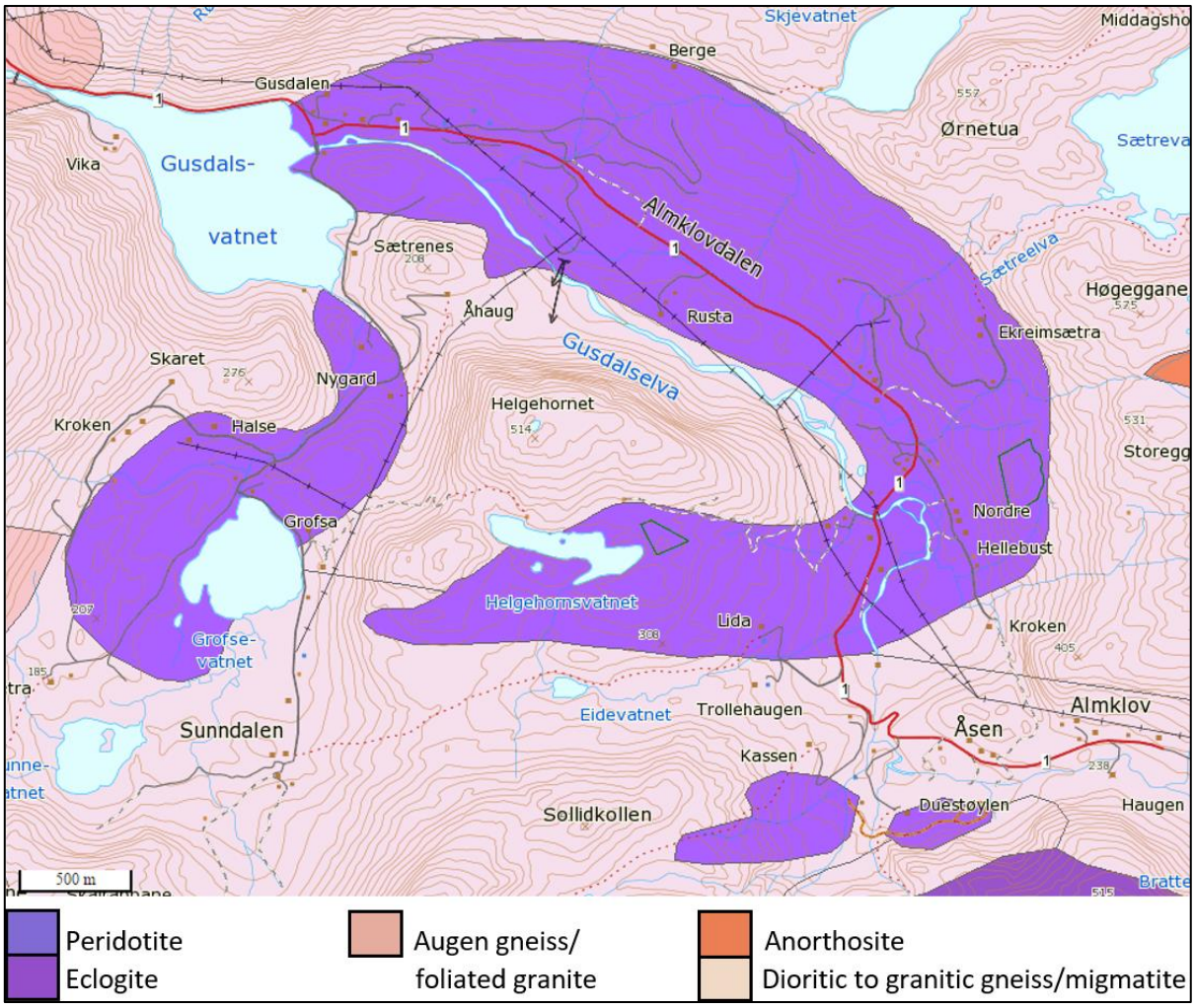

Figure 2.2.3: Geological map of the peridotite massif as it presently occurs in the geological map series from the Norwegian Geological Survey (NGU) (http://geo.ngu.no/kart/berggrunn/, accessed: 17.10.2015).

The entire peridotite massif (Figure 2.2.4) was investigated during fieldwork in order to construct a detailed geological map of its extent and contacts against the surrounding lithologies. Knowledge of the diversity of geological elements was essential to locate the most ideal area for research related to the aims and specific problems in this Thesis. The Almklovdalen peridotite contains a wide range of ultramafic and mafic rocks types which are well exposed due to the sparse vegetation cover and the extensive mining activity. The accessibility of large surface area and vertical profiles in the open pit mines makes the field area ideal for geological research.

The field area for detailed mapping internally in the peridotite massif represents selected outcrops containing geological elements that differ from those generally found in the massif. These selected outcrops are restricted to an area located near Helghornsvatnet (location 6 in Figure 2.2.4, Figure 2.2.5 and Figure 2.2.6 (these maps are constructed as part of this Master`s Thesis)). Samples from this area were compared to samples from locations within the Gusdal mine (location no. 1-5 in Figure 2.2.4). Outcrops within the Helghornsvatnet area are sparsely exposed to surface weathering, sparsely covered by sediments and vegetation (Figure 2.2.5) and contain a compositional layering that differs from the rest of the Almklovdalen peridotite massif. Mineralogical alteration varies extensively within a relatively small area and the lithological elements within this area are of significant importance for research on this peridotite body.

Throughout the WGR there are also ultramafic rocks that contain different and/or distinct geological elements compared to the peridotite at Almklovdalen, which indicates that they may not have been exposed to the same geological evolution. This could also indicate different provenance and emplacement processes of some ultramafic rocks, so that results from research done on the Almklovdalen peridotite may not represent all ultramafic rocks in the WGR.

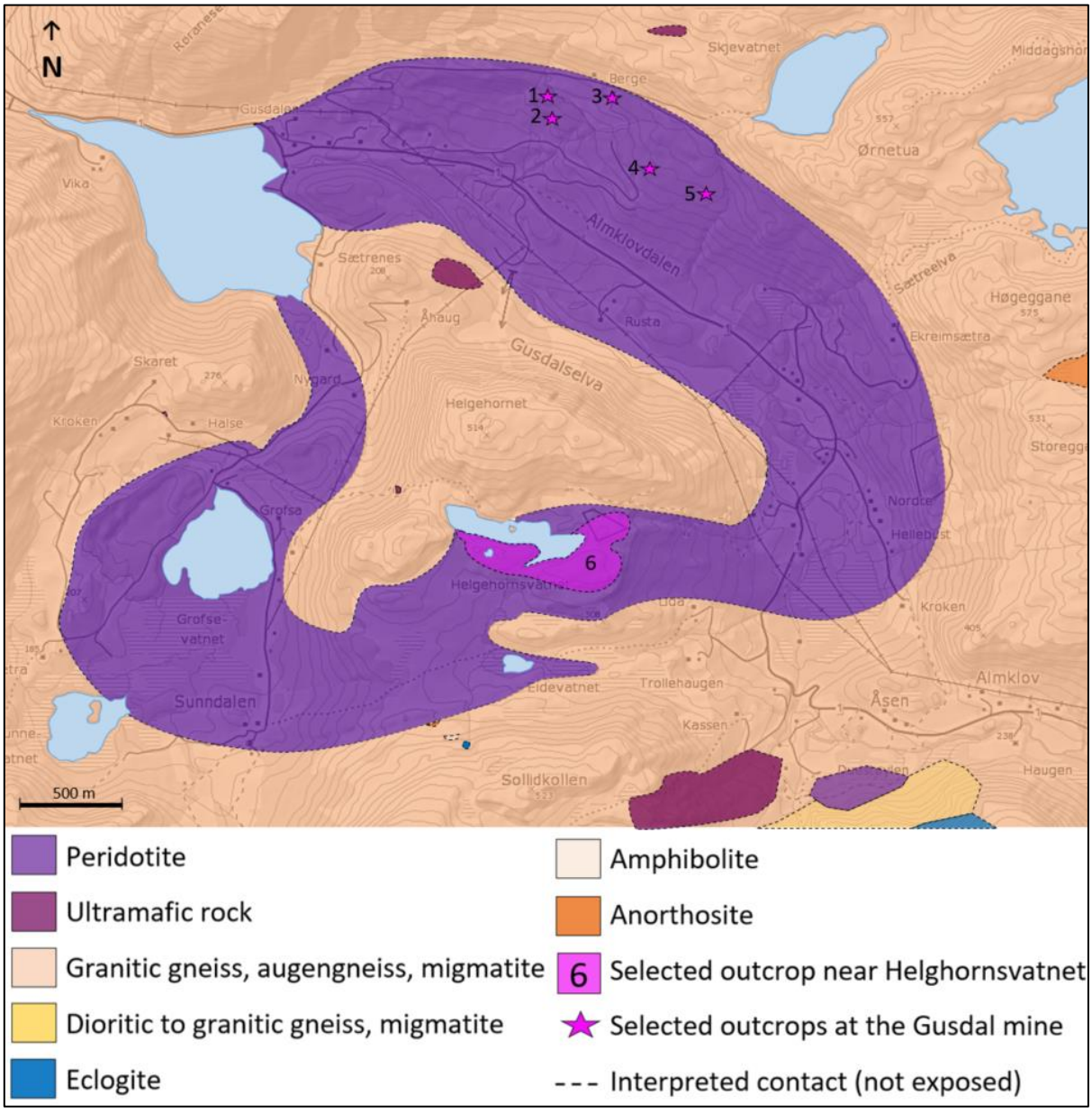

Figure 2.2.4: Geological map of the Almklovdalen peridotite massif constructed from field observations and field data collected during fieldwork conducted for this Thesis. The areas selected for detailed survey are marked by number 6 and sample locations in the Gusdal mine are marked by the numbers 1-5.

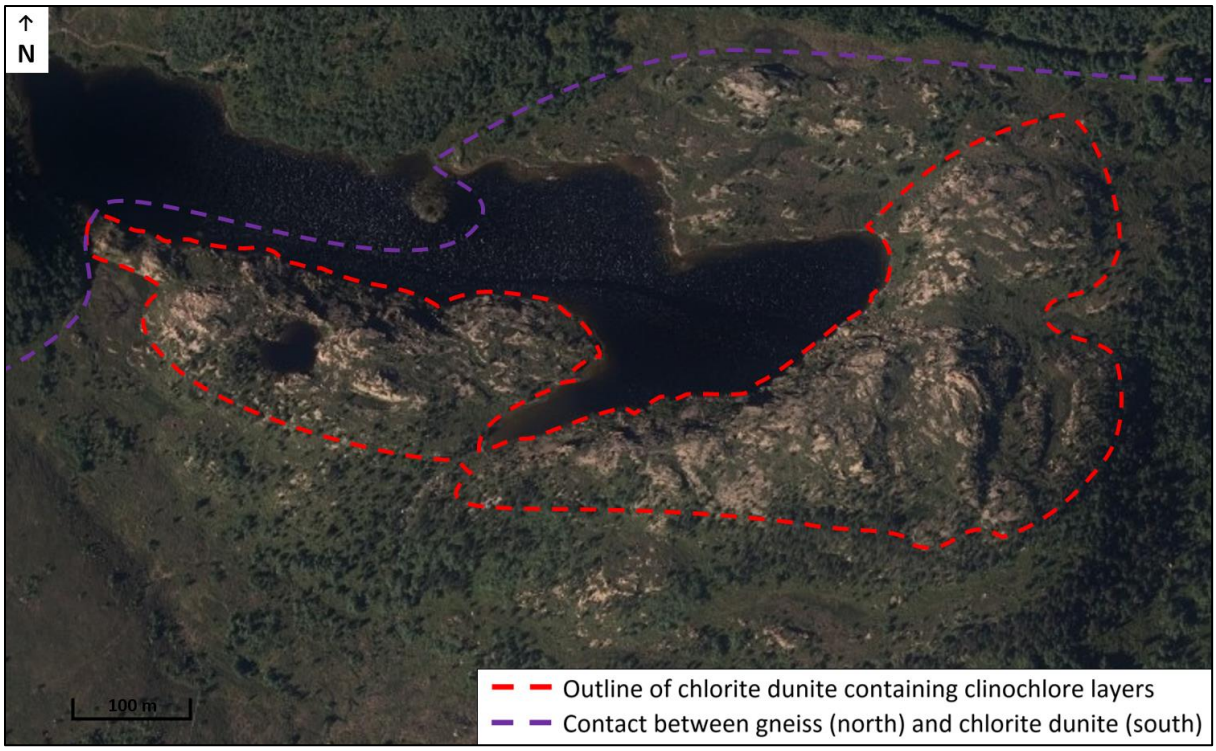

Figure 2.2.5: Aerial photo showing the outline of selected field area near Helghornsvatnet (red line) and extent of vegetation and sediment cover within the area (http://www.norgeskart.no/#15/9210/6910009/-land/+flybilder, accessed: 20.03.2016).

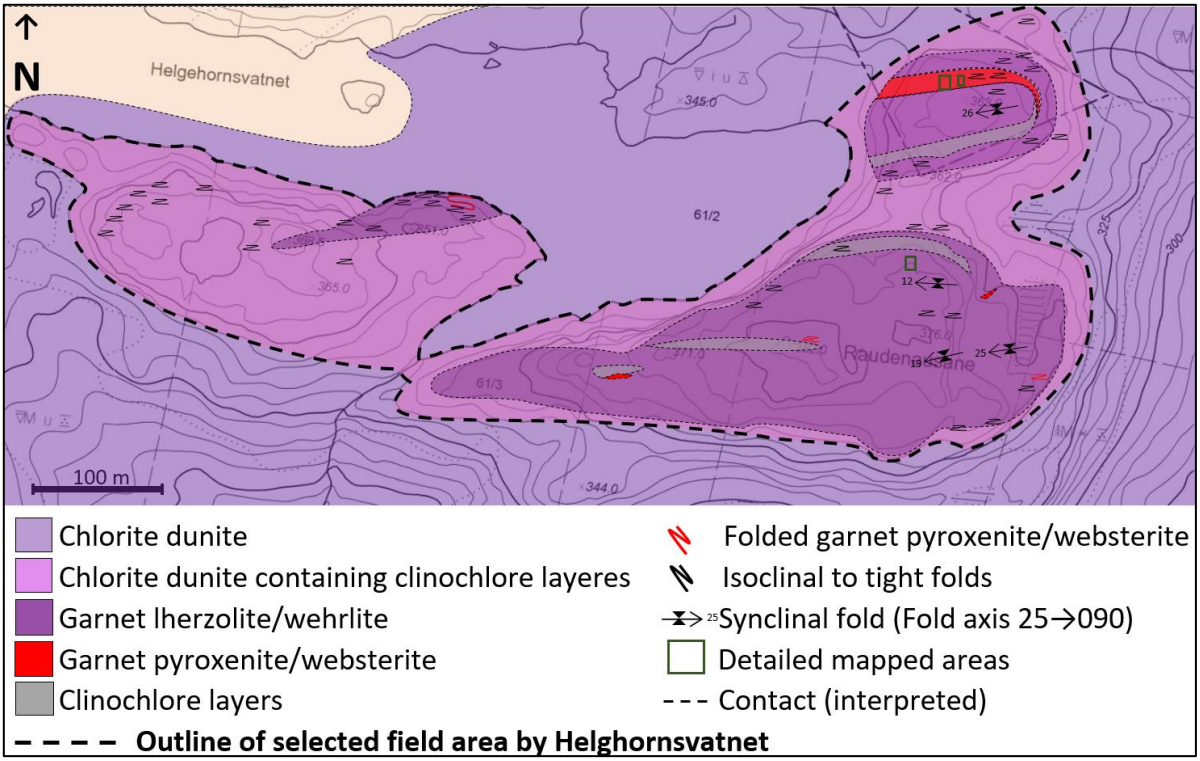

Figure 2.2.6: Geological map illustrating the selected field area near Helghornsvatnet constructed as part of this Thesis.

3. Theoretical background

Peridotite is a relatively coarse-grained ultramafic rock type that contains less than 45% silica. It derives from the upper mantle and is divided into the four rock types lherzolite, harzburgite, dunite and wehrlite. Classification of peridotite (>40% olivine) into these four varieties is done according to chemical composition using a ternary diagram with the endmembers clinopyroxene, orthopyroxene and olivine (Figure 6.2.1). This diagram also includes pyroxenites and websterites (<40% olivine). Olivine is a major component in ultramafic rocks and the dominant mineral in the upper mantle down to approximately 400 km depth where olivine is converted to its higher-pressure polymorph wadsleyite. Lithospheric and asthenospheric mantle are the main sources of peridotites. Layered igneous complexes, basaltic and komatiitic volcanic lavas, ophiolites, xenoliths in kimberlites and mantle fragments exposed by orogenic processes are the geological elements in which peridotite are exposed at crustal levels. The main mineral components additional to olivine are calcic-plagioclase, garnets, spinel/chromite, orthopyroxenes, clinopyroxenes and their retrograded equivalents. Chemical composition reflects the processes that were active during formation. These processes are partial melting, causing melt extraction from the upper mantle, or fractional crystallization, forming crystal cumulates during cooling of magma reservoirs.

Subcontinental lithospheric mantle (SCLM) extends to far greater depths than the sub-oceanic lithospheric mantle (SOLM). The bulk composition of SCLM is suggested to reflect the tecthonothermal age of the overlying continental crust and depletion occur by progressive partial melting and removal of basaltic components. (Griffin et al., 1998; Griffin et al., 1999; Griffin et al., 2009). Highly depleted Archean orogenic massifs in the WGR are by Griffin et al. (2009) suggested to be equivalents to SCLM beneath cratons. Refertilization of Archean SCLM by metasomatic enrichment in basaltic components is further suggested to explain the SCLM composition underneath Proterozoic shields. Viscosity and buoyancy contrasts between Archean and Proterozoic SCLM may have an important role in the generation, preservation and recycling of continental crust (Griffin et al., 2009). To gain further knowledge about the tectonic and genetic relation between mantle and crustal rocks it is essential to understand the geodynamic effects of lateral differences in the physical properties and composition of SCLM. Orogenic peridotite massifs in the WGR, especially the large well-exposed peridotite at Almklovdalen, are of crucial importance for further research on the role of SCLM properties during formation and evolution of the crust. Knowledge about how natural resources are generated during these processes will be important for future access to Platinum Group Elements (PGE), Rare Earth Elements (REE), chromite, nickel and olivine.

4. Previous research

Hypotheses and relevant results from structural, geochemical, geochronological, petrological and mineralogical research conducted on the Almklovdalen peridotite will be presented in this chapter.

4.1 Early work

Scientific research on the peridotite at Almklovdalen was started by pioneers in geology such as Victor Moritz Goldschmidt (1888–1947) and Pentti Eelis Eskola (1883–1964) during the early 19th century. They laid the foundation for groundbreaking work on ultramafic rocks and the development of petrology, geochemistry and mineralogy as important fields of geology. Based on these foundations, geologists have through the last century developed hypotheses that have led to the present day theories and opinions on provenance, geological evolution, age and regional relationships of the peridotite at Almklovdalen.

Early hypotheses suggesting that the Almklovdalen represent an completely unaltered igneous intrusion (Eskola, 1921) or the quite opposite that the garnet-bearing materials within the peridotites are metamorphosed gabbroic rocks (Davidson, 1943; Davidson, 1944) have been explicitly evaluated and are therefore not relevant to the problem of this thesis. Already at an early stage the ultramafic rocks at Almklovdalen and other locations in WGR were believed to be altered mantle fragments incorporated into the crust by orogenic processes (O'Hara and Stewart, 1963). Eclogites, anorthosites and peridotites all occur as lenticular masses within the WGR and evaluation of their relationship by Lappin (1966) was another important step toward deducing the provenance of these lithological elements. Lappin (1966) argued that they are all foreign to the complex, due to contact reactions and a strong correlation between foliation within the bodies and the contact towards surrounding rocks. He further suggested that presence of the mineralogically and texturally distinct garnet amphibolites and hornblende gneisses as basic components of the WGR, meant that a foreign origin for the eclogites and the ultramafic rocks was necessary. Anorthosites, also suggested to be a foreign element, have granulite mineralogical facies which is similar metamorphic grade as the WGR complex. Lappin (1966) concluded that the contact relationships between the anorthosites and the peridotite at Almklovdalen are tectonic, based on the nature of a direct contact between the two lithologies approximately 1.25 km WSW of Lien. A biotite-bearing anorthosite band approximately 5 m wide shows contact reactions similar to those against the neighboring peridotite and forms tectonic inclusions within the peridotite (Lappin, 1966). Other important observations described by Lappin (1966) are the occurrence of two distinct variants of dunite with the same mineralogical composition in the internal parts of the peridotite massif, and a reaction zone formed by penetrative serpentinization of the peridotite along the strike of the contact against the surrounding gneisses. One variant of dunite is described as light green in color and the other is described as dark gray to green; this is suggested to be a result of different degrees of hydration by fluid percolation. The reaction zone of penetrative serpentinization is described as gradually decreasing away from the contact against the surrounding gneiss.

4.2 Hypotheses on provenance and timing of emplacement

Hundreds of ultramafic bodies, from a few cubic meters to several cubic kilometers, are scattered throughout the WGR. The provenance of these lithological elements, their age, processes and time of emplacement into the Baltic continental crust have been subjects of scientific research through a century. From research conducted at the large peridotite massif at Almklovdalen two competing hypotheses were established, involving different provenance, age, process and timing of emplacement of this specific peridotite. From these hypotheses two models of emplacement are

developed. These models do not necessarily explain all peridotites in the WGR but apply to the Almklovdalen peridotite.

1. **The sinking intrusion model:** Recent work suggested that the peridotites in the WGR are fragments of Archean subcontinental mantle intruded into the Baltic crust from the mantle wedge underneath Laurentia during the Caledonian continental subduction (Beyer et al., 2004; Beyer et al., 2012; Beyer et al., 2006; Brueckner and Medaris, 1998; Brueckner et al., 2002; Brueckner et al., 2010; Cuthbert et al., 1983; Medaris Jr, 1984; Van Roermund et al., 2001; Wang et al., 2013).
2. **The up-thrusting model:** Earlier work suggested that the peridotites in the WGR represent Proterozoic mantle fragments thrust vertically into the Baltic crust from underlying Baltic lithospheric mantle (Carswell, 1968; Cordellier et al., 1981; Lappin, 1966; Mercy and O'Hara, 1965a; Mercy and O'Hara, 1965b).

4.3 Structural geology

A detailed structural geological structural survey of the Almklovdalen peridotite was conducted by Cordellier et al. (1981) and will provide a background for the structural geology part of this Thesis. This paragraph will be devoted to a description of the relevant results and the hypothesis of provenance and rheological evolution presented in this work.

Cordellier et al. (1981) suggests that layers of upper mantle garnet lherzolite were thrust vertically into crustal gneisses and later deformed by gravitational sinking to form the cone-shaped peridotite body present at Almklovdalen (Figure 4.3.1). This model is based on field mapping (Cordellier et al., 1981; Lappin, 1966) and gravimetric data (Grønlie and Rost, 1974). They refer to the age of almandine-amphibolite metamorphism in the surrounding gneisses and suggest that emplacement and gravitational sinking occurred before or during the Gothian orogeny (1.7-1.5 Ga) and the generation of the Baltic crust present in this part of the WGR. Reference to specific analyses for these ages is not given but it is likely that they refer to previously published estimates like Jacobsen and Wasserburg (1980). Later events are suggested to have had minor effects on the peridotites in the WGR. Gravitational sinking is ascribed to the density contrast between the peridotite (d=3.3 g/cm^3) and the gneisses (d=2.65-2.75 g/cm^3) in addition to the different rheological properties of the peridotites and gneisses. In their model, continuous structural deformation was accompanied by continuous retrograde metamorphism from “garnet pyroxenite facies” in the mantle to amphibolite facies in the upper crust. Based on their crystallographic observations, Cordellier et al. (1981) suggested that plastic flow dominated most of the deformation history. Hydration of the peridotite potentially lowered the activation temperature of slip systems and caused annealing in the olivine at relatively low temperature. They further concluded that hydration is restricted to the contact against the surrounding gneisses and structural elements such as foliation-, fracture- and fault-planes. The cooling rate and degree of hydration are described to decrease towards the core of the peridotite. This model is based on their crystallographic analyses, which reveal the development of mineralogical texture and hydrous parageneses (amphibolite→chlorite→antigorite) related to distance from the contact against surrounding gneisses.

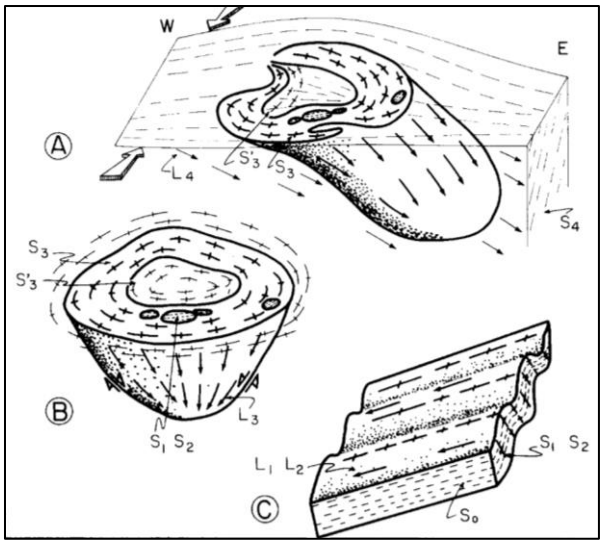

Figure 4.3.1: Illustration of the kinematic path of the peridotite massif at Almklovdalen. **A** illustrates the present day extent after phase D_4. **B** illustrates gravitational sinking and development of the cone-shaped structure during phase D_3. **C** Illustrates folding of the initial slice of upper mantle garnet peridotite during phase D_2 (Cordellier et al., 1981).

Kinematic indicators in the Almklovdalen peridotite and surrounding lithologies were used by Cordellier et al. (1981) to divide the structural evolution into four major events, D_1 to D_4. They also relate microscale kinematic indicators such as slip systems, crystallographic orientation and mineral preferred orientations to their model. S_0 to S_4 represent foliation, L_1 to L_4 represent lineation and F_1 to F_4 represent fold generations (Table 4.3.1). Petrographic facies defined in their publication are garnet lherzolite, chlorite harzburgite and dunite. Correlations between deformation parageneses, metamorphic evolution and estimated equilibration conditions in the Almklovdalen peridotite and surrounding gneisses are listed in Table 4.3.1.

Deformation event 1 (D_1)

Deformed and relatively fresh garnet lherzolite are exposed near Helghornsvatnet and at Raudehaugen. Cordellier et al. (1981) suggested that these locations represent relics from the earliest deformation event in the Almklovdalen peridotite. S_0 represents garnet-pyroxene primary banding (Figure 4.3.2), interpreted to be relics of compositional layering in the garnet lherzolite as it appeared in the upper mantle. Relics of an early folding event (F_1) in the garnet peridotite appear as open folds with axial planes oriented parallel to S_0 striking east-west and fold axes plunging gently towards the west. The S_1 foliation represents a primary foliation striking east-west and dipping approximately 80° towards the south. L_1 lineation is parallel to S_1 foliation, plunging 10°-40° westwards and represented by unaltered and slightly elongated garnets in addition to microscale crystallographic flattening of garnets and olivine crystals. S_1 foliation is plotted in stereonet B and L_1 lineation is plotted in stereonet C provided in Figure 4.3.2. Cordellier et al. (1981) interpreted the D_1 deformation to be related to thrusting of garnet peridotite slices, representing Baltic upper mantle, into Baltic lower continental crust.

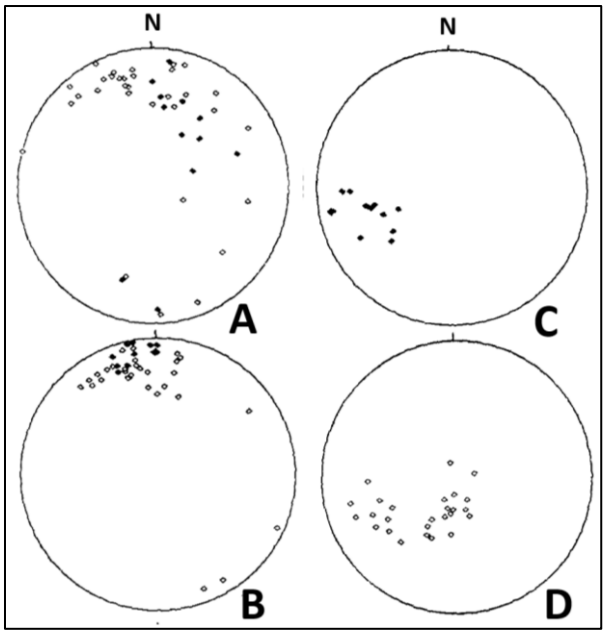

Figure 4.3.2: Stereonets showing lower hemisphere equal area projections. Poles to S_0 foliation are plotted in stereonet **A**. Poles to S_1 foliation are plotted as open symbols and poles to S_2 foliation are plotted as filled symbols in stereonet **B**. Filled symbols represent fresh garnet banding and open symbols represent chloritized garnet banding. L_1 lineation are plotted in stereonet **C** and L_2 lineation are plotted in stereonet **D**. Modified after Cordellier et al. (1981).

Deformation event 2 (D_2)

D_2 shear zones bound the garnet peridotite cores where altered garnet occurs as amphibolite-chlorite aggregates strongly elongated by shear. Flattening of olivine crystals occurred at microscales. These shear zones define a sub-vertical S_2 foliation (stereonets E and G, Figure 4.3.3) which is approximately parallel to S_1, axial planes of F_1 folds and the S_0 garnet-pyroxene primary banding. The L_2 lineation plunges 20°-80° towards the west (stereonet D in Figure 4.3.2), is subparallel to L_1 and parallel to F_1 fold axes. F_2 represents isoclinal folds suggested to have developed during D_2, with fold axes plunging 55°-90° to the west. Axial planes and fold axes of F_2 folds are parallel to S_2 foliation and L_2 lineation respectively. Cordellier et al. (1981) further describe an abrupt rotation of the primary S_0 chlorite-pyroxenite banding into parallelism with S_2 related to gradual deformation, chloritization of garnets and increasing westward plunge of the F_1 fold axes while the axial planes orientation remains unchanged. D_2 is suggested to be related to the introduction of fluids and following retrograde metamorphism which involves transition from garnet peridotite to chlorite peridotite and plastic deformation under hydrated conditions.

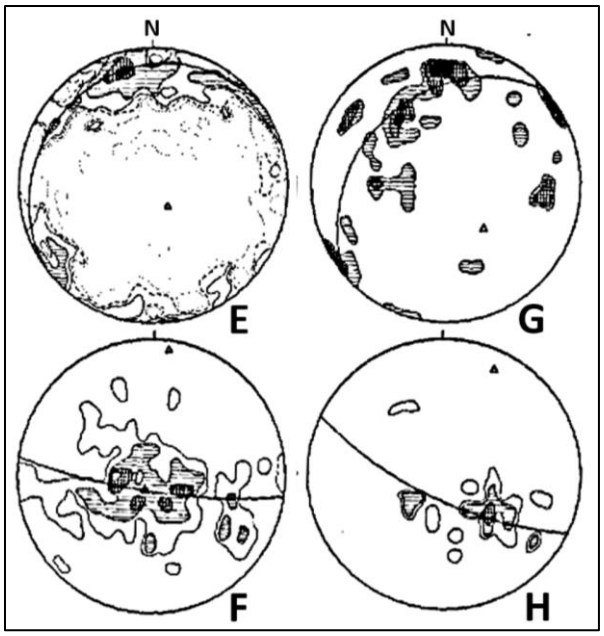

Figure 4.3.3: Stereonets showing lower hemisphere equal area projections. Poles to S_3 for the eastern fold are plotted in stereonet **E** and poles to S_3 for the western fold are plotted in stereonet **G**. L_3 for the eastern fold are plotted in stereonet **F** and L_3 for the western fold are plotted in stereonet **H**. Modified after Cordellier et al. (1981).

Deformation event 3 (D_3)

D_3 deformation involves an S_3 foliation developed by elongation of chlorite lamellae and flattening of olivine crystals. The related L_3 lineation developed by generation of spinel strings in addition to elongation of chlorite lamellae. Deformation geometry differs by a gentler dip of S_3 foliation in the western and eastern parts compared to the rest of the peridotite body. S_3 foliations are folded largely parallel to the contact towards the surrounding gneisses. D_3 deformation are suggested to have resulted in a mesoscopic folding event that developed the two large fold structures characterizing the present shape of the peridotite. Axial planes of both a F_3 western and a F_3 eastern fold are defined as a S_4 foliation. L_3 lineations are parallel to the axis of the both the western and eastern fold (stereonet F and H in Figure 4.3.3). F_3 are suggested to not have superimposed refolding on neither S_2 or S_3 foliations. Cordellier et al. (1981) also define an $S`_3$ foliation in the gneiss approximately parallel to the peridotite-gneiss contact, S_4 foliation and the axial planes of the western and eastern mesoscopic folds. D_3 is suggested to have developed during gravitational sinking of the peridotite massif into the felsic gneisses.

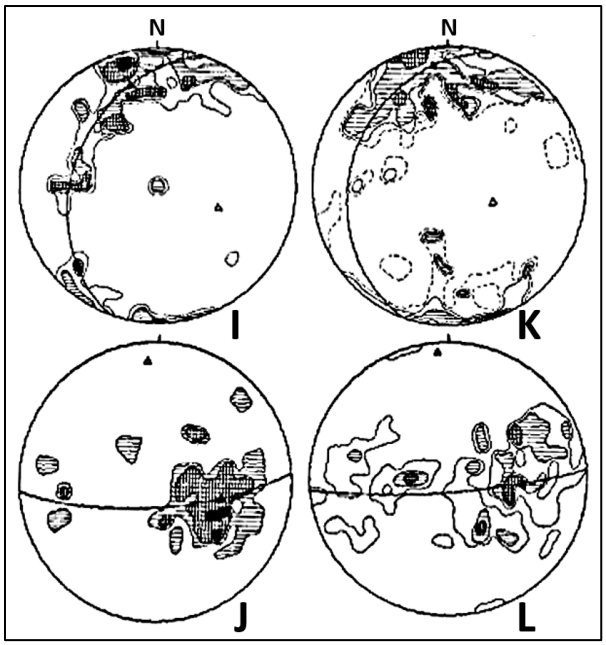

Figure 4.3.4: Stereonets showing lower hemisphere equal area projections. Poles to $S`_3$ and $S_4$ foliation in the central gneiss body are plotted in stereonet **I**. Poles to foliation $S_4$ in the surrounding gneiss are plotted in stereonet **K**. $L`_3$ and L_4 lineation in the central gneiss body are plotted in stereonet **J**. L_4 lineation in the surrounding gneiss are plotted in stereonet **L**. Modified after Cordellier et al. (1981).

Deformation event 4 (D_4)

Almandine-amphibolite to almandine-epidote facies retrograde metamorphism is recognizable in the surrounding gneisses. Cordellier et al. (1981) located relics of almandine-amphibolite metamorphism restricted to the western part of the Helgehornet gneiss massif. Epidote-amphibolite gneisses have a foliation defined as S_4 and interpreted to be metamorphic layering, based on biotite and amphibole flattening. This S_4 foliation trends east-west, dips on average 80° southwards and is parallel to the axial planes of the folds that formed $S`_3$ foliation (Stereonets I and K in Figure 4.3.4). $S`_3$ foliations in the gneiss are folded parallel both to the peridotite-gneiss contact and to the foliation defined as S_3 within the peridotite massif. $L`_3$ and $L_4$ lineation (Stereonets J and L in Figure 4.3.4) relate to the $S`_3$ and S_4 foliation respectively. They formed by elongation of amphibole+quartz+feldspar aggregates. The $L`_3$ lineation reflects stretching in the fold hinges during the related F_3 event. The L_4 lineation plunges on average 40° eastwards and was generated by flow perpendicular to the main shortening direction, which is interpreted to be north to south during the regional folding event. S_3 and $S`_3$ foliations are suggested to have been deformed by the D_4 deformation event.

A simplified illustration of S_0-S_4 foliation is provided in Figure 4.3.5 and suggested correlations between structural elements, metamorphic evolution and deformation events in the Almklovdalen peridotite and surrounding gneisses are provided in Table 4.3.1.

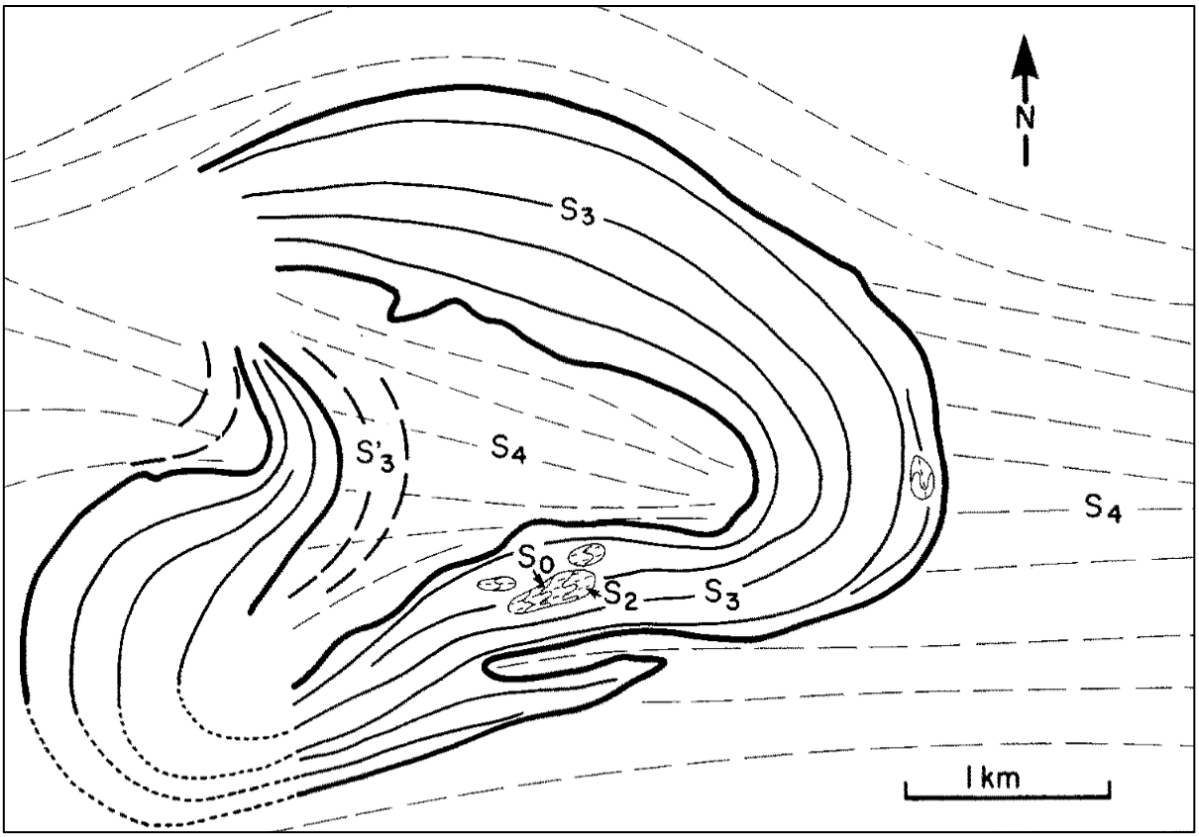

Figure 4.3.5: Illustration of the S_0-S_3 foliation within the peridotite and the $S`_3$ and S_4 foliation in the surrounding gneisses (Cordellier et al., 1981).

Table 4.3.1: Correlations between deformation history, metamorphic evolution and estimated P-T conditions in the Almklovdalen peridotite and surrounding gneisses (Cordellier et al., 1981).

Area	Paragenesis associated with deformation	Association	Location and style of the deformation	Domain of equilibrium	P/T conditions	Deformation phases
Garnet-peridotite bodies	S_0 = pyroxenitic primary banding S_1 = garnet L_1 = garnet	S_1 = S80 L_1 = W10—40	F_1, open folds in garnet peridotite	garnet peridotite	P = 12—15 Kb $T < 850°C$ (O'Hara et al., 1971) P = 17—28 Kb T = 645—820° C (Medaris, 1980)	D_1
Chlorite-amphibole-bearing garnet peridotite	S_2 = chloritized garnet L_2 = chloritized garnet	S_2 = S80 L_2 = W20—80	F_2, intrafolial folds in chlorite peridotite (shear folding)	boundary of garnet peridotite: chlorite peridotite	P = 12—15 Kb $T < 850°C$ (O'Hara et al., 1971) $P \sim$ 10 Kb $T \sim 700°C$ (Rost, 1971)	D_2
Eastern and western peridotite bodies	S_3 = chlorite lamellae in the peridotite L_3 = chlorite lamellae, spinel elongation	S_3 = rotated with L_3 fold axis L_3 = SE80 eastern fold, SE40 western fold	F_3, parallel folding in chlorite peridotite, large-scale folding of eastern and western peridotite bodies, with S_3 as axial plane	chlorite peridotite	$P < 10$ Kb $T < 700°C$ (Rost, 1971) $P \sim$ 7 Kb T = 650—700° C (O'Hara et al., 1971)	D_3
Central gneiss	S'_3 = biotite in garnet gneiss L'_3 = amphibole, quartz feldspar aggregates	S'_3 = rotated with L'_3 as fold axis L'_3 = E40	F'_3 intrafolial folds and large-scale folding in the gneiss with S_3 as axial plane	almandine-amphibolite facies	$P \sim$ 7 Kb T = 650—700° C	
Central and surrounding gneiss	S_4 = biotite in biotite gneiss L_4 = amphibole biotite	S_4 = S80 L_4 = E40	dominant flattening component	biotite-amphibolite facies		D_4

4.4 Age and timing of emplacement

Whole-rock samarium (Sm)-neodymium (Nd) isotopic analyses of garnet peridotite from Almklovdalen provided Proterozoic ages corresponding to the Gothian orogeny (1.5-1.7 Ga) (Brueckner and Medaris, 1998; Brueckner et al., 2002; Jamtveit et al., 1991; Mearns, 1986). Beyer et al. (2004) used the rhenium (Re)-osmium (Os) isotopic system to provide an alternative approach to define the age of the peridotite at Almklovdalen. High Os concentrations (0.5-10 ppm) in mantle peridotites provide an Os isotopic system resistant to metasomatic changes. Re and Os are highly siderophile elements concentrated in sulfides and the Re-Os isotopic system is sensitive to the abundance of trace sulfide phases. Enrichment of Re in sulfides by infiltration of fluids occurs during major tectonothermal events, resulting in sulfide crystallization.

Individual grains of pentlandite, heazelwoodite and chalcopyrite in garnet peridotite at Almklovdalen were analyzed by Beyer et al. (2004). Age determination by Re-Os are done either by isochron methods or by model ages of single data points assuming a chondritic mantle. The t_{RD} (time of Re depletion) age represents a minimum age of melt depletion. The t_{MA} (time of mantle extraction) model age represents the time of mantle extraction and is modeled by using Re/Os ratios to project $^{187}Os/^{188}Os$ ratios and develop an assumed growth curve for mantle Os. The t_{MA} that Beyer et al. (2004) extracted from sulfides in garnet peridotite samples collected at Almklovdalen ranges between 2.9-3.2 Ga and this is supported by t_{RD} value ages, which correspond to initial $^{187}Os/^{188}Os$ ratios. This was interpreted by Beyer et al. (2004) as strong indication of an Archean partial melting event. If the Almklovdalen peridotite were emplaced in the Baltic crust before the Caledonian subduction, Re-depletion ages related to the Caledonian- and Sveconorwegian-orogenies would not be present. Presently there is no geochronological evidence for the presence of Archean crust in the WGR. The model ages were generated assuming that sulfides formed with present Re/Os (t_{MA}); pattern of model ages suggests Re was added during Gothian orogeny (t_{RD}; 1.6 Ga) and the Caledonian orogeny (t_{RD}; 0.4 Ga). A strong peak in t_{MA} at ca 1.65 Ga and in t_{RD} at ca 1.7 Ga appear in cumulative probability plots (Figure 4.4.1) for sulfides, corresponding to the Gothian orogeny and the Sm-Nd mineral isochron ages for the garnet peridotites and garnet pyroxenite. A smaller peak occurs in t_{RD} at ca 1.1 Ga corresponding to Sveconorwegian orogeny and very few younger ages are detected in the sulfides taken as indication of minor resetting of the isotopic system.

The Sm-Nd mineral isochron age of 1703 ± 0.76 Ma (Jacobsen and Wasserburg, 1980) was interpreted to indicate recrystallization of peridotite to garnet-bearing assemblages during crystallization and forming of their present host rock. Archean Re-Os ages for dunites analyzed by whole rock techniques and mixed Archean-Proterozoic Os-isotope model ages for sulfides in garnet peridotites are suggested to indicate a Proterozoic refertilization of an Archean protolith, accompanied by sulfide introduction as reflected in model ages of interstitial sulfides (Beyer et al., 2004). Metasomatic refertilization of depleted Archean lithospheric mantle to more fertile garnet peridotite during formation of the Baltic margin crustal rocks in the Gothian orogeny is suggested to be a plausible hypothesis. Beyer et al. (2004) concluded that the results does not exclude emplacement into the Baltic crust during either the Gothian- or the Caledonian orogeny.

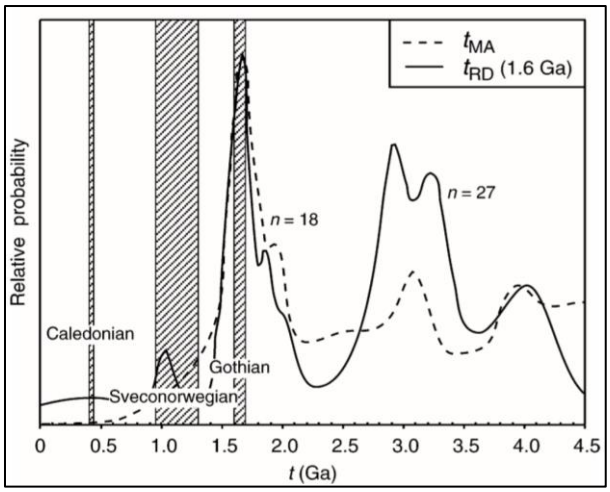

Figure 4.4.1: Relative probability plot for t_{MA} (time of mantle extraction) and t_{RD} (time of Re depletion) model ages for sulfides from garnet peridotites at Almklovdalen (Beyer et al., 2004).

Archean $^{207}Pb/^{206}Pb$ ages were documented by Beyer et al. (2012) in detrital zircons extracted from stream samples in drainage systems eroding the Almklovdalen peridotite massif. These zircons have a rounded shape, lack internal zoning and are suggested to be largely metamorphic based on this morphology. Beyer et al. (2012) plotted the $^{206}Pb/^{238}U$ *vs* $^{207}Pb/^{206}Pb$ ages in a diagram which resolves the data into three populations extend from 2.8 to 0.38 Ga, from 1.6-1.3 Ga to 0.735 Ga and from 1.1-1.3 Ga to 0.515 Ga (diagram a), Figure 4.4.2). These population correspond with the tectonothermal events during the Gothian (1.7-1.5 Ga) and Grenvillian-Sveconorwegian (1.1-0.9 Ga) orogenies. Beyer et al. (2012) further shows that Pb loss may have occurred during these three major tectonic events. The pattern of Pb loss, without mobilization of Hf, from the Archean population is presented in diagram b), Figure 4.4.2. Unusual trace-element patterns of the Archean zircon populations show similarities with zircons from carbonatites, kimberlites and low-Si granitoids, which is by Beyer et al. (2012) suggested to indicate that they derive from the depleted peridotite massif. In contrast to the younger zircon populations extracted from gneiss-dominated drainages, which show trace-element patterns similar to zircons from both high- and low-Si granitoids.

Beyer et al. (2012) state that no evidence was found that Archean crust was involved in the genesis of the WGR gneisses, neither as inherited zircons or from Hf-isotopic compositions in samples from selected drainage systems through the WGR. Juvenile magmatic additions to the crust accompanied remelting and remobilization of Gothian crustal basement during the Sveconorwegian orogeny (1.3 to <1.0 Ga). The lack of Archean zircon populations in the gneiss, combined with the Archean age of the peridotites and extensive Archean crust in East Greenland, led Beyer et al. (2012) to suggest a Laurentian provenance for the peridotite at Almklovdalen. They suggest that the peridotites were tectonically emplaced from subcontinental Laurentian lithospheric mantle overlying Baltic continental crust subducted during the Caledonian collision. Their model implies that processes involving the Almklovdalen peridotite and predating Caledonian subduction occurred in the upper lithospheric mantle of Laurentia. During the subduction the WGR is suggested to have been subjected to high-pressure to ultrahigh-pressure metamorphism, and a gradual post-Caledonian retrograde metamorphism during exhumation.

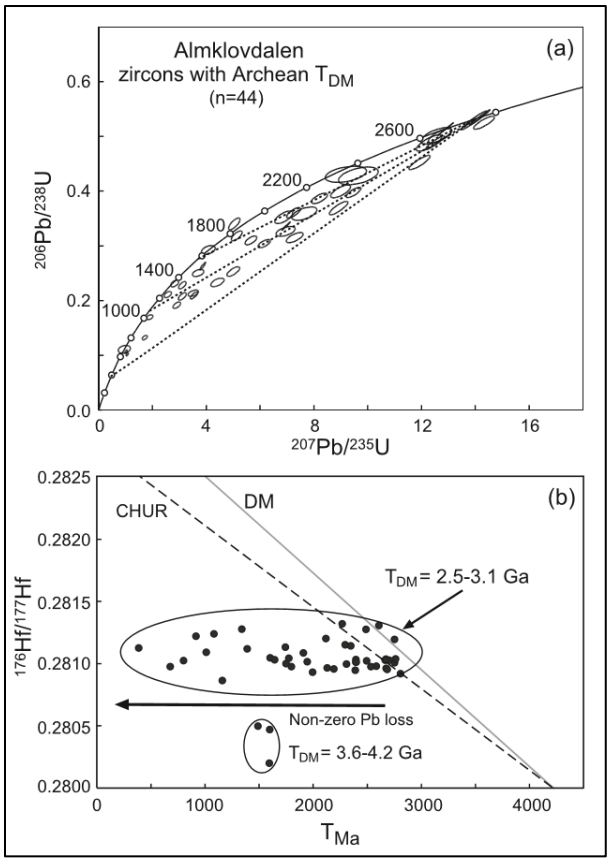

Figure 4.4.2: a) Concordia plot for zircons with Archean T_{DM} from Almklovdalen, showing discordia lines, suggesting resetting of Archean zircons during thermal events at 1,65, 1,1 and 0,4 Ga. b) Dashed lines represent $^{176}Hf/^{177}Hf_i$ *vs* age; arrow show the effect of non-zero Pb loss from the Archean population (Beyer et al., 2012).

4.5 Provenance and geochemistry

Major elements

The high Mg-numbers (Mg#; Mg/(Mg+Fe)=92-93.6) of the dunites categorize them as highly refractory; the degree of partial melting is estimated to be >60% at pressure conditions of 5-7 GPa (Beyer et al., 2006). Beyer et al (2006) further suggest that the high Cr-number (Cr#; Cr/ (Cr+Al)), combined with Mg# and low Ca and Al concentrations indicates high degrees of partial melting (Figure 4.5.1). Garnet-bearing assemblages are weakly refractory and have lower Cr# (5-20) and Mg# (90.6-91.7) in addition to higher bulk-rock Ca, Na and Al. Relatively high Na_2O contents, close to primitive mantle values, are suggested to reflect the presence of amphibole. Beyer et al. (2006) interpret the garnet peridotites to represent zones of melt percolation, imposing refertilization on the depleted dunites by clinopyroxene-rich melts. They further suggest that these melts were the parent magmas of the garnet pyroxenites and eclogites, rich in Fe, Ca, Al, Na and LREE (Light Rare Earth Elements), and poor in K and Ti. Beyer et al. (2006) conclude that the dunite in Almklovdalen is unlikely to represent retrograded garnet-bearing assemblages, as suggested by previous research (Hofmann, 1988; Medaris Jr, 1984; Osland, 1997). The Archean Re-Os model ages for dunites and mixed Re-Os model ages for the garnet peridotites from Beyer et al. (2004) are taken as indication of a Proterozoic refertilization. Plots of Mg# *vs* bulk oxides and Cr# in Figure 4.5.1, and REE and trace-element patterns in Figure 4.5.2, provide indications of a genetic relationship between the dunites and the garnet-bearing assemblages.

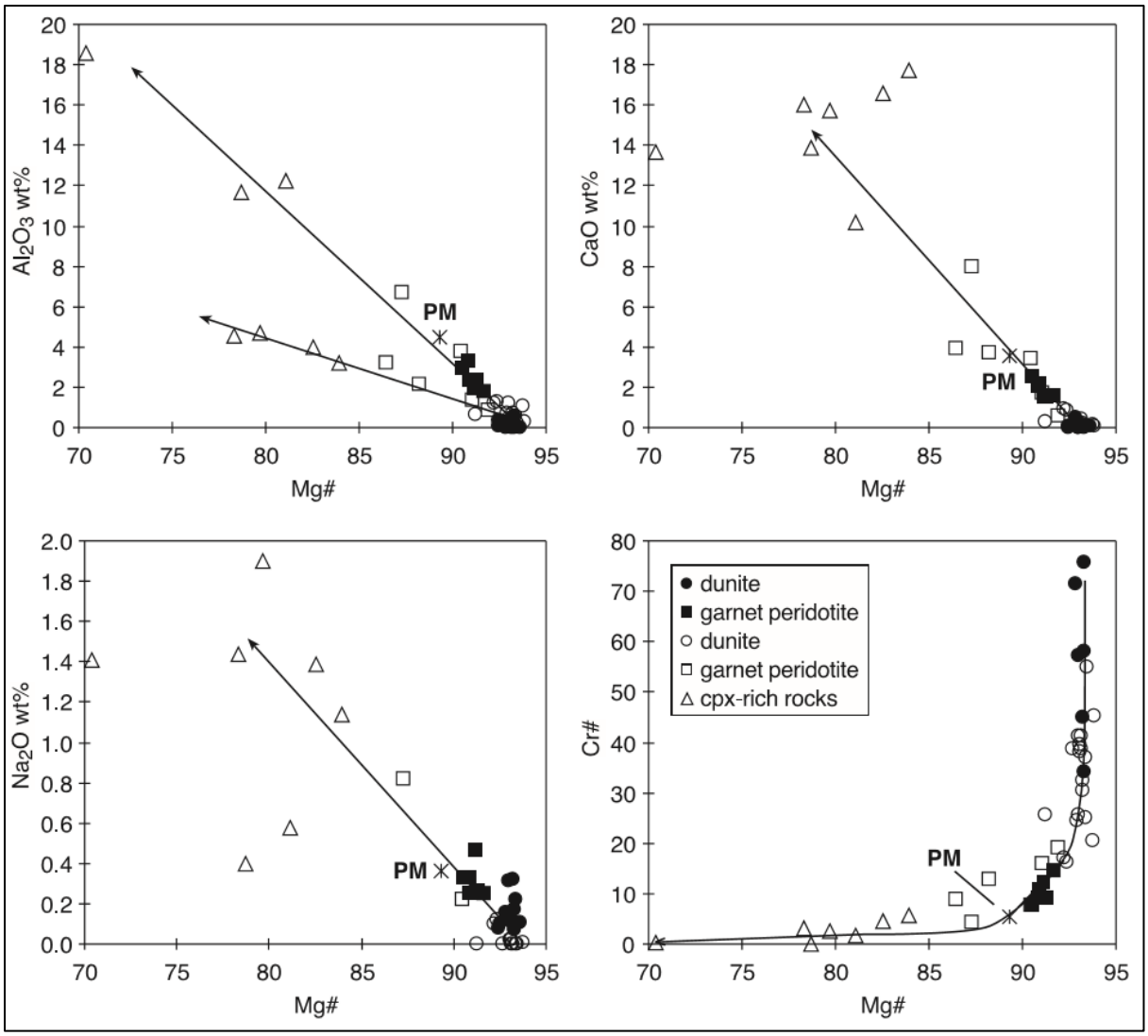

Figure 4.5.1: Mg-number plotted against selected bulk-rock major-element oxides and Cr-number from the Almklovdalen peridotite (Beyer et al., 2006). Filled symbols represent data from Beyer et al. (2006) and open symbols represent previously published data (Eskola, 1921), (Mercy and O'Hara, 1965a),(Rost (pers. comm. between Rost and Beyer in 1967), (Finstadt and Heier, 1972), (Lappin, 1974), (Cordellier et al., 1981), (Griffin and Qvale, 1985) and (Osland, 1997). Primitive mantle composition is taken from McDonough and Sun (1995)

Trace elements and Rare Earth Elements (REE)

Primitive-mantle-normalized patterns for bulk-rock Rare Earth Elements (a) and trace-element patterns (b) for garnet peridotite and dunite samples from the Almklovdalen peridotite massif are provided in Figure 4.5.2. Beyer et al. (2006) showed a positive correlation between Mg# and Ni concentration in all their samples and a weak negative correlation between Mg# and Hf in the garnet peridotites. HFSE are variable in the garnet peridotites and uniformly low in the dunites. Parallel trace-element patterns along with the spatial relationships between garnet peridotites and dikes of garnet pyroxenites are taken as indications for that garnet peridotite formed in zones of melt percolation, represented by the garnet pyroxenite veins, within the mantle. Garnet peridotite samples forms two distinct groups in terms of REE composition (Beyer et al., 2006). One group is characterized by strong enrichment of La along with depletion of MREE (Middle Rare Earth Elements) compared to LREE (light Rare Earth Elements), the other group by depletion of La along with

enrichment of MREE compared to LREE. Beyer et al. (2006) further show that the dunite samples have Ta concentrations comparable to the La-poor garnet peridotites. Enrichment of HREE (Heavy Rare Earth Elements) was detected in the garnet bearing assemblages and corresponding depletion was detected in the dunite samples. Both garnet peridotites and dunites are enriched in LREE and LILE (Large Ion Lithophile Elements). Yb is strongly depleted in the dunites and uniformly high in the garnet peridotites.

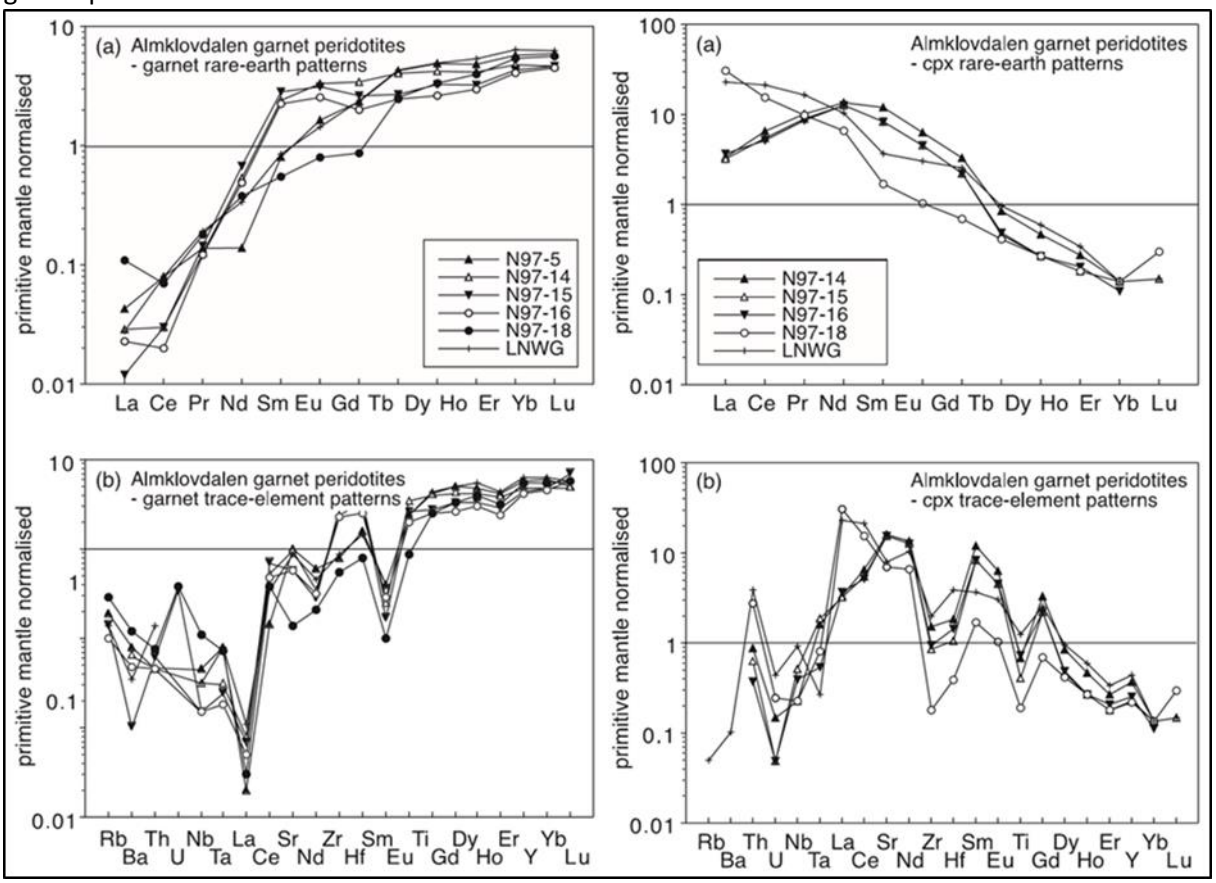

Figure 4.5.2: Primitive-mantle-normalized bulk-rock Rare Earth Element (a) and trace-element (b) patterns for garnet peridotite and dunite samples from the Almklovdalen peridotite massif (Beyer et al., 2006)

5. Methods

5.1 Experimental design

Fieldwork and field observations were the fundamental procedure used to select the outcrops, sample locations and analytical methods applied in this thesis. By observing lithological, structural, rheological, mineralogical and topographical diversity through the peridotite massif an overview of potentially interesting locations and geological features suitable for further research was obtained. Using this as a background knowledge, methodical procedures and progress were designed. The objective was to produce potentially new and additional data from the field area. Analytical methods are listed in Table 5.1.1. All results are presented in the results chapter.

Table 5.1.1: Table of analytical methods and objectives.

Method	Target
X-ray Diffraction Spectrometry (XRD)	**Whole-rock abundance of major minerals and their crystal structures**
X-ray Fluorescence Spectrometry (XRF)	**Whole-rock major-element abundance**
Inductively Coupled Plasma Mass Spectrometry (ICP-MS)	**Whole-rock and mineral trace elements including Rare Earth Elements (REE)**
Inductively Coupled Plasma Optical Emission Spectrometry (ICP-OES)	**Whole-rock major- and trace elements**
Scanning Electron Microscope (SEM)	**Whole-rock minor minerals**

5.2 Field work

Fieldwork at the Almklovdalen peridotite included collecting of samples, mapping of selected structural elements, mapping of lithological and mineralogical diversity, general mapping of the whole peridotite massif and mapping of exposed sections of the contact zone between the peridotite and the surrounding gneiss. Detailed mapping was done at selected outcrops near Helghornsvatnet. These outcrops were selected due to the abundance of structural elements and mineralogical variations not found elsewhere within the Almklovdalen peridotite. Three small areas at this location were selected to illustrate structural elements and compositional layering. Structural data were obtained using a compass and is presented by equal area projection in Schmidt nets. The mineralogical and lithological diversity present within the peridotite is described and related to tectonic and metamorphic evolution. Both pro- and retrograde metamorphic rock were mapped. Fieldwork conducted for this Thesis is based on background knowledge gained during 15 years of exploration related to semi-precious gems and rough material for rock products, previously published literature and research conducted as an employee at the SIBELCO Nordic facility in Åheim.

5.3 Samples

Eleven samples were collected at outcrops near Helghornsvatnet (no. 6 on the map in Figure 2.2.4) and six samples were collected at the Gusdal mine for comparison (no. 1-5 on the map in Figure 2.2.4). Detailed maps of sample locations are provided in Figure 6.4.1, Figure 6.4.2 and Figure 6.4.3. A list of samples including brief descriptions is provided in Table 5.3.1. More detailed descriptions are provided in the results chapter. The samples were cut using a diamond blade saw to remove altered material and provide fresh material for analyses. Appropriate amounts of each samples were crushed using a jaw crusher and ground to fine grained material using an agate mill. Splitting the ground material from each sample in four allowed for different analyses; one part for X-ray Diffraction Spectrometry (XRD), one part for X-ray Fluorescence Spectrometry (XRF), one part for Inductively

Coupled Plasma Mass Spectrometry (ICP-MS) and one part for Inductively Coupled Plasma Optical Emission Spectrometry (ICP-OES).

Table 5.3.1: List of samples.

Sample ID	Sample description	Locality	Coments
HH1 A	Relatively fresh folded garnet pyroxenite	Helghornsvatnet	Representing the HH1 locality
HH1 B	Chlorite dunite containing minor garnet and clinopyroxene	Helghornsvatnet	Representing the HH1 locality
HH1 C	Chlorite dunite containing garnet, amphibole and clinochlore	Helghornsvatnet	Representing the HH1 locality
HH1A Gnt	Seperated garnet from HH1 A	Helghornsvatnet	Representing the HH1 locality
HH1A CPx	Seperated clinopyroxene from HH1 A	Helghornsvatnet	Representing the HH1 locality
JVS 051	Fresh garnet pyroxenite	Helghornsvatnet	
JVS 156	Garnet peridotite	Helghornsvatnet	
JVS 166B	Clinochlore. Highly altered layer	Helghornsvatnet	Representing the HH3 locality
JVS 195-8 1	Altered gnt and CPx in chlorite dunite	Helghornsvatnet	Representing the HH3 locality
JVS 195-8 2	Altered gnt and CPx in chlorite dunite	Helghornsvatnet	Representing the HH3 locality
JVS 195-8 3	Altered layer in chlorite dunite	Helghornsvatnet	Representing the HH3 locality
JVS 195-8 4	Altered layer in chlorite dunite	Helghornsvatnet	Representing the HH3 locality
JVS 195-8 5	Chlorite dunite	Helghornsvatnet	Representing the HH3 locality
JVS 128	Clorite dunite	Gusdal mine	High Mg
JVS 129	Clorite dunite	Gusdal mine	High Mg
JVS 218A	Separated subhedral chromite crystals	Gusdal mine	Not previously described
JVS 218B	Bulk chromite in clinochlore. Lentz in dunite	Gusdal mine	Not previously described
JVS 301	Garnet peridotite	Gusdal mine	Near the contact against the gneiss
JVS 303	Clinochlore. Highly altered layer	Gusdal mine	Near the contact against the gneiss

5.4 X-ray Diffraction Spectrometry (XRD)

X-ray Diffraction Spectrometry (XRD) was conducted to determine the whole-rock abundance of minerals and their crystal structures in each individual sample. Powder from each sample was stained in acetone and slightly compressed in a bracket. The acetone content was evaporated from the samples and the brackets placed into a Bruker AXS D8 ADVANCED Eco diffractometer at the Faculty of Mathematics and Earth Science by the University of Bergen. Analyses were conducted while the sample brackets were rotating. Scanning of bulk powder at angles from ~5 to ~70° (2θ) by using voltage of 40 kV and current of 25 mA provided a series diffraction peaks which were converted into d values. These results were enhanced by subtracting background noise, stripping the $K_{\alpha}2$ component from the scan and adjusting the ration of the alpha signal to 0,5 (intermediate). During the first attempt one mineral phase did not match any reference data in the standard reference database Crystallography Open Database 2013 (COD 2013) installed in the Bruker EVA software. Most of the samples also contained other minerals that did not match the standards well enough to give a conclusive result. Samples containing the mineral phase not matching any standard were reanalyzed by a second scanning after slight compression of the powder in the bracket without staining it in acetone. The results still did not match any reference data in COD 2013. The specific mineral phase was interpreted to be either chlorite or clinochlore by visual observation and assumptions based on the mineralogical context it was found. Concluding that the reference database COD 2013 did not contain a standard for this mineral phase, the more comprehensive reference database PDF/Release 2009 RDB was acquired and installed. Comparing the results to reference data in the new database not only allowed determination of the phase missing in COD 2013 but improved the results for most phases in all the samples. Additional analyses of JVS 218A and JVS 218B were carried out by the laboratory at the SIBELCO Nordic main office in Norway sited in Asker. This was done along with an XRF analyses and the results are provided in Table 6.5.2.

5.5 Inductively Coupled Plasma Mass Spectrometry (ICP-MS)

Abundance of trace elements, including REE, in whole-rock and mineral samples were determined by Inductively Coupled Plasma Mass Spectrometry (ICP-MS). The trace elements analyzed were the large ion lithophile elements (LILE; Rb, Sr, Cs, Ba, Th and U), high field strength elements (HFSE; Sc, Y, Zr, Nb, Pb and Hf), REE, and minor and transition elements (Ti, V, Cr, Mn, Co, Cu and Zn).

1 g of fine grained powder from each sample and three separated mineral phases were ignited in a furnace at 1000°C for 60 minutes. This process removed volatile content from the samples and loss of ignition (L.O.I.) was calculated. Then ca 0.1 g of ignited material from each sample was weighed into 25 ml PFA Savillex beakers and the exact weight of each sample were documented. The sample powder was then digested by adding 3 ml concentrated HF. These mixtures were then heated at 135 °C for approximately 48 hours and the supernatant liquid HF evaporated. The fluoride residues were thereby hydrolyzed by adding a weak solution of HNO_3. This solution was also heated in order to evaporate the liquid. This was done under sub-boiling point conditions to avoid losing sample material which might be a result if the solution starts to boil. During this procedure unsolvable fluorides transformed to solvable nitrates. The nitrate salt residues were dissolved by adding ca 2 ml 2% HNO_3 and then diluted with 2% HNO_3 in 50 ml water. The samples derive from ultramafic rocks containing chromite which did not dissolve completely. Most of the residue was dissolved by adding 1 ml of Aqua Regia (three parts concentrated HCl + one part HNO_3) and then heating the solution. The samples JVS 218 A and JVS 218 B has relatively high chromite contents and was not dissolved completely. Minor amounts of chromite particles may also be present in other samples.

Analyses were conducted using the Thermo Scientific ELEMENT XR™ Inductively Coupled Plasma Mass Spectrometer at the Faculty of Mathematics and Earth Science at the University of Bergen. 1 ppm of Indium was added to each sample as an internal standard. In addition, standard reference materials BCR2 were analyzed parallel with and between the samples. Whole-rock and mineral trace elements including REE were determined for all samples. Average relative standard deviation (RSD) ranges between 0.42-9.43%, representing the precision of the results and average recovery ranges from 82.69-113.76%, representing accuracy (Table 5.5.1). The analytical results are presented in Table 6.6.1.

Table 5.5.1: Average relative standard deviation (RSD) and recovery in percentages for each individual element analyzed by ICP-MS.

Element	RSD%	Recovery%	Element	RSD%	Recovery%
Sc	1,11	101,58	Th	3,02	98,51
Ti	0,87	101,90	U	2,46	101,91
V	0,52	99,10	Y	2,93	97,93
Cr	2,10	82,69	La	4,14	101,65
Mn	1,59	95,29	Ce	3,03	97,42
Co	0,91	101,29	Pr	2,13	101,00
Cu	4,36	83,07	Nd	2,58	104,83
Zn	9,43	110,48	Sm	2,80	99,79
Rb	0,71	97,92	Eu	3,99	103,10
Sr	0,60	99,14	Gd	3,91	100,03
Y	1,32	92,28	Tb	4,02	100,70
Zr	1,57	102,38	Dy	4,15	103,62
Nb	1,58	99,12	Ho	4,39	100,05
Cs	0,42	101,95	Er	4,55	106,73
Ba	1,11	100,39	Tm	5,75	99,46
Hf	2,01	113,76	Yb	5,17	99,65
Pb	2,69	90,93	Lu	6,07	102,95

5.6 Inductively Coupled Plasma Optical Emission Spectrometry (ICP-OES)

Abundances of major elements and trace elements in whole-rock samples were determined using Inductively Coupled Plasma Optical Emission Spectrometry (ICP-OES). Major elements include Na, Mg, Al, Si, P, K, Ca, Ti, Cr, Fe and Ni. Trace elements analyzed include the large ion lithophile elements (LILE; Sr), high field strength elements (HFSE; Y, Zr and Pb), in addition to minor and transition elements (V, Cr, Ni, Co, Cu and Zn). Cr and Ni are presented as both trace elements (ppm) and major elements (wt% oxides) due to the relatively high content of these elements in the samples.

A powder fraction from each sample and three of international standard reference materials (SRM) were weighed, heated in a furnace and weighed again to determine loss of ignition (L.O.I.). The SRM used were SPS-SW2, BCR2 and UB-N (serpentine). Then each sample was melted with lithium tetra-borate as flux and cooled to glass tablets which were weighed again and crushed manually using an agate mortar. 0.1 g of each sample was dissolved in HNO_3 and diluted to 50 ml of solution of which 10 ml were used in the analyses. 1 ppm of Scandium was added to each sample as internal standard and a blank sample of lithium tetra-borate was analyzed along with the samples to control blank levels. All samples and reference materials were analyzed using a Thermos Scientific iCAP 7000 ASX 520 series Inductively Coupled Plasma Optical Emission Spectrometer at the Faculty of Mathematics and Earth Science of the University of Bergen. The analytical process was conducted in five steps. Internal standards were analyzed first, then samples excluding JVS 216A and JVS 216B along with two international standards were analyzed. Next the internal standards were analyzed again followed by an attempt to analyze samples JVS 216A and JVS 216B. Finally, the internal standards were analyzed a third time. All samples and all elements were analyzed in three parallel runs. Relative standard deviation (RSD) ranges between 0.01-22.18%, representing the precision of the results and average recovery ranges from 94.7-117.7%, representing accuracy for sample SPS-SW2. Certificates for the standard reference materials BCR2 and UB-N provided variable standard values so the average

results are given along with these values instead of recovery. Relative standard deviation (RSD), average value from results and given standard value/s for each individual element are listed in Table 5.6.1.

Table 5.6.1: Average relative standard deviation (RSD), average values from the results and given standard value/s for each individual element. (NG: Not given and ND: Not detected).

	SPS-SW2			BCR2			UB-N		
	RSD	Recovery	Standard value	RSD	Average result	Standard value	RSD	Average result	Standard value
Element	%	%	ppm	%	ppm	ppm	%	ppm	ppm
Na	2,11	94,75	10,00	1,06	21227	22600-24200	2,85	1643	950-1084
Mg	0,70	98,09	2,00	0,69	20748	21300-21900	0,39	241413	199000
Al	20,75	112,58	0,25	0,84	68291	70400-72400	1,46	16654	15600
Si	6,84	98,09	5,00	0,50	239813	249000-257000	0,38	203219	197000
P	11,36	117,70	0,50	13,28	1775	1400-1600	46,48	52,51	NG
K	1,50	99,18	1,00	2,87	14315	14500-15300	0,16	231	<200-<5000
Ca	0,47	99,80	10,00	0,74	48487	50100-51700	0,44	9165	8080-9000
Ti	ND	ND	NG	0,75	13317	13200-13800	1,56	642	560
Mn	0,03	101,45	0,05	0,57	1504	1460-1580	0,05	1047	906-973
Fe	0,08	100,36	0,10	0,30	92862	95100-98100	0,11	62906	52700-57100
Co	0,03	99,39	0,01	1,25	62,34	34-40	0,15	110	100-102
Cu	1,02	98,74	0,01	10,63	10,71	17-21	4,44	30,80	27-28
Cr	22,18	99,43	0,01	2,88	16,78	16-20	1,28	2678	2300-2421
Ni	0,33	103,35	0,05	0,76	98,93	NG	0,53	2195	1942-2000
Pb	2,62	112,88	0,03	2,32	142	9-13	1,20	129	12,8-13
Sr	0,75	100,30	0,25	0,49	320	332-360	0,25	18,12	7,7-9
V	0,37	100,06	0,05	1,09	440	402-430	2,22	73,47	63-75
Y	2,27	97,79	0,00	0,37	29,31	35-39	1,71	1,83	2,5
Zn	0,94	103,03	0,10	2,44	141	118-136	1,37	96,34	84-85
Zr	4,70	ND	0,00	0,50	183	172-204	3,90	7,94	3,8-4

6. Results

6.1 Lithological units

Terminology used in this Thesis are defined and described in this paragraph. The ultramafic rocks are categorized according to the ternary diagram presented in Figure 6.1.1. In the olivine- and pyroxene-bearing rocks these minerals are also classified according to ternary diagrams of their most common endmembers. Some of the terms used to define the individual zones in the peridotite on the geological map illustrating zonation in the Gusdal open pit mine (Figure 6.2.2) are modified from Osland (1997). The gneisses surrounding the peridotite massif at Almklovdalen are defined from http://geo.ngu.no/kart/berggrunn/. Categorizations are additionally based on XRD results and major element abundance. Rock type definitions are presented below.

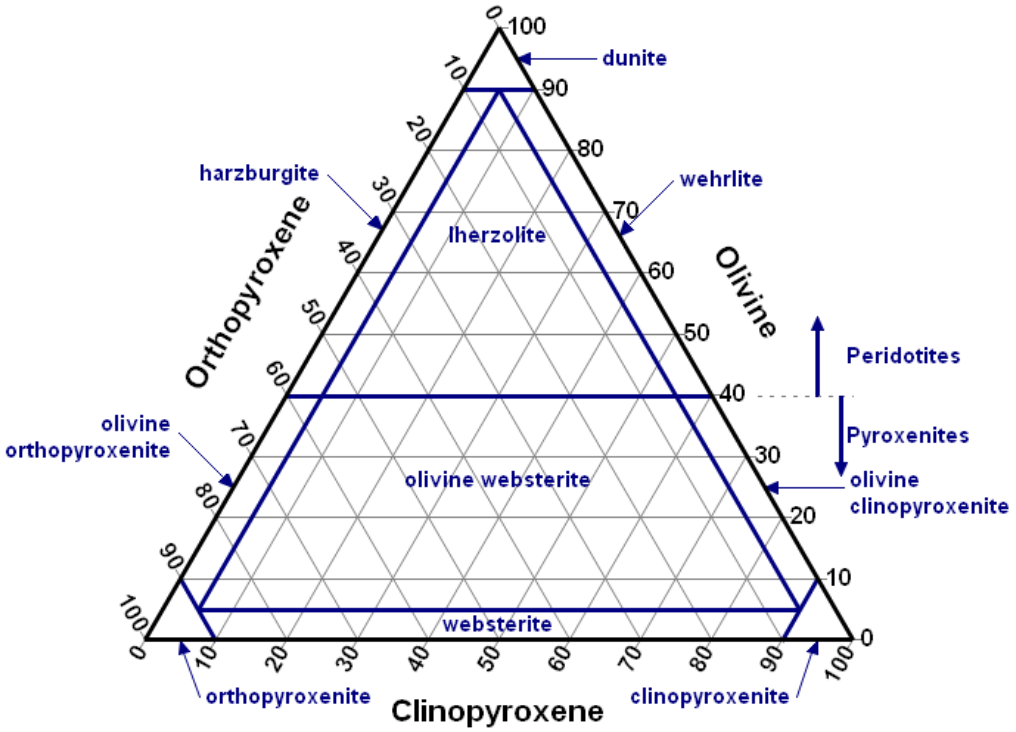

Figure 6.1.1: Ternary diagram for categorization of ultramafic rocks (http://www.dplot.com/mt/mt-search.cgi?blog_id=1&tag=triangle%20plot&limit=20, accessed: 15.12.2015).

Peridotite

Peridotite is for practical reasons used as a general term for the whole ultramafic massif at Almklovdalen. In its strict meaning peridotite includes dunite, harzburgite, lherzolite and wehrlite (Figure 6.1.1) and these are the volumetrically dominant rock types. Terminology used for their retrograded equivalents and pyroxenites are further described below.

Gneiss

Dioritic to granitic gneiss and migmatite, biotite-rich granitic gneiss, mica gneiss, quartz-mica gneiss, locally migmatitic, thin lenses of garnet amphibolite, garnet mica schist and anorthosite (http://geo.ngu.no/kart/berggrunn/). The major minerals in the gneiss determined by field observation are quartz, plagioclase, K-feldspar, biotite, muscovite and amphibole. Minor minerals determined by field observation are almandine garnet, pyrite, fluorite, calcite, hematite and titanite.

Dunite

Homogenous and relatively pure dunite (>90% forsterite with Mg#~93) with a low bulk clinochlore content. The volumetrically dominant dunite in the Almklovdalen peridotite may have minor content of chromite (spinel), orthopyroxene (enstatite), mica (phlogopite and vermiculite) and amphibole. Sulfides are practically absent but Ni sulfides like hazelwoodite and libenbergite are described in small quantities (Gautneb and Flem, 2001). The sulfur content in the olivine products is measured once a year by SIBELCO Nordic and varies from 0-300 ppm. Very low degree of penetrative serpentinization but rims of serpentine are widespread on fractures and fault planes. On the geological map illustrating zonation (Figure 6.2.3) this term is used to specifically to define zones that contain no or very few chlorite bands and veins. In all other associations this term is used for the volumetric dominate dunite.

Chlorite dunite

If the dunite contains more than ~5% visible chlorite it is termed chlorite dunite. This term is used for the dunite surrounding the chlorite dunite with clinochlore layers, found at the field area near Helghornsvatnet. The dunite in this area contain scattered pods of clinochlore <1.5 cm long and <0.5 cm wide orientated parallel to the foliation.

Chlorite banded dunite

Homogenous and relatively pure dunite (>90% olivine) with a low bulk clinochlore content, orthopyroxene and amphibole content. Contains bands of chlorite up to 0.5 cm thick, formed in fractures and faults dominantly parallel to main foliation (Figure 6.1.2). Exceptions are found in fractures and faults not parallel to the main foliation. Chlorite banded dunite defines the zones where chlorite bands are dominant compared to chlorite veins. (Modified after Osland (1997)).

Figure 6.1.2: Photo of chlorite banded dunite.

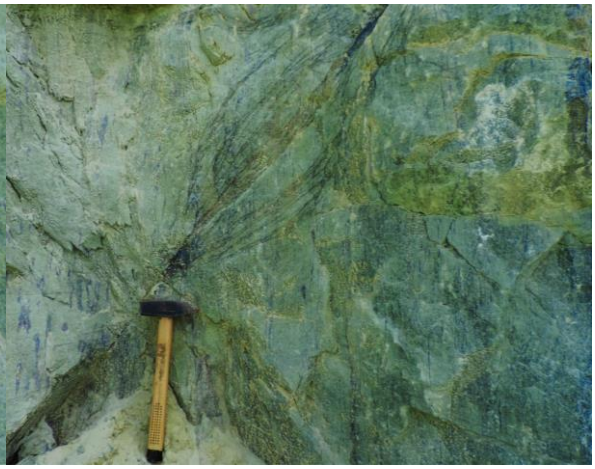

Figure 6.1.3: Photo of chlorite veined dunite.

Chlorite veined dunite

Homogenous and relatively pure dunite (>90% olivine) with a low bulk clinochlore, orthopyroxene and amphibole content. Contains chlorite veins up to 0.5 cm wide penetrating the dunite and crosscutting the main foliation. These veins have characteristics of hydro-fracturing networks (Figure 6.1.3). Chlorite veined dunite defines the zones where chlorite veins are dominant compared to chlorite bands. (Modified after Osland (1997)).

Serpentine dunite

Recognized in the field by its dark green to light brown color and slightly higher competence/hardness than the dunite. Low degree of penetrative serpentinization of a homogenous and relatively pure dunite (>90% olivine) with a low bulk clinochlore content. Minor orthopyroxene and amphibole content. Serpentine dunite has higher L.O.I. and lower MgO content than the dunite and the Fe content is present as magnetite. (Modified after Osland (1997)).

Serpentinite

Recognized in the field by its dark brown to blackish color, high competence/hardness and magnetic properties. High degree of penetrative serpentinization of homogenous and relatively pure dunite (>90% olivine) with a low bulk clinochlore content. Minor orthopyroxene and/or amphibole content. Serpentinite has higher L.O.I. and lower MgO content than serpentine dunite and the Fe content is present as magnetite. (Modified after Osland (1997)).

Forsterite granoblasts (G)

Forsterite granoblasts from 0.5-40 cm in diameter consisting of light green to green sub-transparent to transparent crystalline forsterite (Modified after Osland (1997)). Sub-transparency is caused by microscale chromite inclusions. Occurs dominantly in one defined zone that crosscuts the main foliation and strikes northwest-southeast. Forsterite granoblasts have the highest Mg content (MgO=50-51 wt%; Mg#>93) found in the peridotite massif.

Eclogite (E)

Pyrope garnet and clinopyroxene- to amphibole-dominated matrix. Eclogites are distinguished from garnet pyroxenes by their omphacite-dominated matrix in contrast to diopside-dominated matrix. They have minor contents of biotite, orthopyroxene, pyrite and apatite. In many eclogite lenses the pyroxenes are partly retrograded to amphibole and contain cores where the clinopyroxene matrix are still preserved. Pyrope garnets have developed alteration rims which are thickest in the amphibolite matrix and slightly thinner or absent in the pyroxene matrix. Eclogites found along the strike of the northern contacts at the Gusdal mine consist almost entirely of pyrope garnet. Eclogites have sharp contacts towards dunite and serpentinized assemblages and occur as lenses and veins with strike parallel to the main foliation and to the peridotite contact against the gneiss.

Garnet pyroxenite (GPx)

Pyrope garnet and orthopyroxene in clinopyroxene-dominated (<40% olivine) matrix. Garnet pyroxenites occur as lenses and layers. Lenses are oriented with their strike parallel to the main foliation and the contacts against the gneiss. Layers occur in open folds (F_1 of Cordellier et al. (1981)) and in isoclinal to tight folds (F_2 of Cordellier et al. (1981)) in chlorite dunite. Lenses of garnet pyroxenite are found along the northern contact in the Gusdal mine. Layers of garnet pyroxenite are found in one location at Raudehaugen and are widespread in the outcrops near Helghornsvatnet selected for detailed mapping in this Thesis. Garnet pyroxenites have either sharp contacts towards dunite or a gradual transition to garnet peridotite and further to dunite or chlorite dunite. Garnet-bearing clinopyroxenite, orthopyroxenite, olivine websterite and websterite are generally grouped here as garnet pyroxenite.

Garnet peridotite (GP)

Pyrope garnet, orthopyroxene (enstatite) and clinopyroxene (diopside) in olivine (>40%) matrix. Enstatite and diopside occur as subhedral to anhedral crystals <3 cm in diameter in the dunite matrix. Garnet peridotite is found in close proximity to garnet pyroxenite lenses and layers. One exception is the field area near Helghornsvatnet where a larger area of garnet lherzolite/wehrlite is exposed (Figure 6.3.3). These garnet-bearing assemblages are generally described as garnet peridotite.

6.2 Results and field observations from general mapping

Field mapping of the peridotite at Almklovdalen resulted in a more detailed geological map (Figure 6.2.2) of the entire massif than previously surveys have produced. Documentation of a continuous peridotite massif all around the central Helgehornet mountain was obtained in contrast to the map made by NGU (Norwegian geological survey) provided in Figure 2.2.3. Other workers have concluded that the peridotite is continuous around the Helgehornet mountain but this was mainly done by interpretation (Beyer et al., 2006; Cordellier et al., 1981; Kostenko et al., 2002; Osland, 1997) and not by detailed field mapping. The contact towards the surrounding gneiss varies widely within these publications.

The contact zone in the surrounding lithologies

The rocks surrounding the peridotite are dioritic to granitic gneiss and migmatite. Biotite-rich granitic gneiss, mica gneiss, quartz-mica gneiss, locally migmatitic, thin lenses of garnet amphibolite and garnet mica schist have been described (http://geo.ngu.no/kart/berggrunn/). Contact relationships between the peridotite and surrounding gneiss were observed directly in a narrow zone along the northern contact. This is one of few well exposed outcrops in the gneiss within 4 m distance of the peridotite. Isoclinal folds at cm scale resulting from ductile shear movement were observed in compositionally banded gneiss. A narrow reaction zone < 0.5 m wide is present between the serpentinized peridotite and the gneiss. Metasomatic crystallization of euhedral to subhedral quartz, calcite and muscovite occurs in fractures up to 5 km from the contact with the peridotite. The quartz occurs as light purple amethyst in some locations. Large anorthosite and eclogite lenses and bodies are located throughout the region. In addition, smaller eclogites are widespread in the gneiss near the contact to the peridotite (Figure 6.3.2).

Ultramafic rocks in small lenses of a few m^3 to large bodies are scattered in the gneiss all around the large peridotite massif. Fibrous minerals, magnesite, talc and serpentinization are widespread in these minor ultramafic lenses. Mining for chrysotile was for a short period established in two of them and at one location within the large peridotite. One of lenses, located north of Åhaugen (No. 1, Figure 6.2.3), has in all previous field mapping been interpreted as part of the large peridotite. During this field mapping, continuous gneiss exposures were observed in the Gusdal riverbed identifying it as a separate lens. The other one is located north of Berge (No. 2, Figure 6.2.3) and these individual lenses are extensively hydrated compared to large peridotite massif. Pillow-like pods approximately 30-50 cm in diameter separated by talc were observed in an approximately 5 m wide and 5 m high outcrop of ultramafic rock on the path from Sunndalen to the west end of Helghornsvatnet (No. 3, Figure 6.2.3). South of Skaret farm another small outcrop of ultramafic roc is located (No. 4, Figure 6.2.3). Actinolite pods approximately 30 cm in length, 20 cm in width and 20 cm high were observed at two localities approximately 2 m from the contact into the gneiss (Figure No. 6 and No. 7, Figure 6.2.3). Various ultramafic rock-types like dunites, harzburgites and pyroxenites are scattered throughout the region and these are marked as peridotites at the geological map provided in Figure 2.2.2. An important implication for the presently accepted emplacement models is that anorthosites are also distributed throughout the region. They show strong similarity in occurrence and located in

close spatial relationship to the peridotites. A relation between these lithological elements are difficult to dismiss but according to the presently accepted geological evolution model for the WGR such relation is not apparent.

Crosscutting relationships between the peridotite and an approximately 5 m wide zone of anorthosite in the gneiss can be observed approximately 1,25 km WSW of the farm Lien (No. 7, Figure 6.2.3). Xenoliths of anorthosite were found in the peridotite and an approximately 2-3 m thick layer of amphibolite was observed along the anorthosite. This locality was described by Lappin (1966) but was reexamined during this field work due to the importance of its geological implication it provides (Figure 6.2.1). The anorthosite is coarsely crystalline and shows a tendency to karst-like weathering. Mixtures of peridotite and anorthosite, amphibolite or gneiss were not found and are not likely due to the distinct mineralogical properties of the ultramafic mineral assemblages in the peridotite and the felsic to mafic mineral assemblages in these rocks. Approximately 20 m to the SW of this location a layer of amphibolite was found (No. 8, Figure 6.2.3) in the gneiss and approximately 80 m to the SW a body of eclogite was found (No. 9, Figure 6.2.3). The area between these lithologies is covered by vegetation so their relations are difficult to deduce further. In terms of emplacement history and field relation between the peridotite and the surrounding lithologies these elements are important for further research.

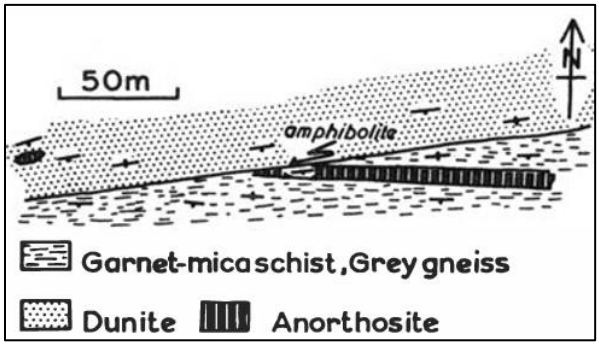

Figure 6.2.1: Field sketch illustrating the anorthosite-peridotite direct contact (Lappin, 1966).

The contact

The actual transition from peridotite to gneiss is abrupt and covered around the entire peridotite massif except a few locations were sections of contact ranging from 0.5-4 m in length are exposed. These locations are located along the northern contact zone west of Berge (No. 5, Figure 6.2.3), in the Gusdal riverbed (No. 10, Figure 6.2.3) and in the riverbed at Raudekleivane (No. 11, Figure 6.2.3). The reaction zone between the peridotite and the gneiss is highly permeable and less competent than both the serpentinized dunite and the gneiss. Therefore, it has lower resistance to weathering and due to erosion the contact occurs as a sediment-filled depression all around the peridotite massif. An abrupt change in the orientation of the contact were mapped at Raudekleivane (No. 11, Figure 6.2.3). This feature might have important structural implications for several eclogite boudins within the peridotite. Another interesting structural feature regarding the orientation of the contact is located by Eidevatnet (No.12, Figure 6.2.3). These structures will be discussed further in the discussion chapter.

The contact zone within the peridotite

The Gusdal open pit mine covers an area in the northern section of the peridotite massif and mining has resulted in exposure of a surface area of the peridotite near the northern contact towards surrounding gneiss (Figure 6.2.2 and Figure 6.2.3). Serpentinization of the dunite decreases gradually with increasing distance from the contact towards the core of the peridotite and is limited to >70 m from the contact. This zone is indicated as two lithological units on the zonation map (Figure 6.2.2)

and described as serpentinite and serpentinized dunite above. Numerous veins and lenses of garnet peridotite, garnet pyroxene, amphibole-rich clinochlore and eclogue have been found near the contact during mining activities. Garnet bearing assemblages occur in close proximity to- and along the strike of the contact against the gneiss. Such lithological elements are not known to have been found more than 60 to 70 meters from the contact in this area of the peridotite. Lenses containing eclogite cores enclosed in amphibole, lenses of amphibole-rich clinochlore, garnet peridotite and garnet pyroxenite occur in serpentinized dunite. Eclogite cores enclosed in amphibole contain minor apatite and pyrite. The garnet pyroxenites are surrounded by garnet peridotite with a gradual transition to serpentinized dunite. These rocks are all found in similar lenses previously interpreted as boudins and are all located within approximately 40 m from the contact against the gneiss. Like the degree of serpentinization of the dunite, the alteration of pyroxenes and garnet in eclogite to amphibole and the chloritization of pyroxenes and garnet in the peridotite decrease with increasing distance from the contact. Drill cores penetrating the contact at this northern perimeter of the peridotite were examined at the SIBELCO Nordic plant at Åheim. These indicate that all described garnet bearing assemblages and their retrograded equivalents are widespread on a vertical scale all along the contact. A 4 km long underground tunnel constructed for transport of the olivine product by conveyor belt, from the crushing facility at the Gusdal mine to the sorting facility at the Åheim plant, crosscuts the contact zone. This location provided evidence that large volumes of groundwater drain along the contact zone, which has high permeability and connectivity.

Zonation

Zonation in peridotite was mapped in the Gusdal mine area during a survey conducted from 15. June to 15. August 2014 in order to create a background for evaluation of properties such as Mg concentration, hardness and loss on ignition (L.O.I.), which are important for the quality of the products delivered by SIBELCO Nordic. Variations in the peridotite were defined from mineralogical content and degree of alteration. A practical terminology for this purpose was modified from Osland (1997) in an internal report made for SIBELCO Nordic (Seljebotn and Soldal, 2014) and modified again for this Thesis (Section 6.1). A modified geological map from Seljebotn and Soldal (2014) illustrating zonation in the peridotite at the Gusdal open-pit mine is presented in Figure 6.2.2. Zoning varies on a vertical scale and the geological map in Figure 6.2.2 represents the surface at the time of mapping (15.06.14-15.08.14). The geological map in Figure 6.2.3 provides an overview of the zonation in the Gusdal mine on a larger scale. Continuous upgrading of the map is sufficient to give an indication of vertical variation. “Chlorite” was in this case used for both chlorite and clinochlore minerals for practical reasons. Chlorite-banded and chlorite-veined dunite often occur together and the dominant texture defines the selected terminology.

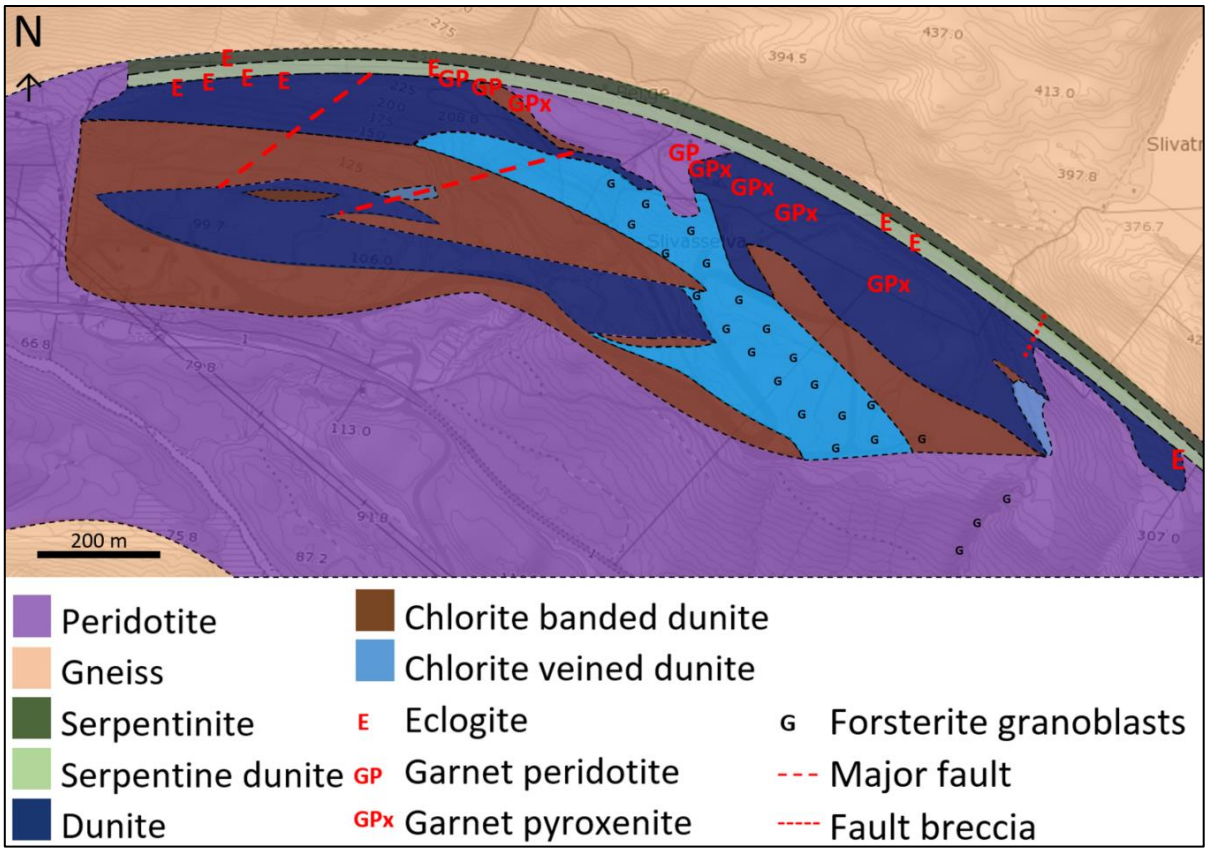

Figure 6.2.2: Geological map illustrating zonation of the Gusdal mine area at Almklovdalen between 15. June to 15. August 2014 (Seljebotn and Soldal, 2014).

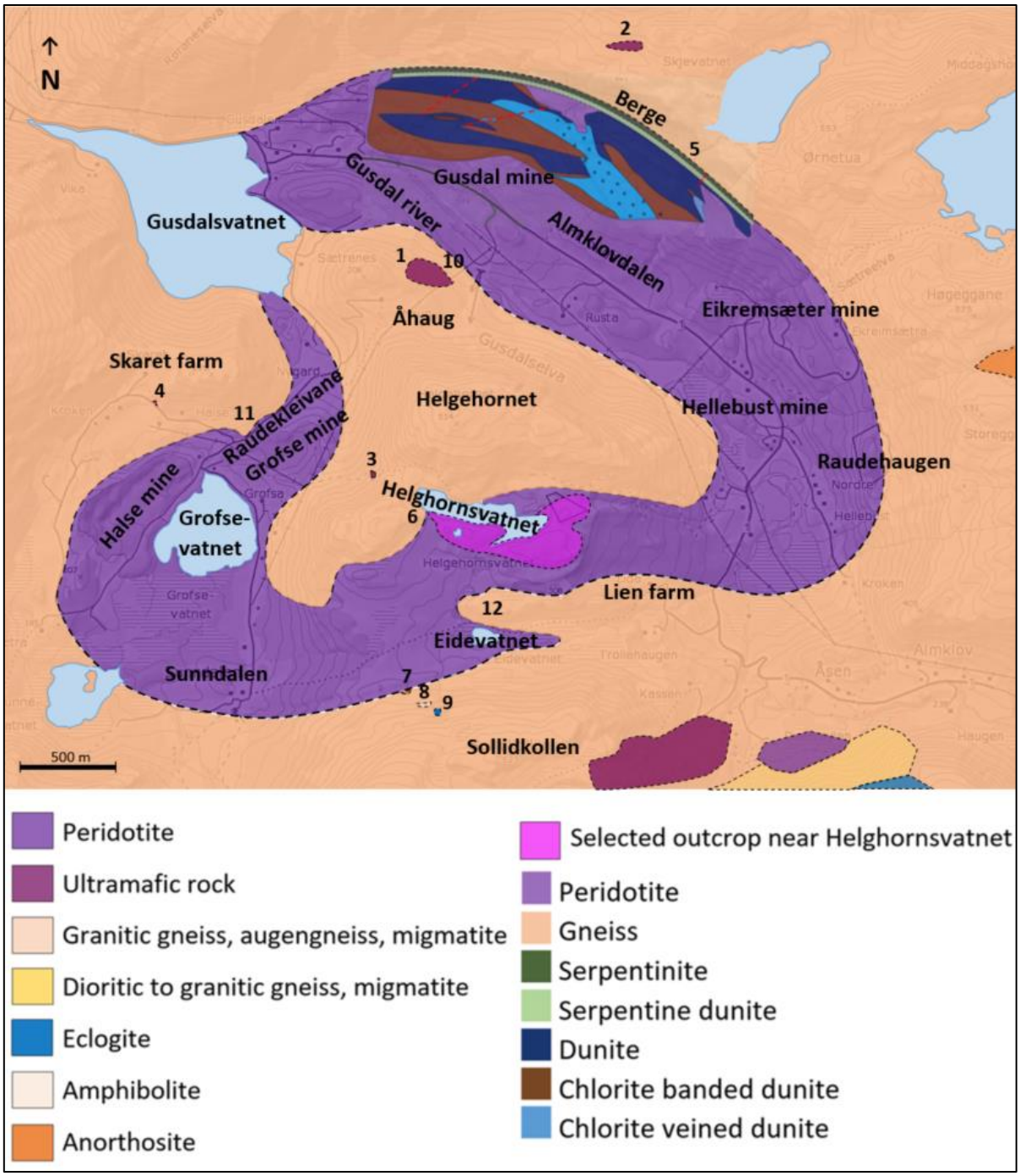

Figure 6.2.3: Zonation within the Gusdal mine area between 15. June to 15. August 2014 illustrated on a large scale geological map of the entire Almklovdalen peridotite massif. Local names used in the Thesis are added on this map.

6.3 Foliation, lineation and folds

A complete geological map of the Almklovdalen peridotite where foliation, lineation, faults and garnet-bearing assemblage are included is provided in Appendix 1.

Dominant foliation in the entire peridotite massif and the surrounding lithologies.

Steeply dipping foliation parallel to the contact against the gneiss is present through the entire peridotite massif and this is considered the dominant foliation (Figure 6.3.1). Osland (1997) defined

this foliation as internal layering in the peridotite. This dominant foliation is considered as penetrative secondary linear foliation and generated by a tectonic fabric along preferred orientation of metamorphic mineral aggregates. Both the gneiss and the peridotites are considered as tectonites. The outline of the peridotite massif was refined by field observations and by measuring this dominant foliation (Figure 6.3.2). This foliation shows strict parallelism to the strike of the contact against the surrounding gneiss and facilitate locating the contact in the field. No seismic survey providing data from deeper levels than <30 m has been done on the massif so the interpretation provided from foliation at the contact zone is the presently only indication of vertical extent. The purpose of measuring the main foliation was also to localize structural elements deviating from the general trend. Such deviations were only found at the selected field area near Helghornsvatnet (Figure 6.3.4).

Figure 6.3.1: Weathered surface south of Helghornsvatnet illustrating the dominant foliation in the Almklovdalen peridotite massif.

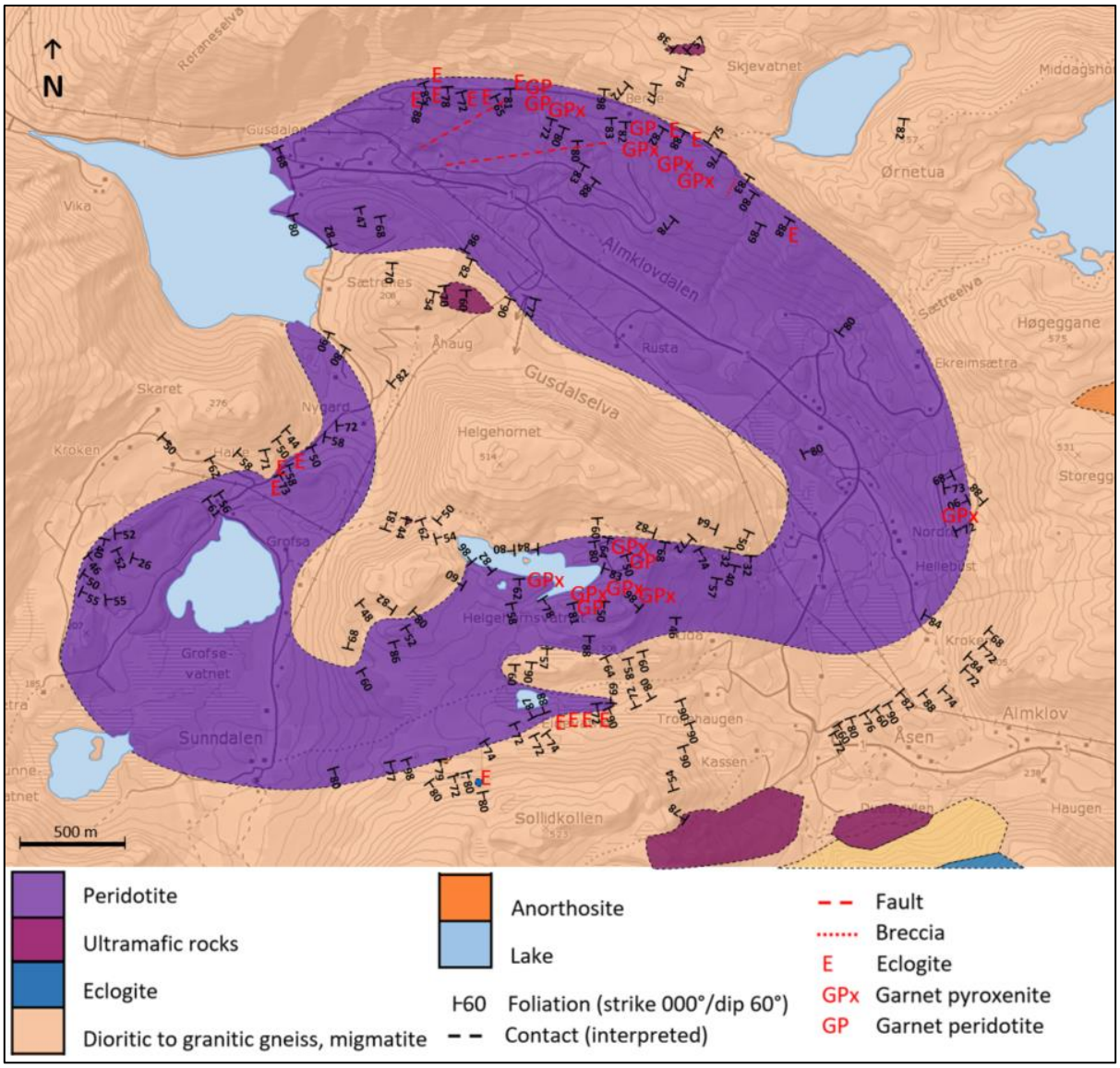

Figure 6.3.2: Geological map illustrating the extent of the contact zone against the surrounding gneisses, dominant foliation and distribution of garnet-bearing assemblages.

Lineation in the entire peridotite massif and the surrounding lithologies.

The lineation was not measured during this survey but the lineation from Cordellier et al. (1981) was plotted in the geological map constructed for this Thesis (Figure 6.3.3). This was done due to limited access of accurate data and the data is plotted by the same symbols as the original. It should be kept in mind that this map is a modified version constructed by copying data presented on a hand-drawn sketch and do not represent accurate field measurements such as the rest of the results.

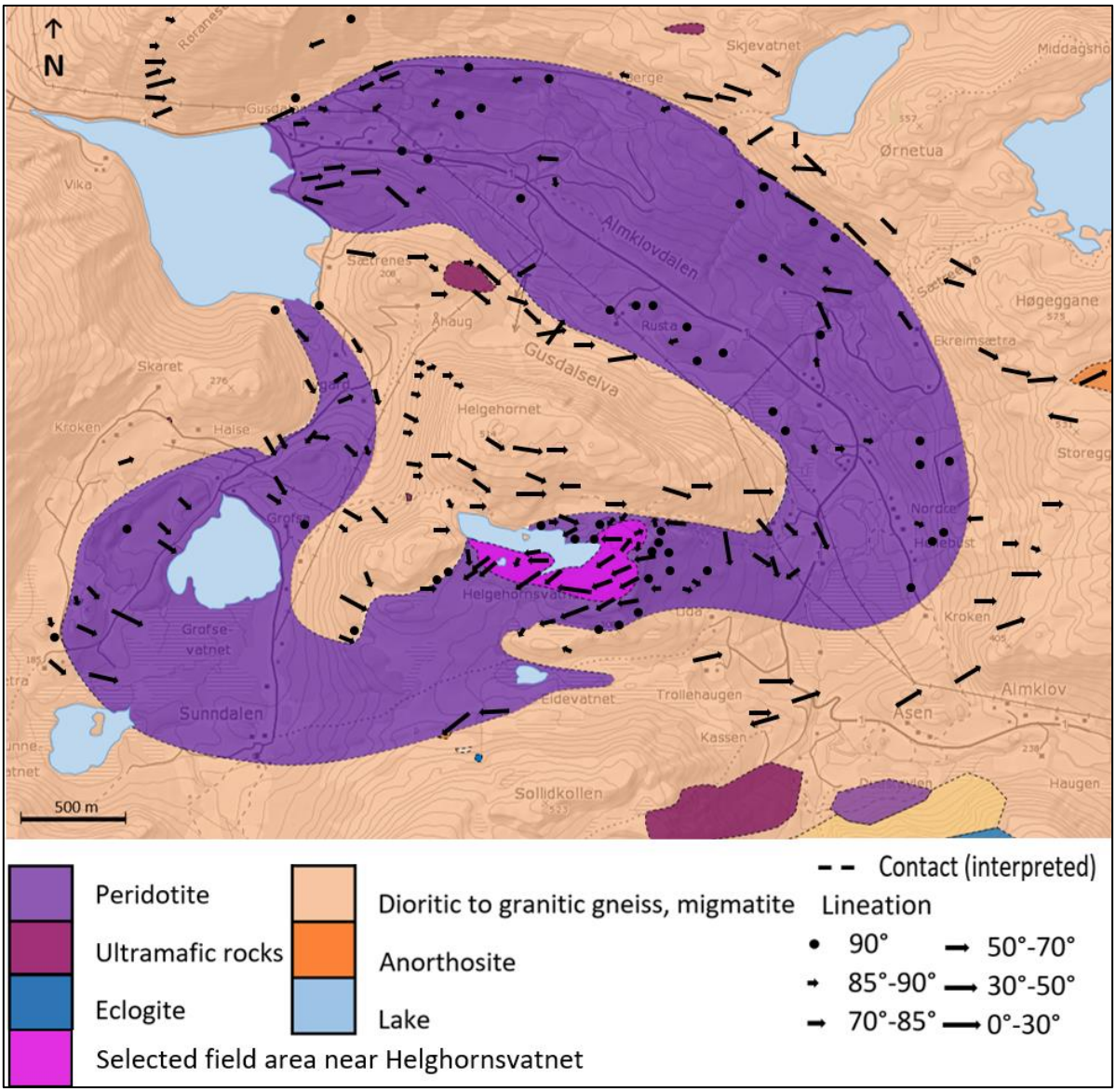

Figure 6.3.3: Geological map showing the lineation in the Almklovdalen peridotite massif and surrounding gneiss. Modified from Cordellier et al. (1981).

Dominant foliation at the field area near Helghornsvatnet

A geological map with dominant foliation at the field area near Helghornsvatnet is provided in Figure 6.3.4. From this map a vertical profile A-A` was constructed from interpreting surface structures and lithological elements (Figure 6.3.5). The main foliation within this area also shows a general parallelism to the contact but the variation is larger than in other areas of the peridotite massif where foliation was measured. In addition, this dominant crystallographic foliation seems to be related to the orientation of all fold categories present at this location. A stereonet was constructed by using equal area projection for the dominant foliation within the selected field area at Helghornsvatnet and the dominant foliation in the surrounding peridotite and gneiss (Figure 6.3.6). Dominant foliation within the field area at Helghornsvatnet and orientations of the axial planes of all fold categories was compared by using the same procedure (Figure 6.3.7). The fold geometry and categories will be described further below.

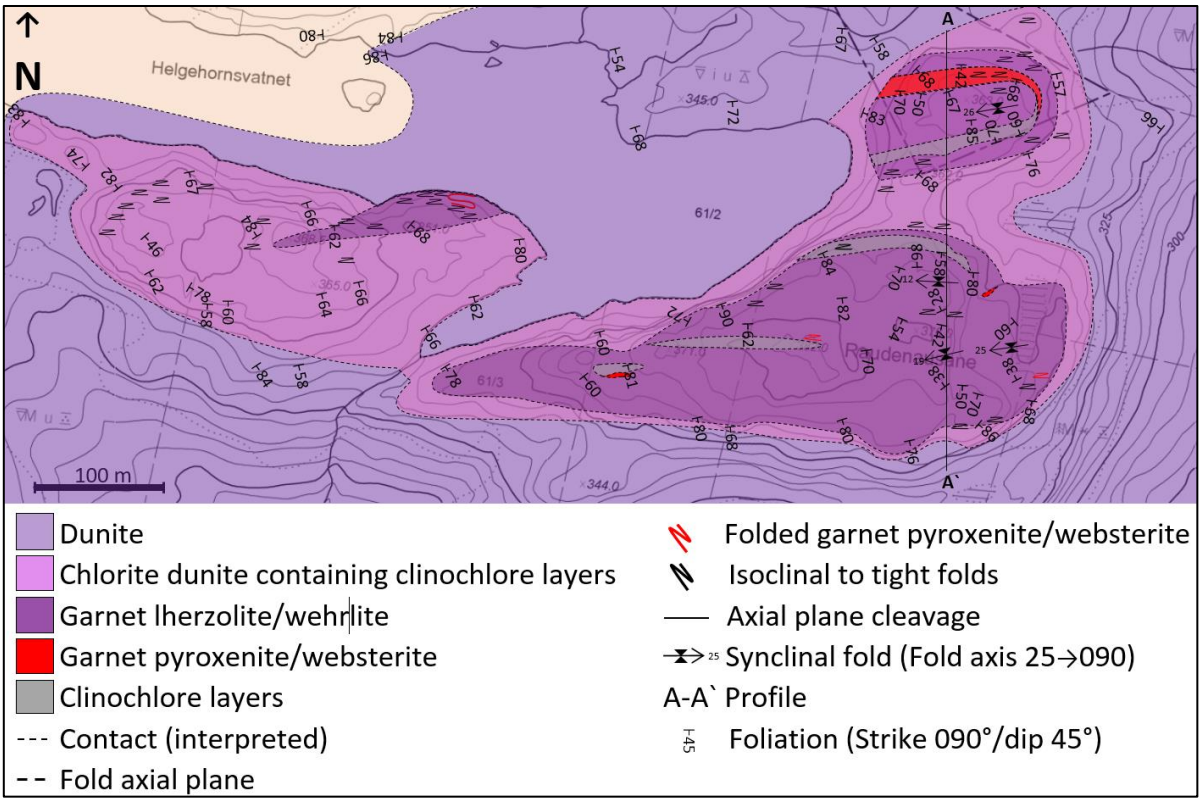

Figure 6.3.4: Geological map of the field area near Helghornsvatnet illustrating foliation, folds, lithologies and distribution of garnet-bearing assemblages.

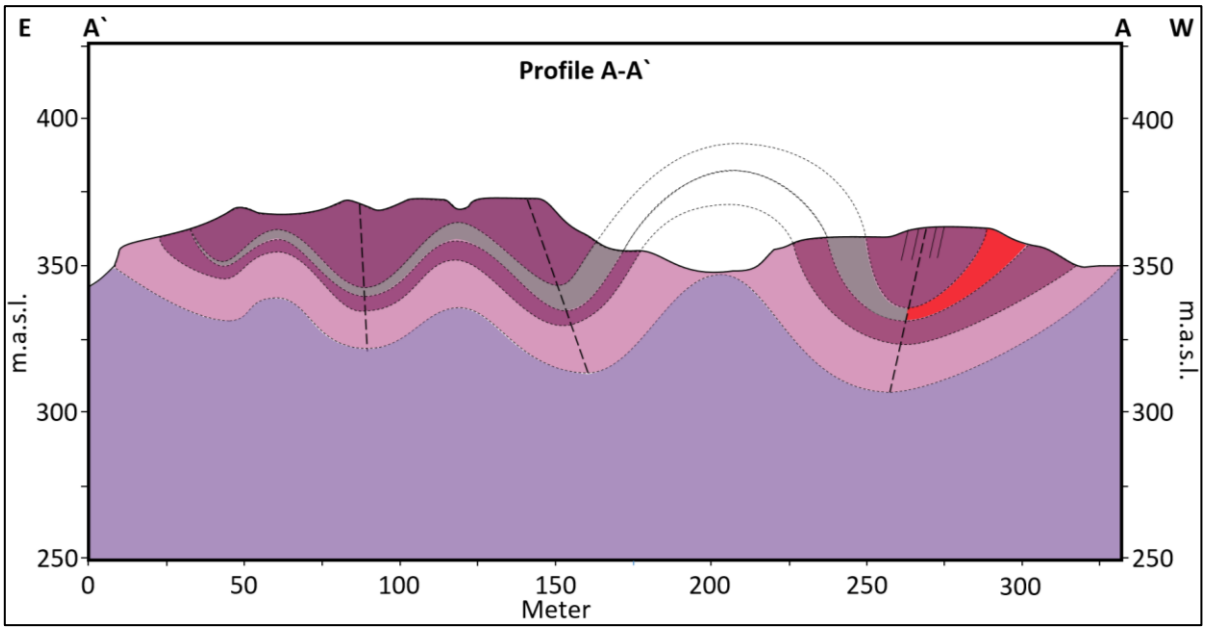

Figure 6.3.5: Profile A-A` interpreted from the geological map in Figure 6.3.4. The colors and symbols correspond to the legend provided with the map in Figure 6.3.4.

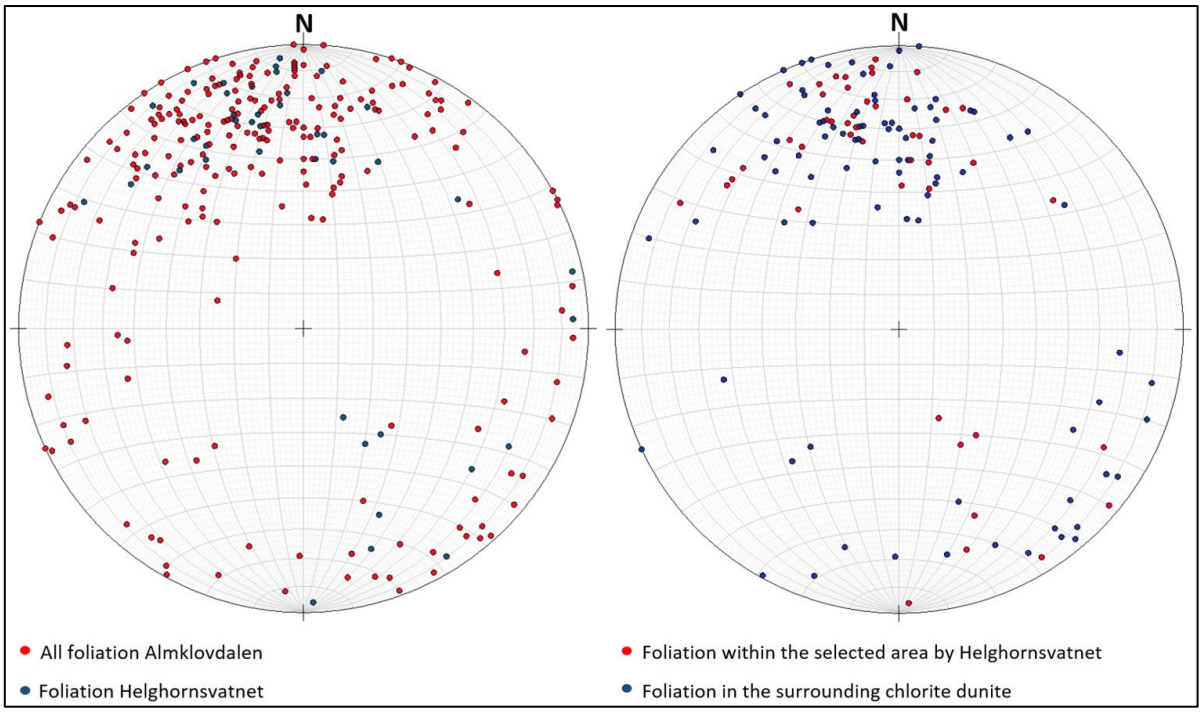

Figure 6.3.6: Left: Stereonet where poles to the dominant foliation from the entire peridotite massif and the surrounding gneiss in proximity to the contact zone are compared with poles to the dominant foliation within the selected field area at Helghornsvatnet and the surrounding chlorite dunite. Right: Stereonet where poles to the dominant foliation within the selected field area near Helghornsvatnet are compared with poles to the dominant foliation in the surrounding chlorite dunite.

Poles to the dominant foliation in the peridotite at Almklovdalen spread out in the stereonet due to parallelism between the contact and the foliation (left stereonet Figure 6.3.6). The approximately oval shape of the peridotite massif (Figure 6.3.2) will cause the strike of the foliation to scatter in 360°. Distribution of measurements is restricted because some areas are covered by vegetation and sediments. The areas represented by the highest number of measurements are the most investigated and best exposed. Parallelism between the dominant foliation in both gneiss and the peridotite in addition to parallelism between foliation and the contact dividing the two lithologies is apparent in Figure 6.3.2 except from some local deviations. Red circles in the stereonet to the right in Figure 6.3.6 represent poles to the foliation within the chlorite dunite containing clinochlore, garnet peridotite and garnet pyroxenite layers/veins in addition to local masses of garnet lherzolite/wehrlite. Blue circles represent poles to the foliation in the surrounding chlorite dunite. A relatively wide distribution is apparent also in this plot but a correlation between the foliation in the two areas is apparent.

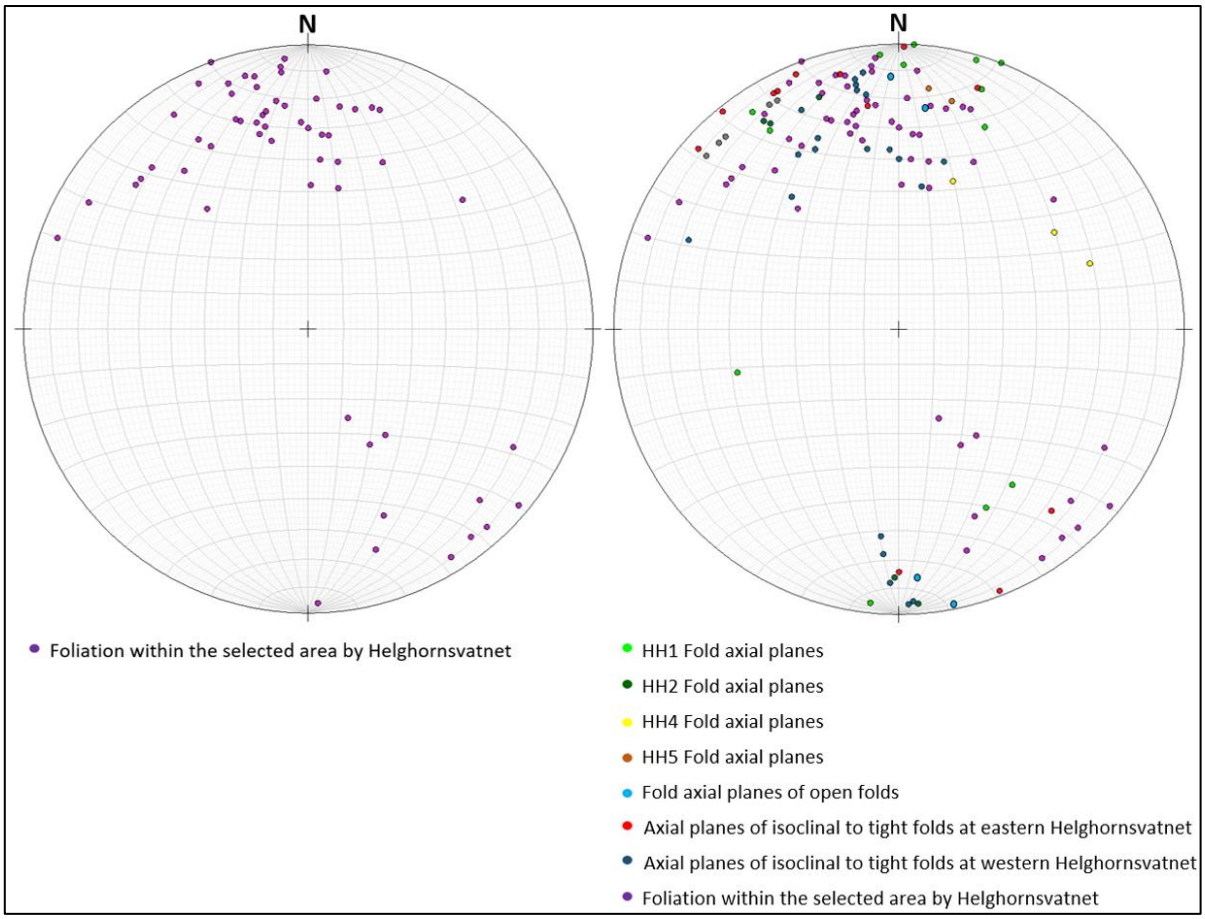

Figure 6.3.7: Left: Stereonet showing poles to dominant foliation within selected field area near Helghornsvatnet. Right: Stereonet where the foliation shown in left stereonet is compared to orientation of axial planes of the folds within selected field area near Helghornsvatnet. HH1 to HH5 represent folded garnet pyroxenite and garnet peridotite.

Poles to the dominant foliation in the selected field area south and east of Helghornsvatnet are plotted in stereonet to the left in Figure 6.3.7. The stereonet to the right in the same figure represents all fold axial plane measurements done within this area. Poles to the fold axial planes spread out within the same field as poles to the foliation and the scattering is approximately of the same order.

Description of folds within the selected field area near Helghornsvatnet

A series of folds at the field area near Helghornsvatnet was mapped and their orientation is significant for interpretations related to deformation in this section of the peridotite massif. The folds are divided into three categories and a description of these are provided below. Classification of the folds based on orientation of the hinge line and the axial surface in addition to interlimb angle are done according to Fossen (2016). Folded areas are indicated on the geological map in Figure 6.3.4.

Category 1 folds: This category include folding that affect clinochlore-rich-, garnet peridotite- and garnet pyroxenite layers in chlorite dunite and garnet lherzolite/wehrlite. These folds are open upright to steeply inclined mesoscopic parallel folds with gently plunging fold axes. In terms of bluntness category 1 folds seems to be relatively cylindrical and harmonic at <10 m scale but are considered non-cylindrical and disharmonic at larger (>10 m) scale. They are further generally considered as non-symmetrical and south vergent. The shortening direction of category 1 folds are

N-S and their fold axes are plunging to the west. Their orientations are plotted in a stereonet provided in Figure 6.3.10 and the stereonet is related to their locations on the geological map in Figure 6.3.13. Only the synclinal category 1 folds were properly exposed and therefore no anticlinal folds were added on this map. Figure 6.3.8 provide a photo illustrating the geometrical pattern of the south-easternmost category 1 fold in Figure 6.3.4. The north-south vertical profile along the line denoted A-A` on the geological map provided in Figure 6.3.4 illustrate the occurrence of category 1 folds in addition to the interpreted vertical extent of the lithologies at the field area near Helghornsvatnet (Figure 6.3.5). Penetrative axial plane cleavage where dip isogons converge towards the inner arc was observed in the northernmost category 1 fold near the HH1 and HH2 localities. A photo of the axial plane cleavage is provided in Figure 6.3.21 and its orientations are plotted in the stereonet in Figure 6.3.22.

Figure 6.3.8: Photo illustrating the pattern of the south-easternmost category 1 fold at the field area near Helghornsvatnet.

Category 2 folds: This category include folding that affect clinochlore-rich layers in chlorite dunite and garnet lherzolite/wehrlite. They are isoclinal to tight macro to mesoscopic folds. Their orientations are upright to gently inclined with horizontal to steeply plunging fold axes. In terms of bluntness category 2 folds are considered non-cylindrical and asymmetrical at a scale of <1 m. They are further generally considered as non-symmetrical although symmetry can be observed at some locations. They are both N-NW and S-SE vergent. The shortening direction of the category 2 folds are orientated from N-S to NW-SE and the plunge of their fold axes varies from north-east to south to west. These folds seem to have axial planes largely parallel to the dominant foliation. Well-developed box folds are relatively common. Stereonets with poles to their axial plane orientations and their fold axes are provided in Figure 6.3.11 and a photo of typical category 2 folds are provided in Figure 6.3.9.

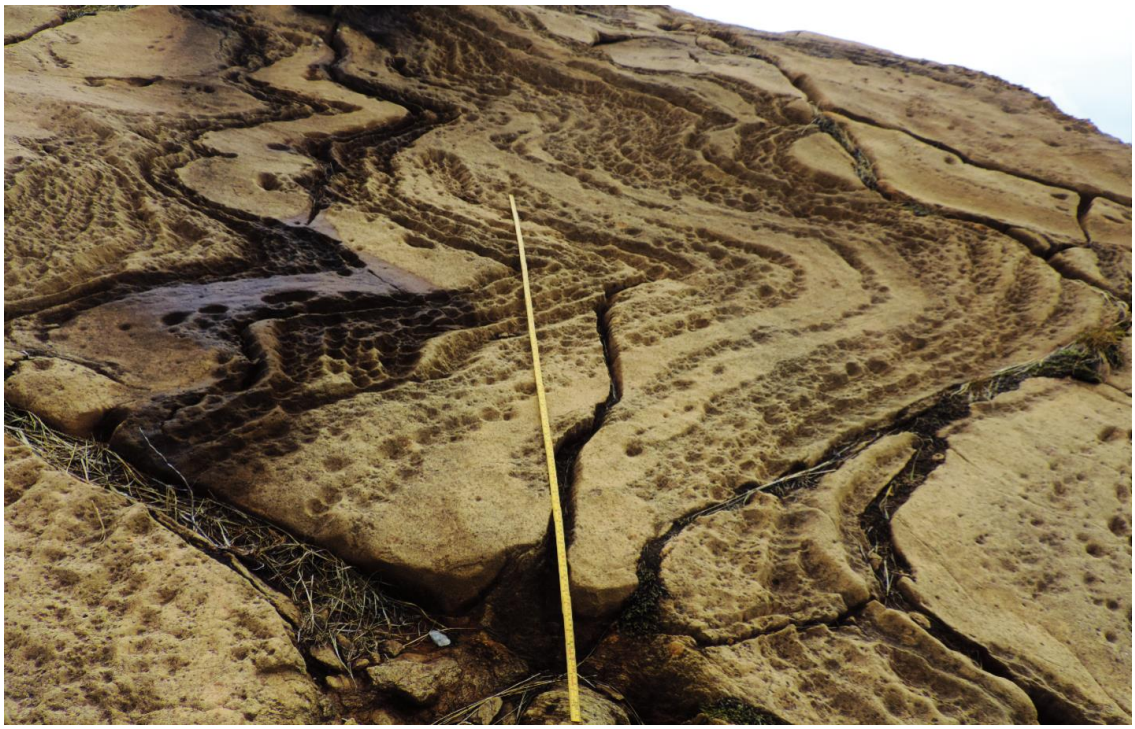

Figure 6.3.9: Photo illustrating the pattern of category 2 folds at the field area near Helghornsvatnet (scale=2 m).

Category 3 folds: This category include folds that affect garnet peridotite- and garnet pyroxenite layers in chlorite dunite and garnet lherzolite/wehrlite. They are gentle to tight meso- to macroscopic parallel folds. Their orientations are upright to steeply inclined with horizontal to steeply plunging fold axes. In terms of bluntness category 3 folds are considered non-cylindrical and disharmonic at larger scale than >1 m. Both the vergence, the shortening direction and plunge of the fold axes of category 3 folds seem to vary largely. Stereonets with poles to their axial plane orientations and fold axes are plotted in a stereonet provided in Figure 6.3.12 and the stereonets is related to their locations in Figure 6.3.13. Locations that contains category 3 folds are abbreviated HH1, HH2, HH4, HH5 and measurements presented for these locations represent only these lithologies. Figure 6.3.17 and Figure 6.3.19 contains photos illustrating the pattern of category 3 folds at the HH1 and HH2 locations.

Various combinations of axial plane and fold axis orientations are illustrated by using equal area projection in Schmidt nets. Figure 6.3.13 provides a geological map in which stereonets showing poles to fold axial planes and fold axes orientations of category 1 and 3 are related to locations within the field area near Helghornsvatnet. Stereonets showing poles to axial planes and fold axes orientations of all folds plotted together are provided in Figure 6.3.15. Locations HH1 and HH2 were additionally mapped in detail and geological maps, vertical profile sketches and photos are provided for these locations. Figure 6.3.16 and Figure 6.3.17 represent HH1. Figure 6.3.18 and Figure 6.3.19 represent HH2.

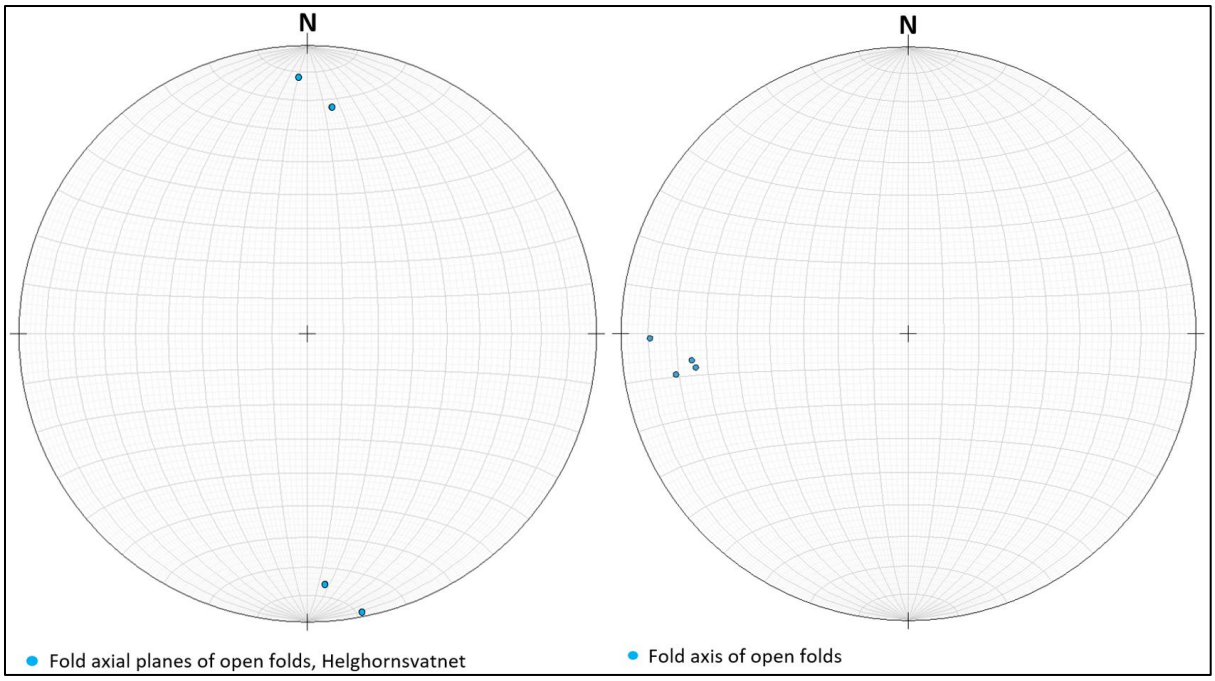

Figure 6.3.10: Stereonets showing poles to axial planes and fold axes of category 1 folds at the selected field area near Helghornsvatnet.

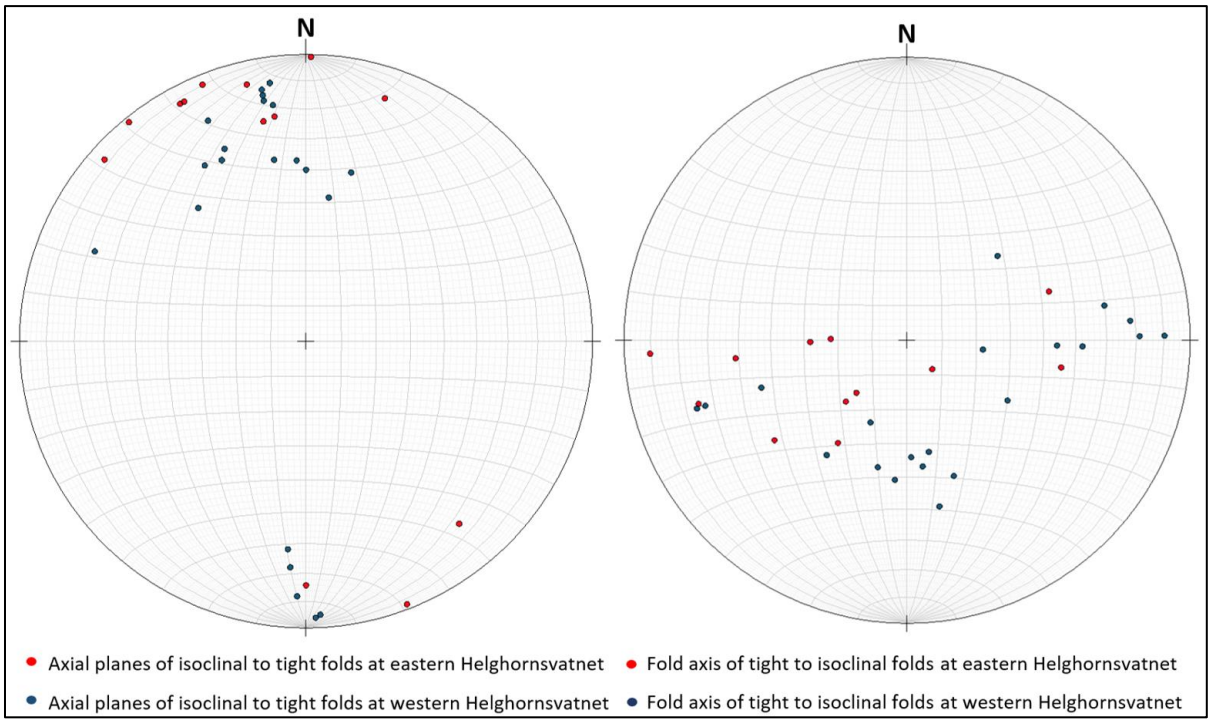

Figure 6.3.11: Stereonets showing poles to axial planes and fold axes of category 2 folds at the selected field area near Helghornsvatnet.

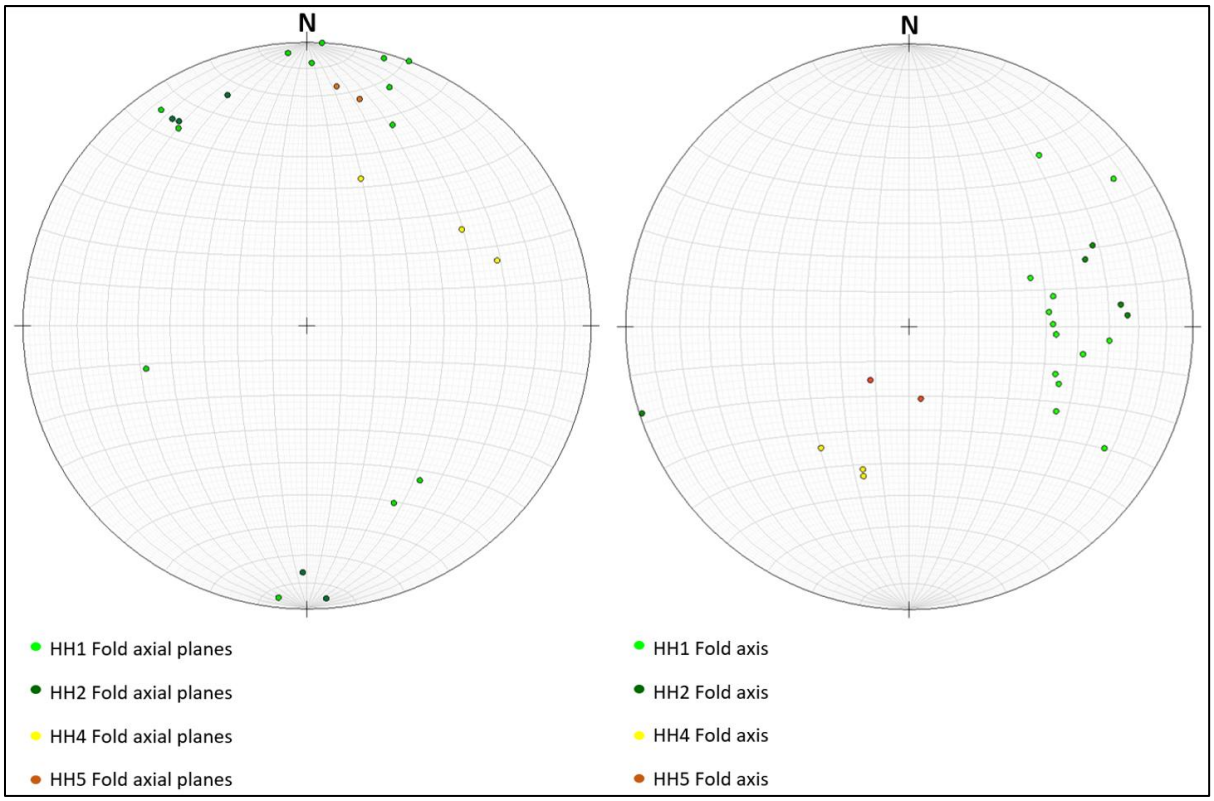

Figure 6.3.12: Stereonets showing poles to axial planes and fold axes of category 3 folds at the HH1, HH2, HH3 and HH5 locations near Helghornsvatnet.

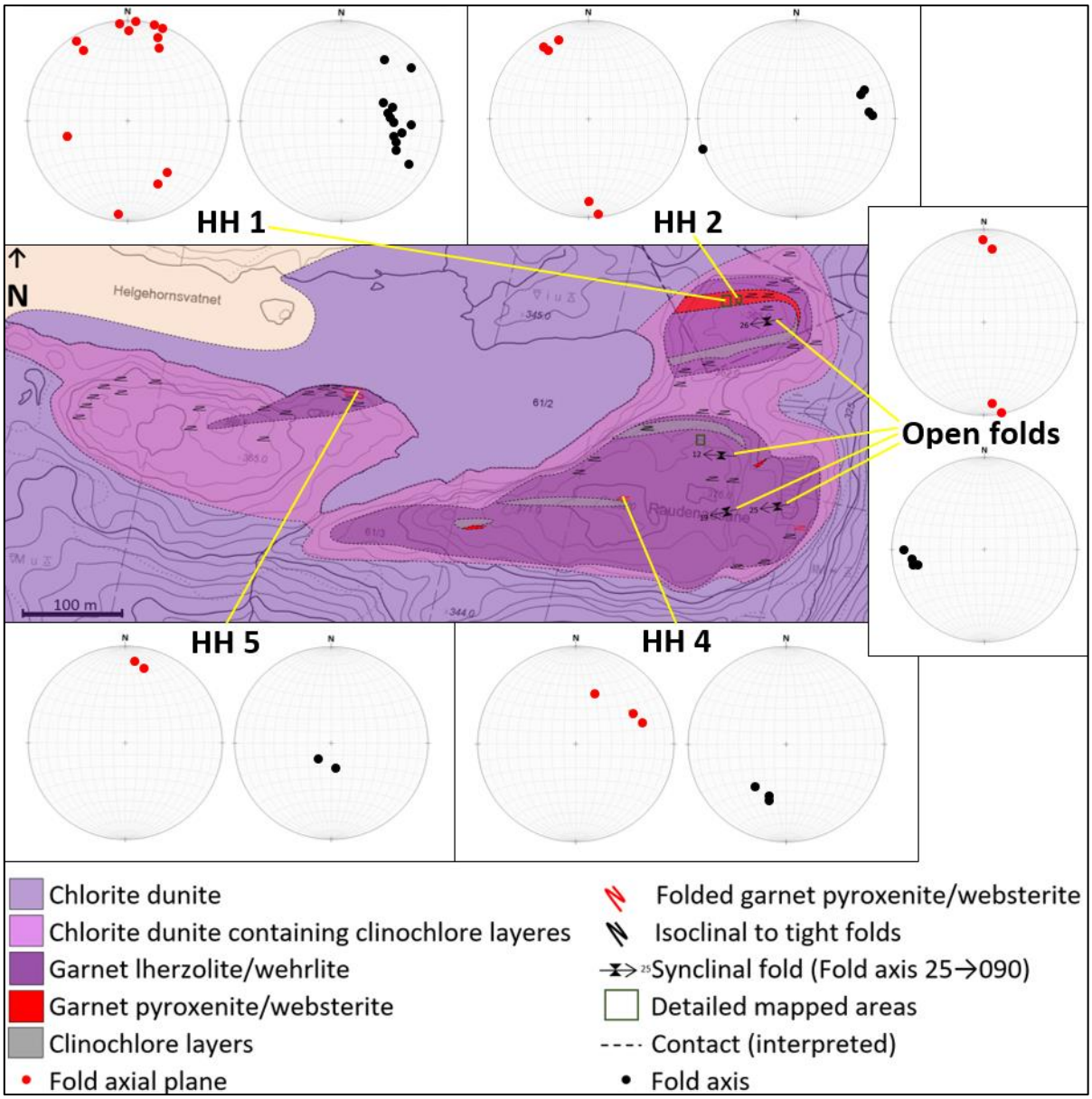

Figure 6.3.13: Geological map on which stereonets showing poles to fold axial planes and fold axes of category 1 and 3 folds are related to their locations within the field area near Helghornsvatnet.

Fold axial planes and fold axis orientations of category 3 folds at HH1 and HH2 seems to correlate to each other to a degree and represents folding of a category 1 fold hinge. Fold axial plane orientations of the category 1 folds correspond roughly to the latter but fold axes are plunging to the west while the HH1 fold axes plunge vary from NE to SE. The HH2 fold axes plunge to the NE-E with one exception which is horizontal roughly orientated towards the SW. Figure 6.3.14 illustrate category 2 folds in the fold hinge of a category 3 fold at the HH5 locality. Figure 6.3.16, Figure 6.3.17, Figure 6.3.18 and Figure 6.3.19 illustrates category 3 folds occurring in the hinges of a category 1 fold. Category 3 folds have steeper plunging fold axes towards the S to SE at the HH4 and HH5 locations compared to the HH1 and HH2 locations. However, when the orientations of category 3 folds at the HH1, HH2, HH4 and HH5 locations are compared with the orientations of the category 2 folds, they fall within roughly the same distribution area (Figure 6.3.15). At location HH5 a series of category 2 folds occur along the fold hinge of a category 3 fold (Figure 6.3.14). Complex fold patterns of category 2 folds continue westwards from the HH5 location along a sub-vertical E-W oriented ridge

with low accessibility, but no large deviation from the other category 2 folds were observed. Category 2 folds are the most common and orientations of these folds are more widely distributed and give an indication of the potential internal variation in orientation within an individual fold category. Even when considering the lack of symmetry, harmony and cylindricity, category 3 folds still show relatively large deviation in orientation compared to the category 2 folds. The shortening direction seem to vary among the fold categories, which indicate that the folds are orientated slightly different.

Figure 6.3.14: Photo of a series of category 2 folds occurring along the fold hinges of a category 3 fold at location HH5 (Figure 6.3.13).

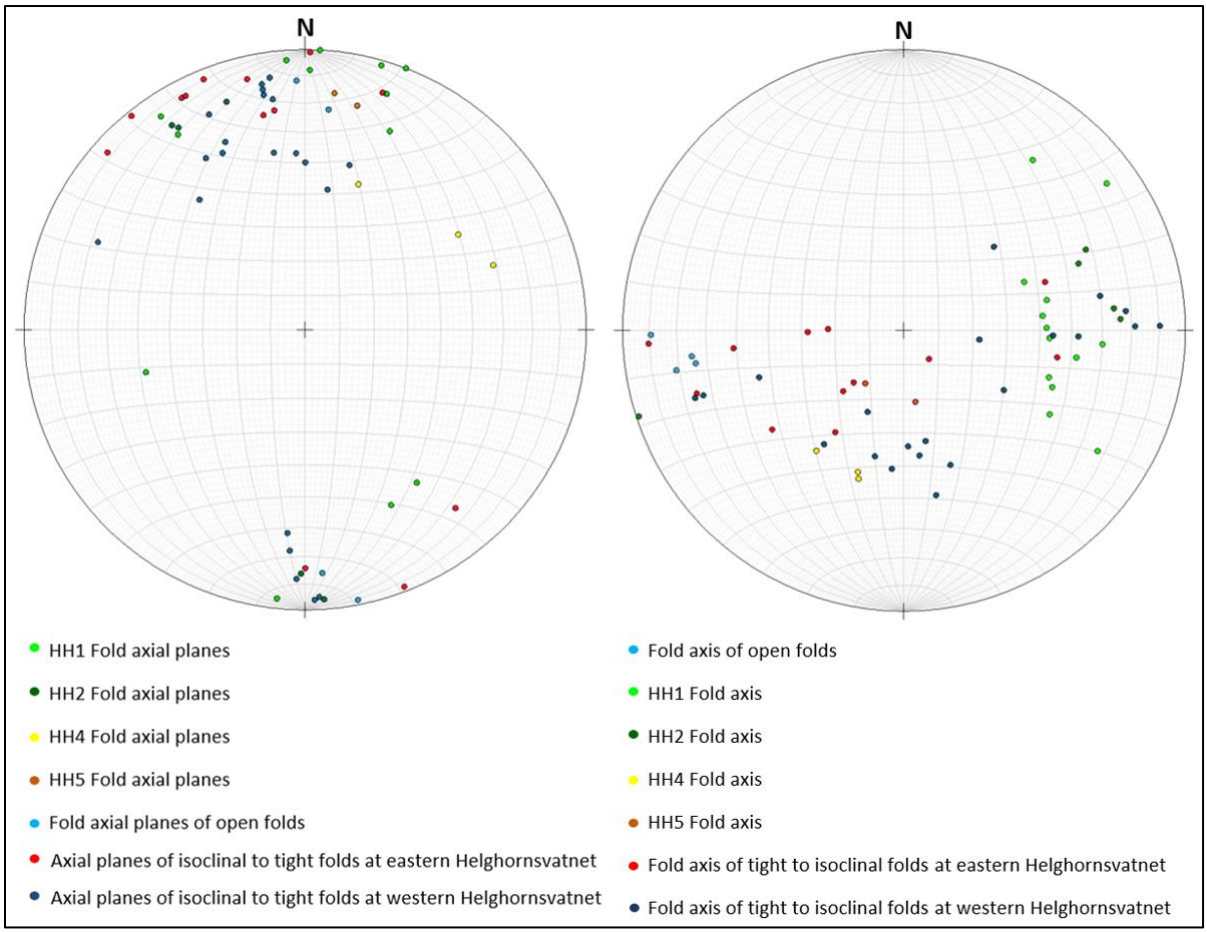

Figure 6.3.15: Stereonets where poles to axial planes and fold axis orientations of all folds within the field area near Helghornsvatnet are compared.

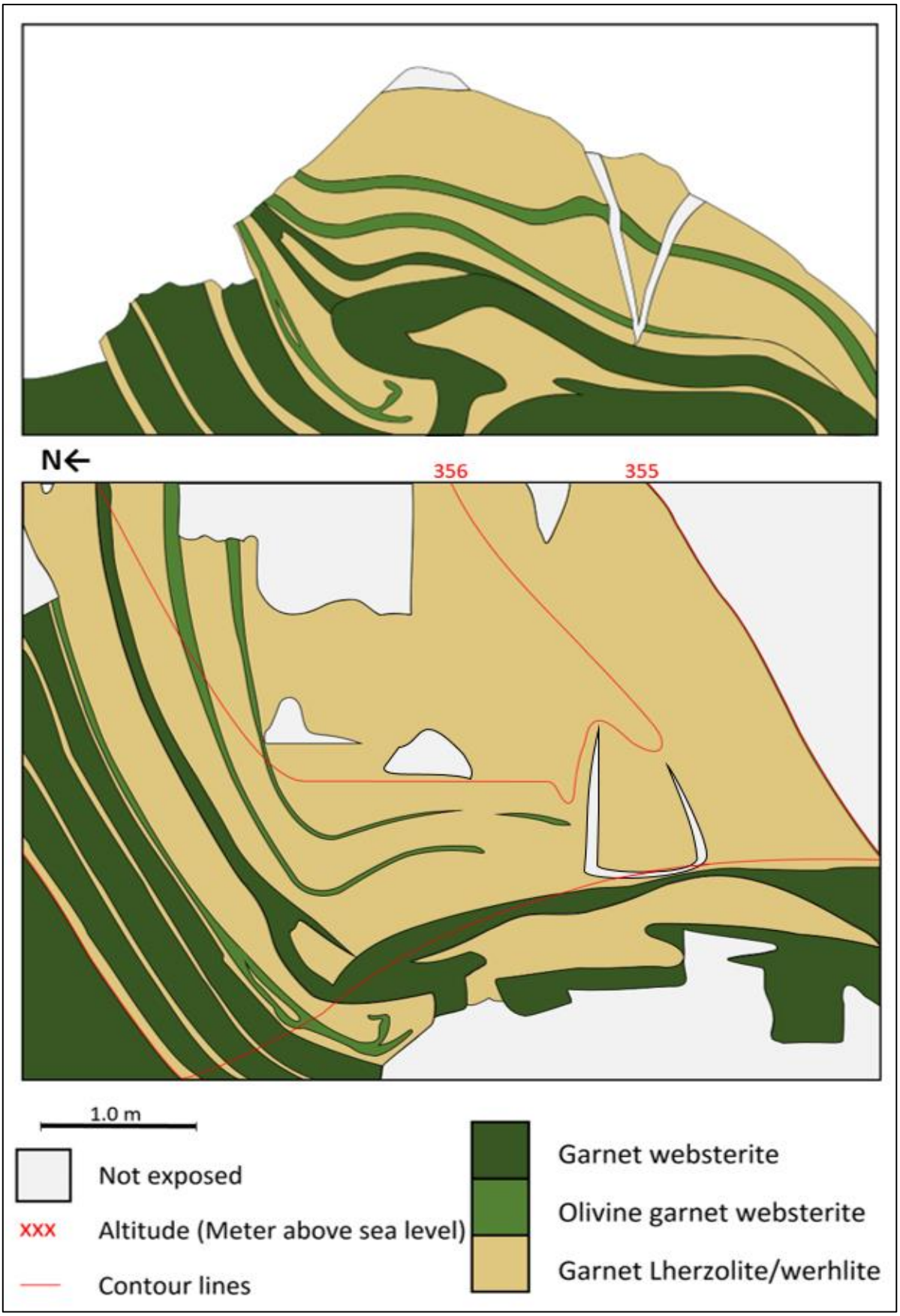

Figure 6.3.16: Geological map (lower) and vertical profile sketches (upper) of the HH1 location (Figure 6.3.13).

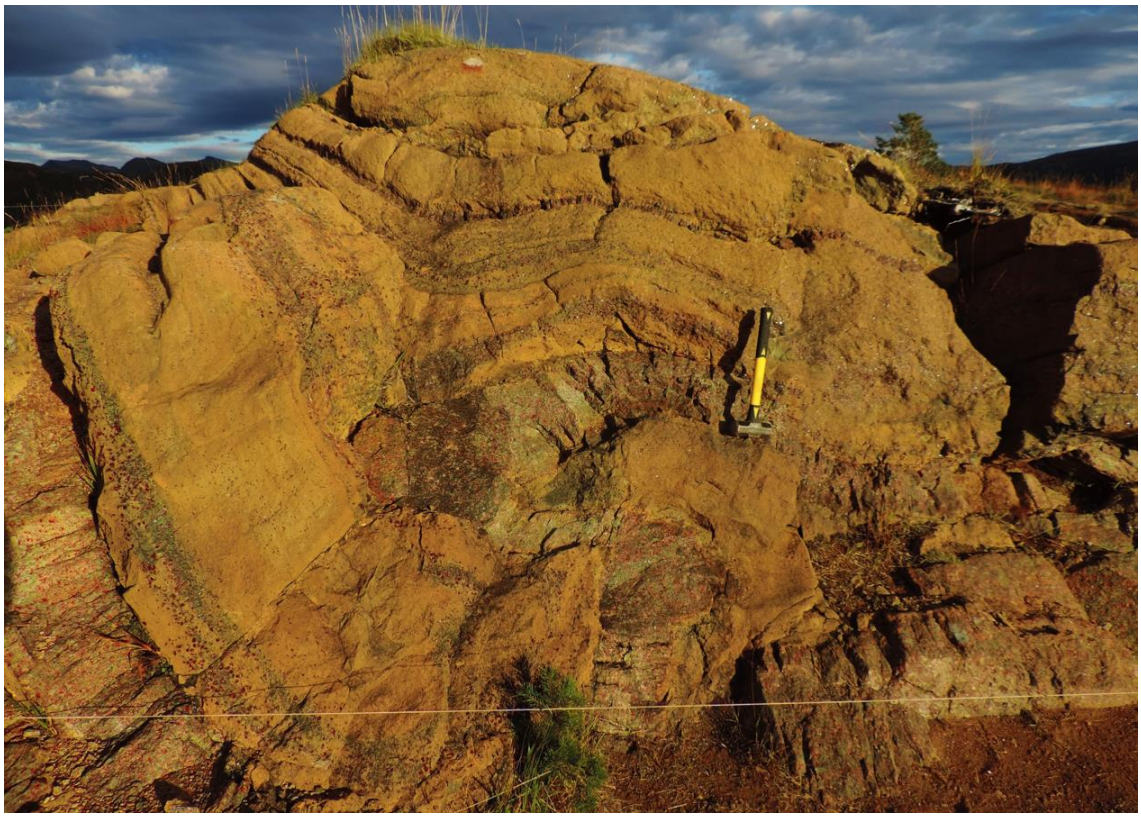

Figure 6.3.17: Photo of fold pattern at the HH1 location.

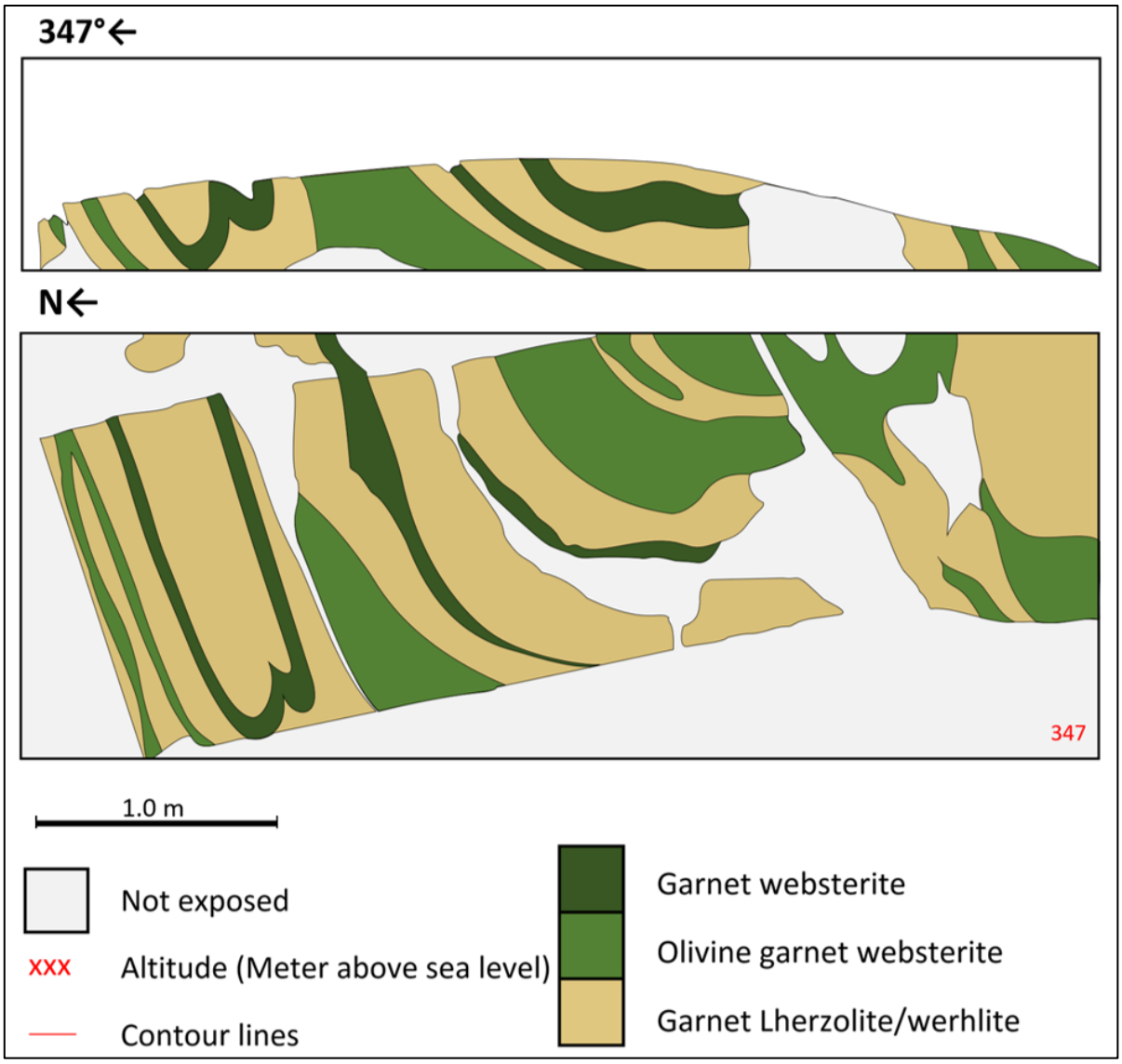

Figure 6.3.18: Geological map (lower) and vertical profile sketch (upper) of the HH2 location (Figure 6.3.13).

Figure 6.3.19: Photo of fold pattern at the HH2 location.

An abrupt change in the orientation of the clinochlore layers, and more complex deformation features was observed in a few locations. Photos of these features are presented in Figure 6.3.20 where the upper left and right photos show the abrupt change in orientation of the clinochlore layers. Lower left and right photos show more complex deformation. Another apparent feature is a cleavage perpendicular to the shortening axis in the fold core of a category 1 fold east of the HH1 and HH2 localities (Figure 6.3.21). A stereonet showing poles to the abruptly changed orientation of the clinochlore layers and the cleavage in the category 1 fold are provided in Figure 6.3.22.

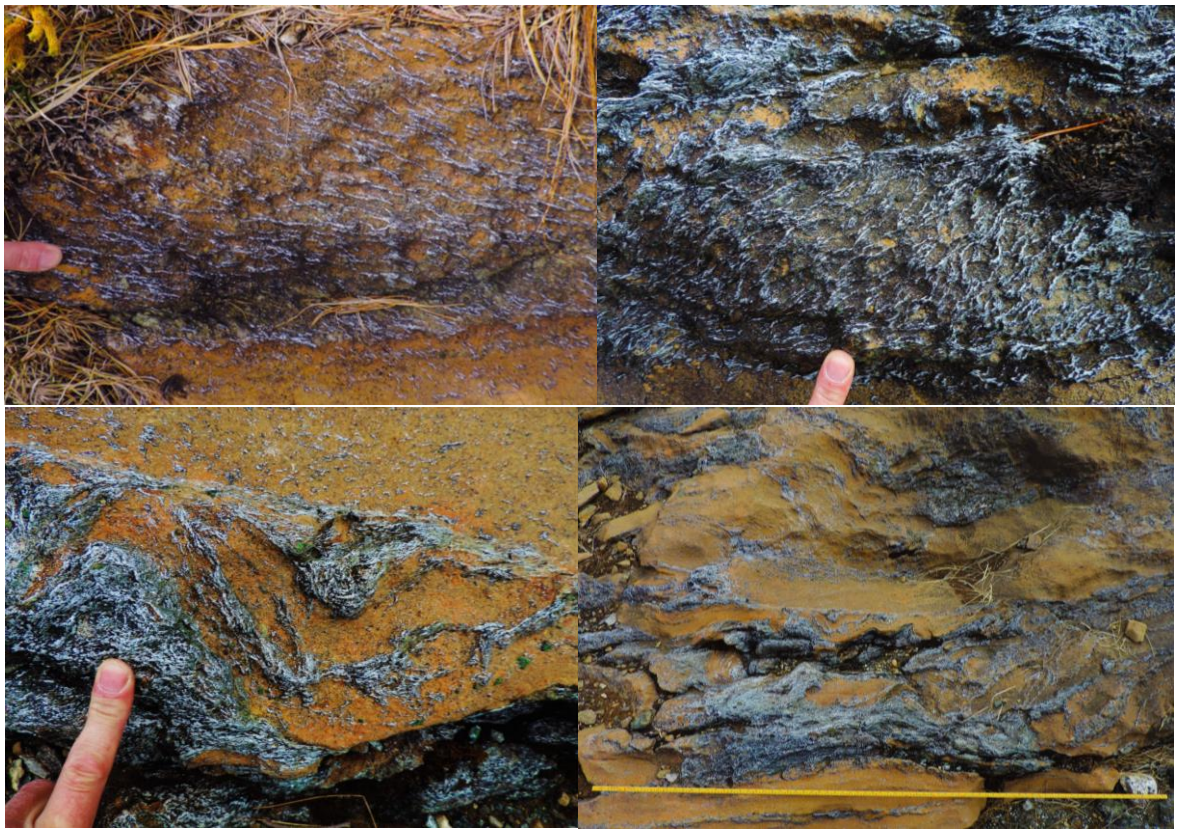

Figure 6.3.20: Photos of the abrupt change in orientation (upper left and right) and the more complex deformation patterns (lower left and right) of clinochlore layers.

Figure 6.3.21: Photo of the cleavage in the fold core of a category 1 fold east of HH1 and HH2.

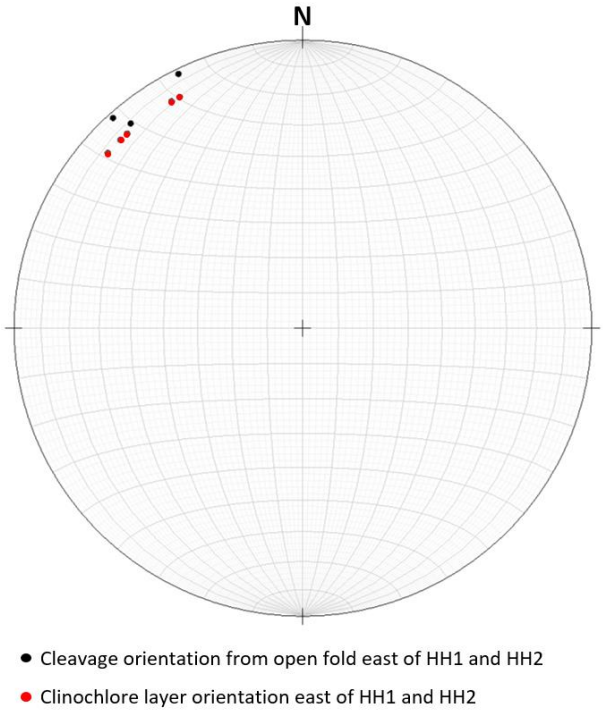

Figure 6.3.22: Stereonet showing poles to orientation of the cleavage in the core of the category 1 fold east of HH1 and HH2 and poles to the orientations of the abruptly changed clinochlore layers.

Faults and fractures

Extensive faulting and fracturing has occurred along slip-planes parallel to the dominant foliation. The magnitude of the movements on these deformation features is not measurable due to lack of kinematic indicators. Slickensides were observed in the serpentine rims on fault planes, providing indicators of the orientation of the movement. The orientation varies from vertical to horizontal and no systematic trends were detected. Two mesoscopic brittle faults with general strikes of approximately 210° and 190° are of specific importance to the product quality due to their permeability and connectivity; fluid percolation resulted in hydration of the peridotite (Figure 6.3.2). Orientation of these faults are provided in the stereonet in Figure 6.3.23. A fault breccia occurs in the northern wall of Gusdal quarry and appears to be of brittle nature only affected by low degrees of hydrothermal activity. The hydrothermal fluids deposited a white crust on the fracture surfaces and only small fraction of this crust show reaction with 1 molar hydrochloric acid (HCl). The rock-type at this location is serpentinite and mineral phases occurring as white crust are suggested to be chlorite (kammererite $Mg_5(Al,Cr)_2Si_3O_{10}(OH)_8$ analyzed by Sibelco Nordic at other locations in the Gusdal mine) and talc in addition to minor amounts of various carbonate mineralization. Another interesting aspect is that the brecciated zone does not continue into the gneiss but ends abruptly at the contact. This indicates that this structure was generated by a brittle deformation process that only effected the peridotite and not the gneiss. The breccia is 0.5 m wide at the top and 6 m wide at the contact against the gneiss. The orientation of the fault breccia is provided in the stereonet in Figure 6.3.23 and a photo of the fault breccia is provided in Figure 6.3.24.

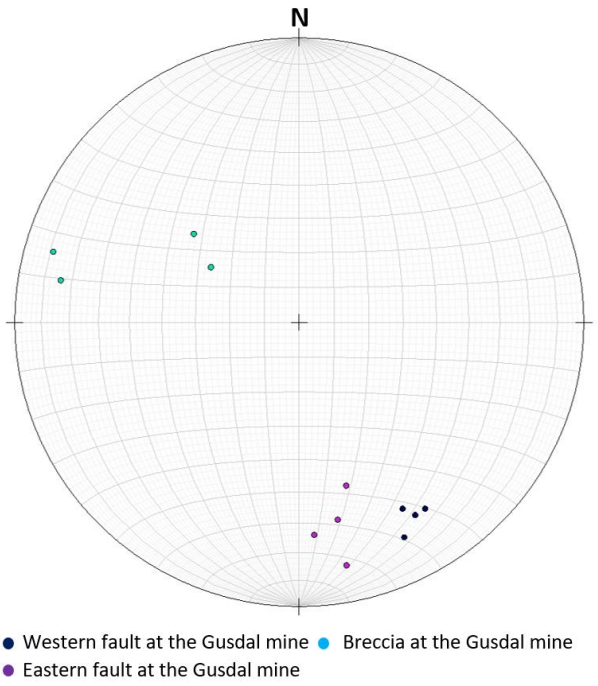

Figure 6.3.23: Stereonet showing poles to the orientation of the two large scale brittle faults and the fault breccia at the Gusdal mine.

Figure 6.3.24: Photo of the fault breccia at the Gusdal mine. The purple to bluish mineralization is the kammererite.

Hydration

Serpentinization develops by chemical alteration of olivine reacting with aqueous silica intruding from the gneiss. The general formula is:

$$3Mg_2SiO_4 + SiO_2 + 4H_2O \rightarrow 2Mg_3Si_2O_5(OH)_4$$

During this process the MgO content decreases, the L.O.I. increases and the Fe content is altered to magnetite. Hydration also causes an increase in competence and hardness of the dunite. Non-penetrative serpentinization is widespread as thin layers on fault planes and fracture surfaces. Penetrative serpentinization is found in a 30-70 m wide zone along the contact against the surrounding gneiss along the whole peridotite massif. The degree of serpentinization decreases gradually from the contact towards the interior of the massif. A generation of fluid percolation in the internal part of the massif has occurred in restricted zones and is marked by minor penetrative alteration of dunite. These restricted zones surrounding the major faults marked on the map in Figure 6.3.2. The dunite near to the zones where silica-rich fluids have percolated has a slightly darker green to gray color in contrast to the light green color of the zones not effected by hydration (Figure 6.3.25).

Figure 6.3.25: Slightly darker green to gray colored dunite affected by silica-rich fluids in contrast to the light green color of the zones not effected by hydration.

Fibrous minerals are occasionally found in the fault and fracture zones and related to serpentinization. Such minerals are remarkably rare in the Gusdal open mine but occur sporadically throughout the peridotite massif. Two smaller ultramafic bodies occur as separate lenses in the gneiss to the north and to the south of the Gusdal open pit mine were mined for fibrous mineral for a relatively short time. These bodies and a few locations within the Almklovdalen peridotite show the importance of fluid percolation combined with fracture and fault development in the formation of fibrous mineral phases.

Semiprecious forsterite gems

Along fault planes at two locations, there are pockets where alteration of forsterite crystals to serpentine and talc has occurred. Within the talc matrix and on the walls of these spaces, relics of euhedral to subhedral forsterite crystals have been found. Relics of these crystals display the whole sequence from semiprecious forsterite to serpentine and talc pseudomorphs. The weight of the crystals described by the miners varies from approximately 6 kg to a few grams. During field work related to this Thesis a transparent subhedral forsterite crystal approximately 4.5 cm high and 1.5 cm wide was found (Figure 6.3.26). Mining for these crystals has occurred at one of these location but was abandoned due to disagreement between miner and landowners. Potential for mining is still present but it is not considered to be economically profitable.

Figure 6.3.26: Transparent subhedral forsterite crystal approximately 4.5 cm high and 1.5 cm wide illustrating alteration from forsterite to talc.

6.4 Sample locations and sample classification by X-ray Diffraction Spectrometry (XRF)

Sample locations

Twelve samples were collected within the selected field area near Helghornsvatnet. Their exact locations are marked at the geological maps in Figure 6.4.1 and Figure 6.4.2. Five samples were collected for analyses within the area of the Gusdal mine and their exact locations are marked at the map in Figure 6.4.3. These samples were used to compare the lithology in the Gusdal mine to the mapped field area near Helghornsvatnet. A general overview map of sample locations is provided in Figure 2.2.4.

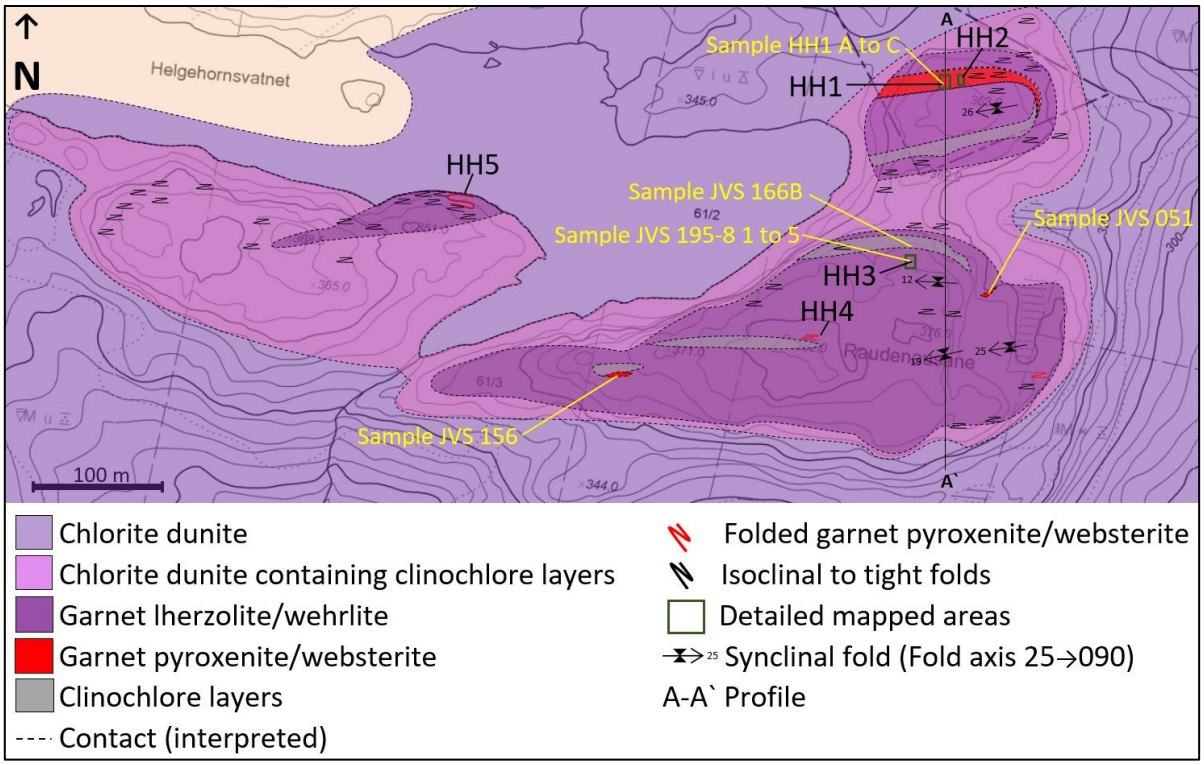

Figure 6.4.1: Geological map of the field are near Helghornsvatnet with detailed sample locations. The locations HH1, HH2 and HH3 are selected for detailed mapping and the locations HH4 and HH5 are selected for structural analyses.

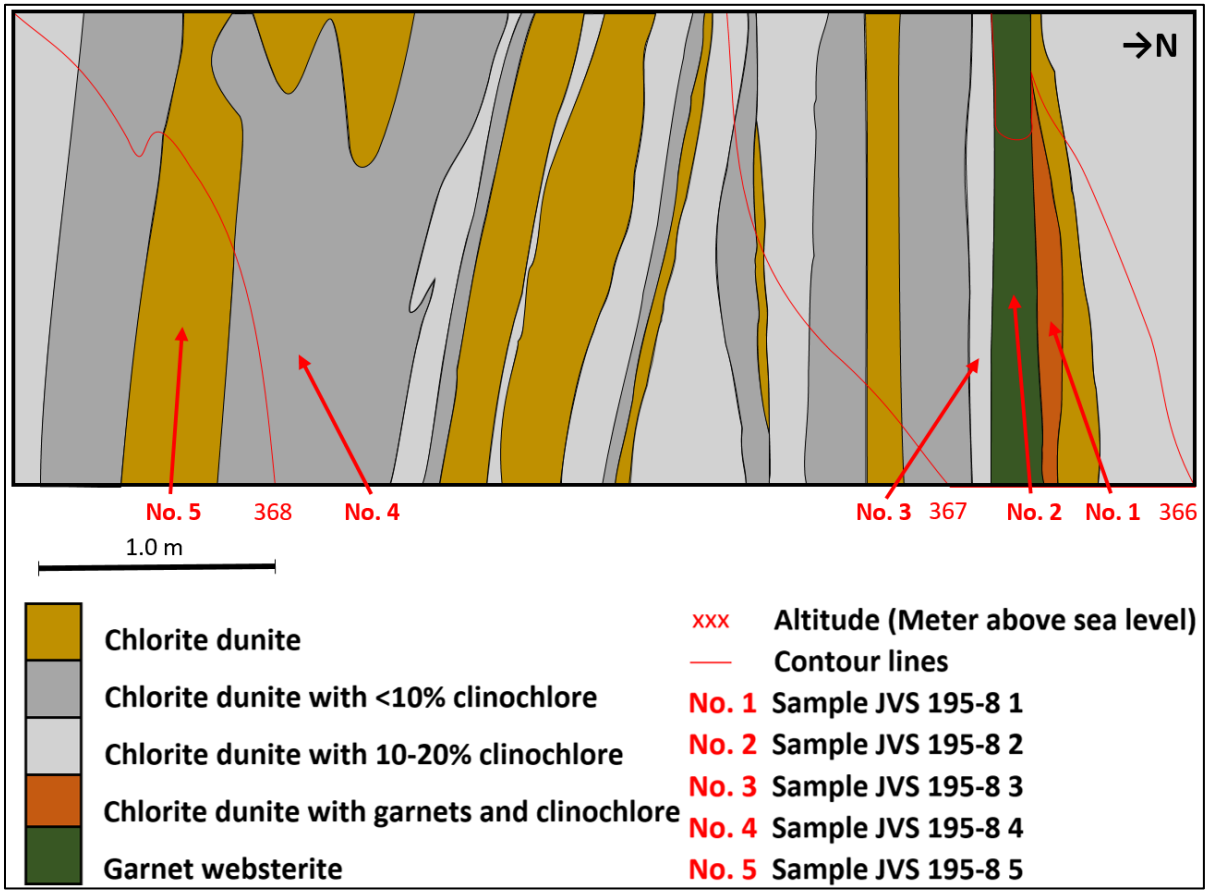

Figure 6.4.2: Detailed geological map of the HH3 locality at the field area near Helghornsvatnet (Figure 6.4.1.) with exact locations for sample JVS 195-8 1 to JVS 195-8 5.

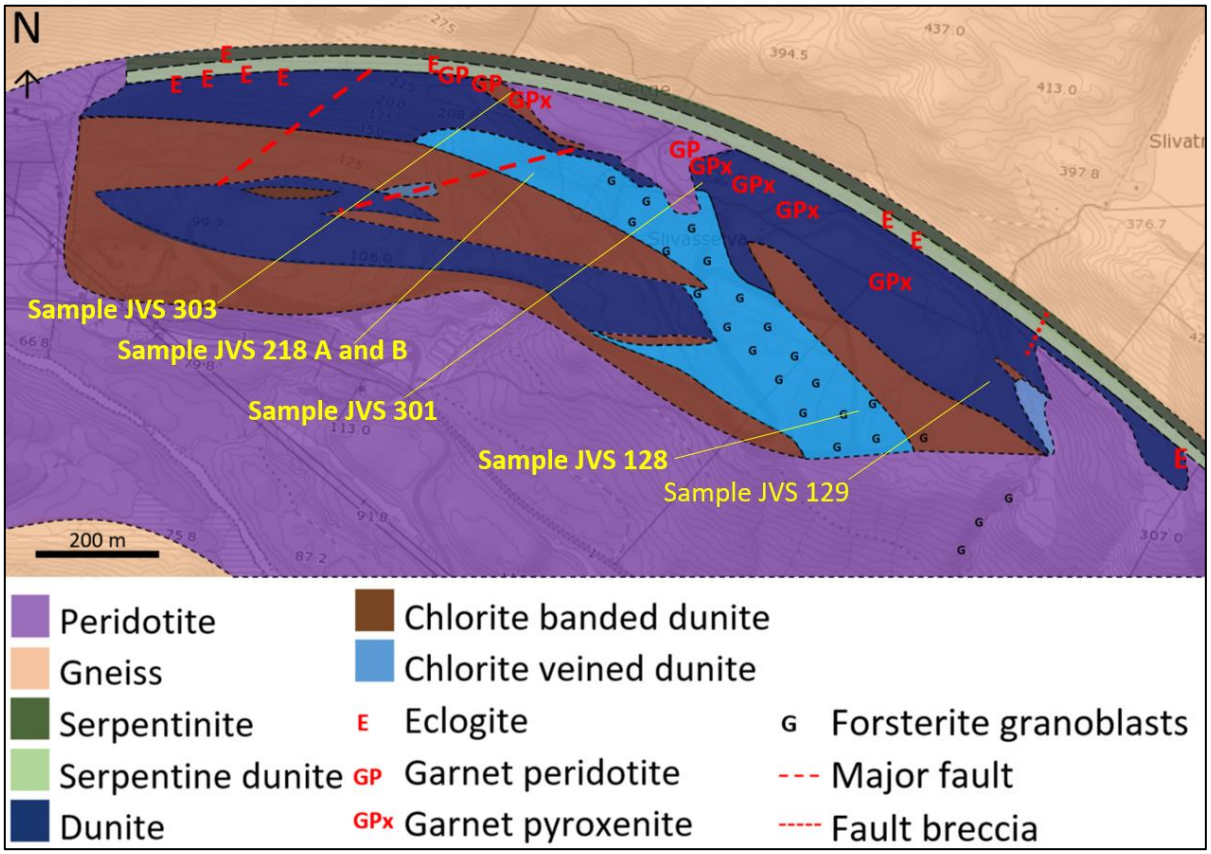

Figure 6.4.3: Geological map of the Gusdal mine with exact sample locations.

Sample classification from X-ray Diffraction Spectrometry (XRF)

Descriptions include XRD results, the geological setting of each samples and the lithological unit represented by each sample represents.

HH1 A

Sample HH1 A represents relatively fresh garnet pyroxenite (GPx) collected at the HH1 locality at the field area near Helghornsvatnet (Figure 6.4.1). It was collected from a macroscopic isoclinally folded garnet pyroxenite layer (category 3 fold) in the fold hinge of a mesoscopic open fold (category 1 fold). Mineral phases detected by XRD are diopside, enstatite, pyrope and fluoro-edenite (Figure 6.4.5). Categorization after the ternary diagram in Figure 6.1.1 defines it as a garnet bearing websterite.

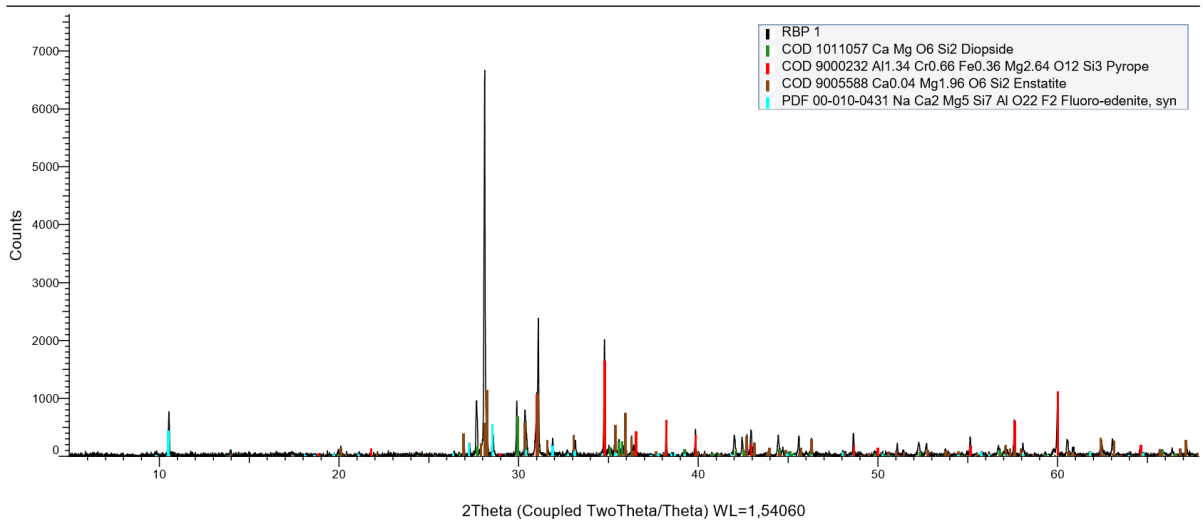

Figure 6.4.5: XRD results for sample HH1 A (RBP 1).

HH1 B

Sample HH1 B represents garnet peridotite (GP) containing minor clinopyroxene and garnet, surrounding the garnet pyroxenite layer represented by sample HH1 A (Figure 6.4.1). It was collected at the HH1 locality and represent an open-folded garnet peridotite layer (category 3 fold) in the hinge of a mesoscopic open fold (category 1 fold). Mineral phases detected by XRD are forsterite, pargasite and lizardite (Figure 6.4.6), although pyrope garnet and diopside are clearly optically visible (Figure 6.4.7). Categorization according to the ternary diagram in Figure 6.1.1 defines it as a garnet bearing lherzolite/wehrlite.

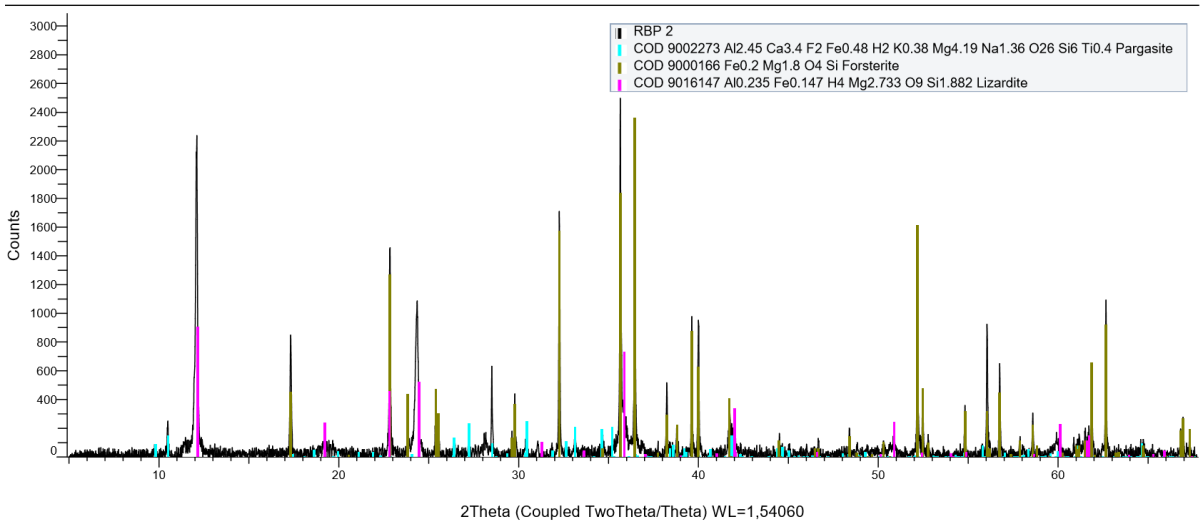

Figure 6.4.6: XRD results for sample HH1 B (RBP 2).

Figure 6.5.7: Garnet Lherzolite/wehrlite from the HH1 locality (Figure 4.5.1).

HH1 C

Sample HH1 C represents altered garnet peridotite (GP) containing clinopyroxene, minor amphibole and garnet, surrounding the garnet pyroxenite layer represented by sample HH1 (Figure 6.4.1). It was collected at the HH1 locality and represent a slightly altered garnet peridotite layer in the hinge of a mesoscopic open fold (category 1 fold). Mineral phases detected by XRD are olivine, kaersutite, fluor-edenite and clinochlore (Figure 6.4.8). Categorization after the ternary diagram in Figure 6.1.1 defines it as an altered garnet bearing olivine websterite.

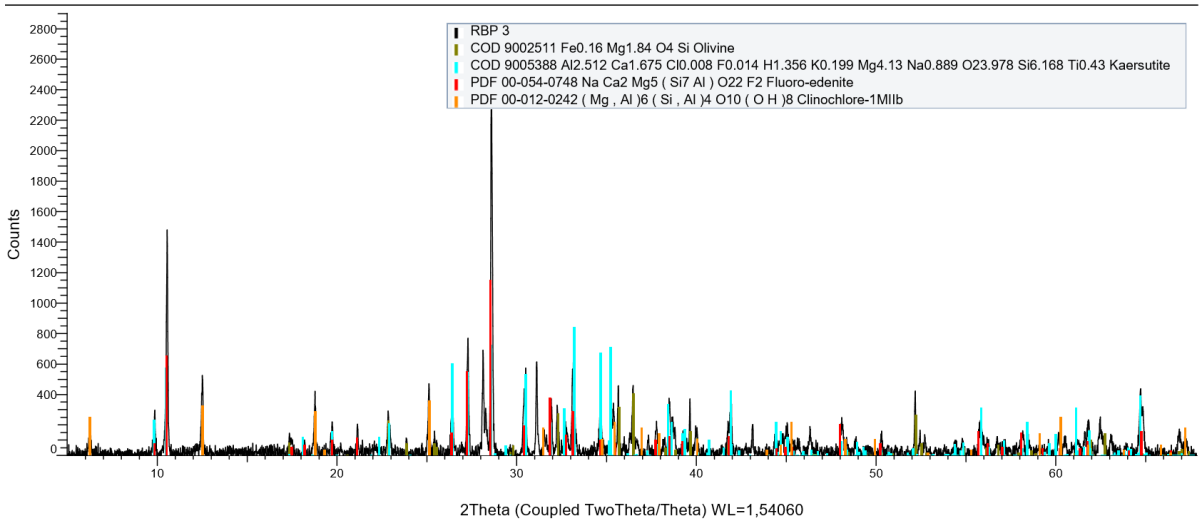

Figure 6.4.8: XRD results for sample HH1 C (RBP 3).

HH1 Garnet and HH1 Clinopyroxene

HH1 Garnet represents pyrope garnets and HH1 Clinopyroxene represents pyroxene separated from the HH1 A sample. These samples were not analyzed by XRD.

JVS 051

Sample JVS 051 represent relatively fresh garnet pyroxenite (GPx) collected at Helghornsvatnet (Figure 6.4.1), from a garnet pyroxenite layer in the hinge of a mesoscopic open fold (category 1 fold). Mineral phases detected by XRD are diopside, pargasite, pyrope and clinochlore (Figure 6.4.9). Categorization after the ternary diagram in Figure 6.1.1 defines it as a garnet bearing websterite.

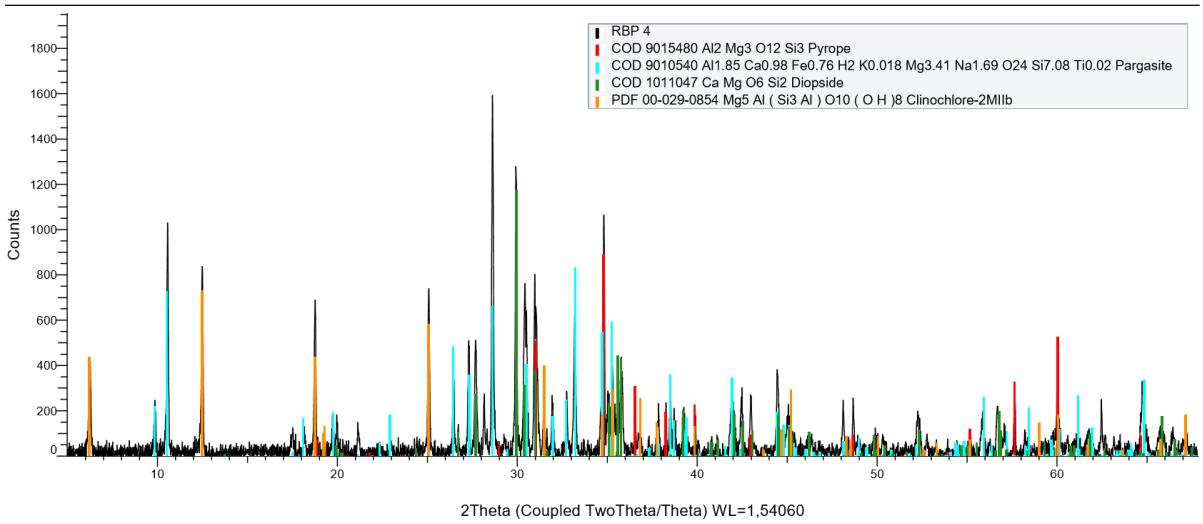

Figure 6.4.9: XRD results for sample JVS 051 (RBP 4).

JVS 156

Sample JVS 156 represent slightly altered garnet peridotite (GP) collected at Helghornsvatnet (Figure 6.4.1). It was collected from the contact between clinochlore layers in garnet lherzolite/wehrlite and garnet pyroxenite. Mineral phases detected by XRD are olivine, pyrope and lizardite (Figure 6.4.10). Categorization after the ternary diagram in Figure 6.1.1 defines it as a garnet lherzolite/wehrlite.

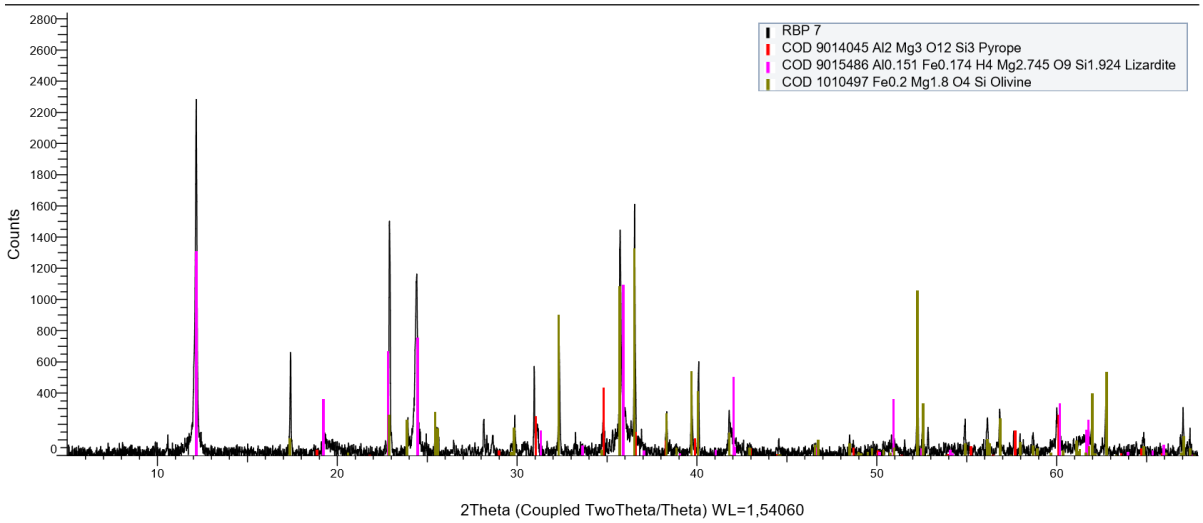

Figure 6.4.10: XRD results for sample JVS 156 (RBP 7).

JVS 166B

Sample JVS 166B represent a highly altered lithology collected at Helghornsvatnet (Figure 6.4.1). It was collected from is a layer in the hinge of a mesoscopic open fold (category 1 fold). This sample is an addition to the JVS 195-8 1 to JVS 195-8 5 series. Mineral phases detected by XRD are hornblende and clinochlore (Figure 6.4.11). The sample is categorized as a retrograded equivalent of garnet pyroxenite (GPx) and the lower left photo in Figure 6.3.20 illustrates the field relation and texture of the clinochlore layer this sample represents.

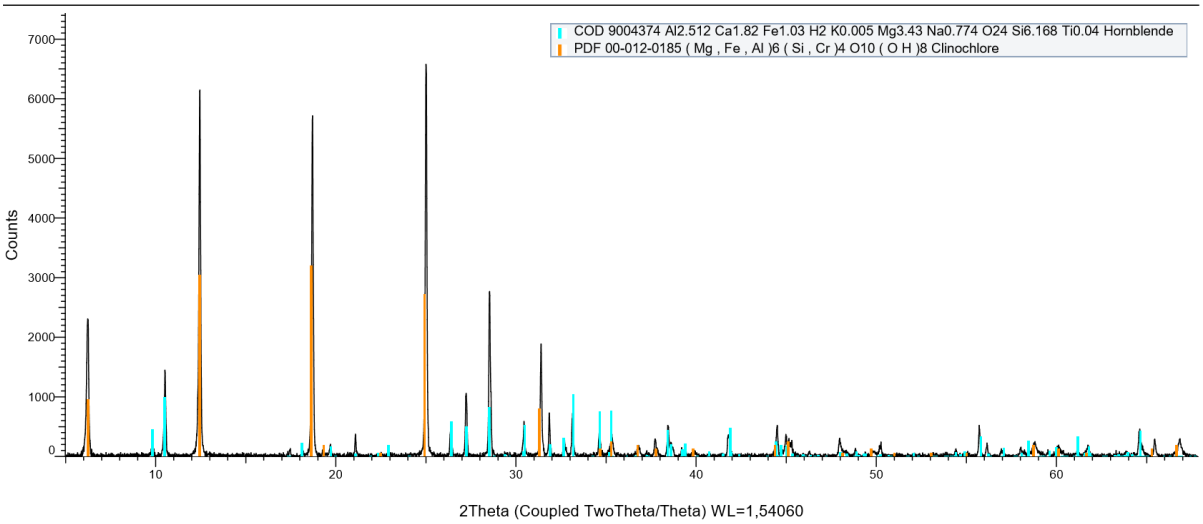

Figure 6.4.11: XRD results for sample JVS 166B (RBP 8).

JVS 195-8 1

Sample JVS 195-8 1 represents altered garnet peridotite (GP) at Helghornsvatnet (Figure 6.4.1 and Figure 6.4.2). It contains visual remains of garnet cores in the clinochlore. It was collected from is a layer in the hinge of a mesoscopic open fold (category 1). Mineral phases detected by XRD are olivine, tremolite and clinochlore (Figure 6.4.12). This samples also contains visible remains of garnets and diopside. Categorization after the ternary diagram in Figure 6.1.1 defines this sample as an altered garnet bearing lherzolite/wehrlite.

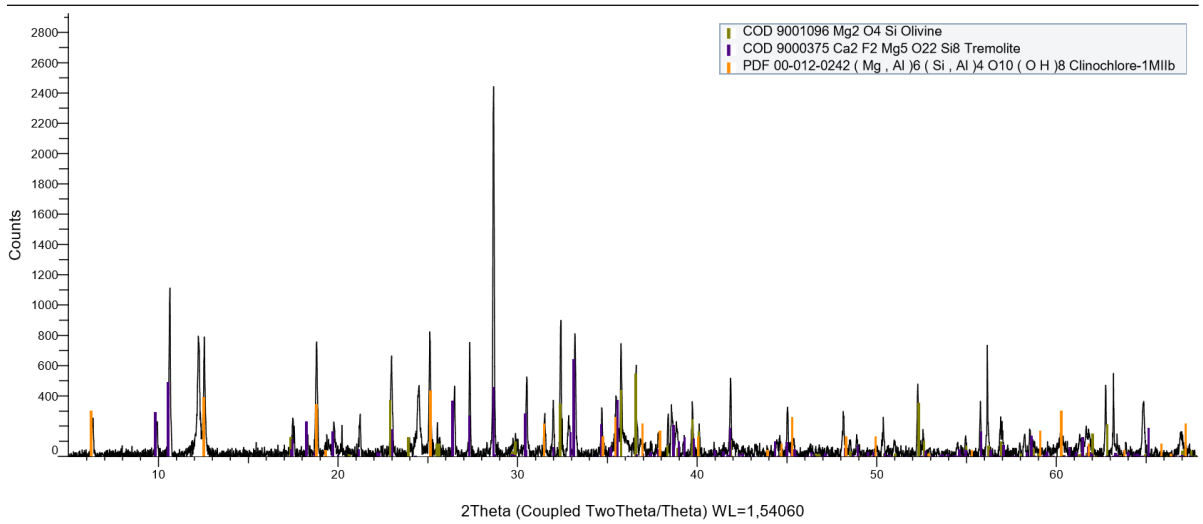

Figure 6.4.12: XRD results for sample JVS 195-8 1 (RBP 11).

JVS 195-8 2

Sample JVS 195-8 2 is an altered garnet pyroxenite (GPx) collected at Helghornsvatnet (Figure 6.4.1 and Figure 6.4.2). It contains visual remains of garnet cores in the clinochlore. It was collected from a layer in the hinge of a mesoscopic open fold (category 1 fold). Mineral phases detected by XRD are olivine, tremolite and clinochlore (Figure 6.4.13). This samples also contains visible remains of garnets and diopside. Categorization after the ternary diagram in Figure 6.1.1 defines this sample as an altered garnet-bearing olivine websterite.

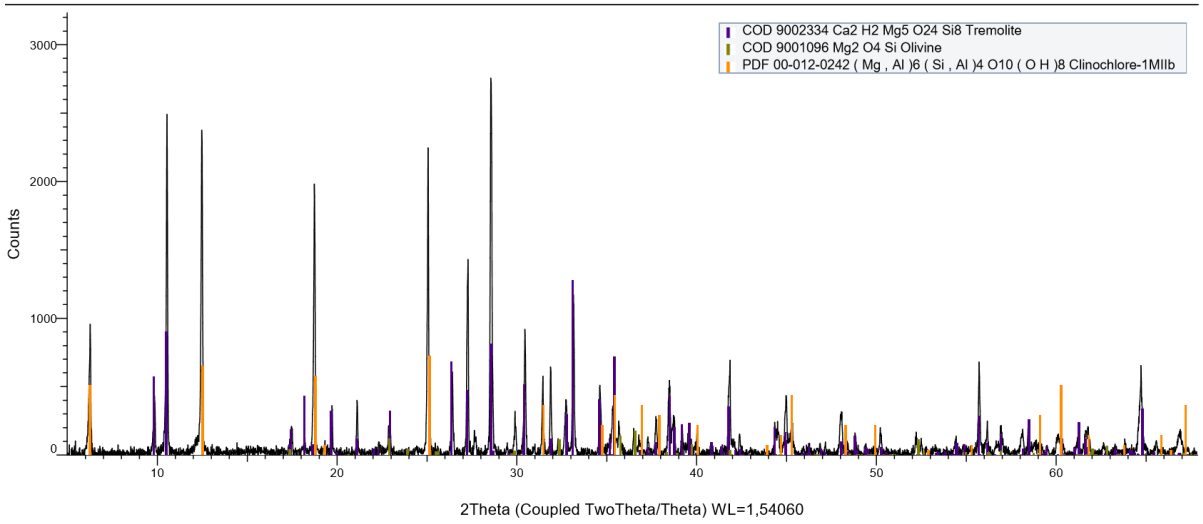

Figure 6.4.13: XRD results for sample JVS 195-8 2 (RBP 12).

JVS 195-8 3

Sample JVS 195-8 3 is altered garnet peridotite (GP) collected at Helghornsvatnet (Figure 6.4.1 and Figure 6.4.2). It contains no visual remains of garnet cores in the clinochlore. It was collected from is altered garnet peridotite layer in the hinge of a mesoscopic open fold (category 1 fold). Mineral phases detected by XRD are olivine, tremolite, lizardite and clinochlore (Figure 6.4.14). Categorization after the ternary diagram in Figure 6.1.1 defines this sample as an altered garnet-bearing lherzolite/wehrlite.

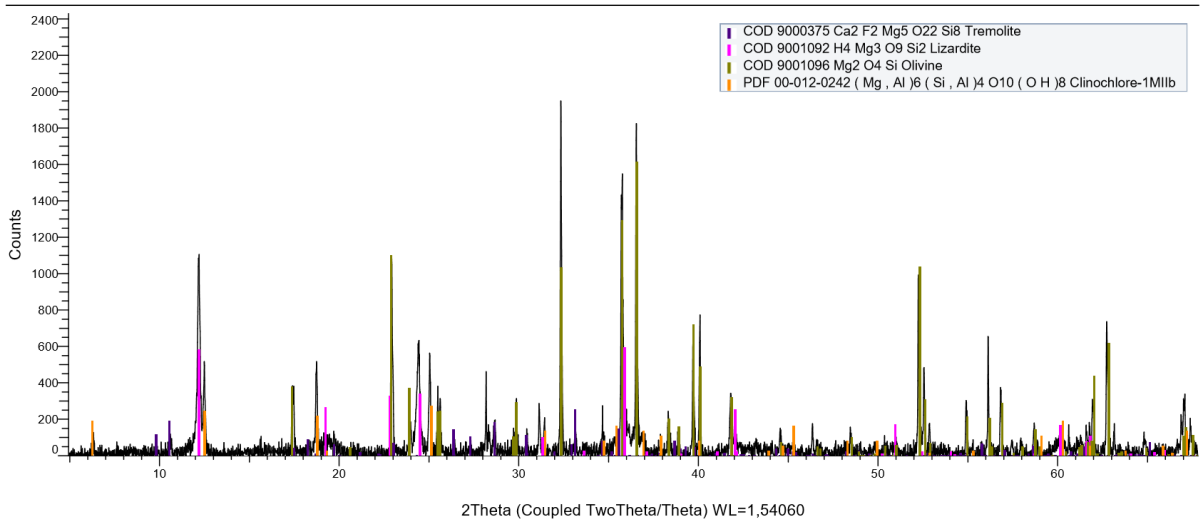

Figure 6.4.14: XRD results for sample JVS 195-8 3 (RBP 13).

JVS 195-8 4

Sample JVS 195-8 4 is an altered garnet peridotite (GP) collected at Helghornsvatnet (Figure 6.4.1 and Figure 6.4.2). It contains no visual remains of garnet cores in the clinochlore. It was collected from a layer in the hinge of a mesoscopic open fold (category 1 fold). Mineral phases detected by interpretation of XRD results are olivine, antigorite and clinochlore (Figure 6.4.15). Categorization after the ternary diagram in Figure 6.1.1 defines this sample as an altered garnet-bearing lherzolite/wehrlite.

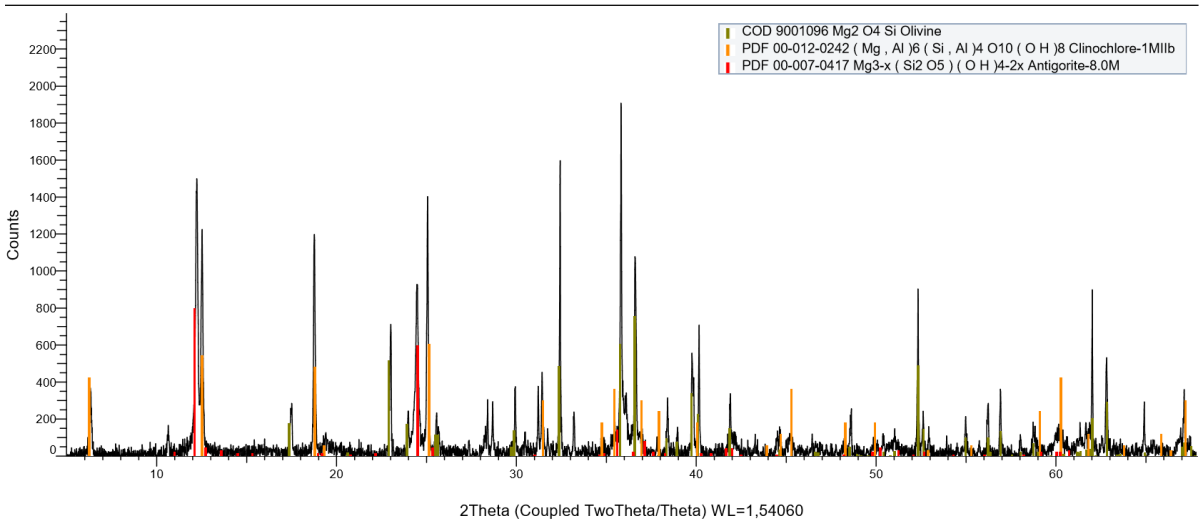

Figure 6.4.15: XRD results for sample JVS 195-8 4 (RBP 14).

JVS 195-8 5

Sample JVS 195-8 5 represents dunite collected at Helghornsvatnet (Figure 6.4.1 and Figure 6.4.2). It was collected from a layer in the hinge of a mesoscopic open fold (category 1 fold). Mineral phases detected by XRD are olivine and clinochrysotile (Figure 6.4.16). Categorization after the ternary diagram in Figure 6.1.1 defines this sample as a slightly altered dunite.

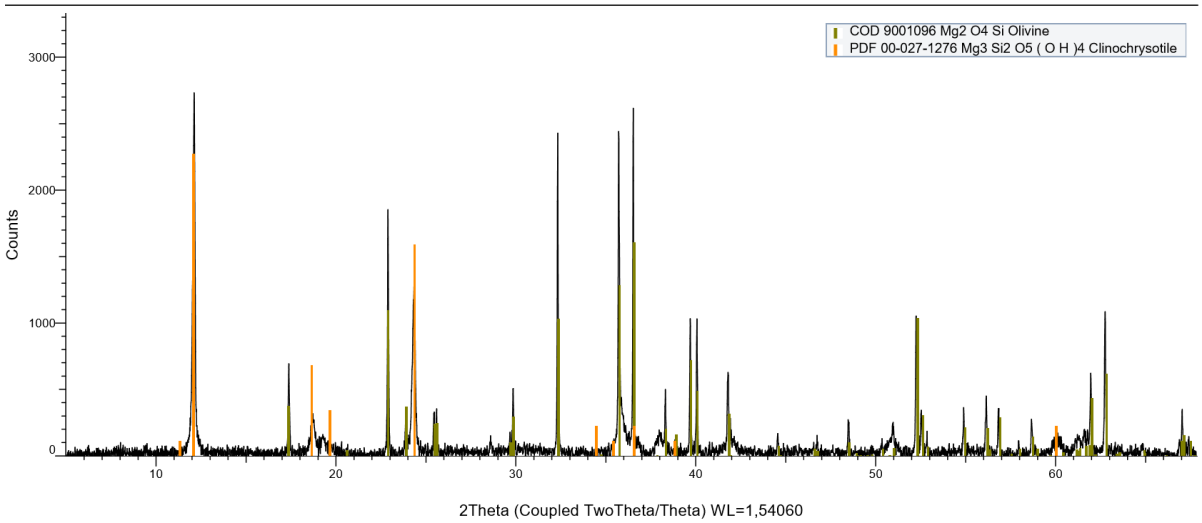

Figure 6.4.16: XRD results for sample JVS 195-8 5 (RBP 15).

JVS 128

Sample JVS 128 was collected at the Gusdal mine (Figure 6.4.3). It is a dunite containing forsterite granoblasts (G). Mineral phases detected by XRD are olivine and clinochlore (Figure 6.4.17). Categorization after the ternary diagram in Figure 6.1.1 defines it as a dunite.

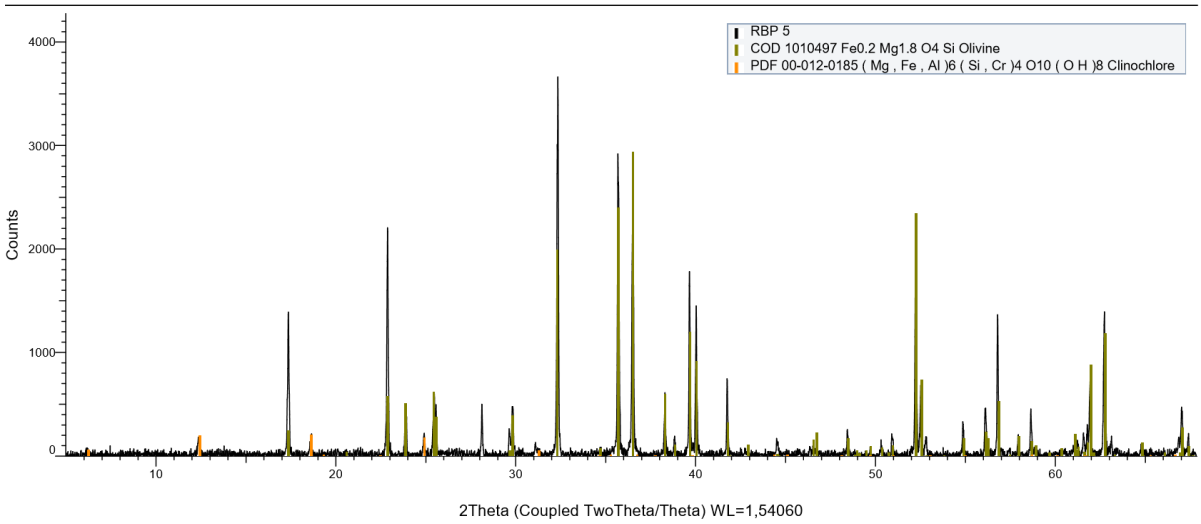

Figure 6.4.17: XRD results for sample JVS 128 (RBP 5).

JVS 129

Sample JVS 129 is dunite collected at the Gusdal mine (Figure 6.4.3). Mineral phases detected by XRD are olivine and clinochlore (Figure 6.4.18). Categorization after the ternary diagram in Figure 6.1.1 defines it as a dunite.

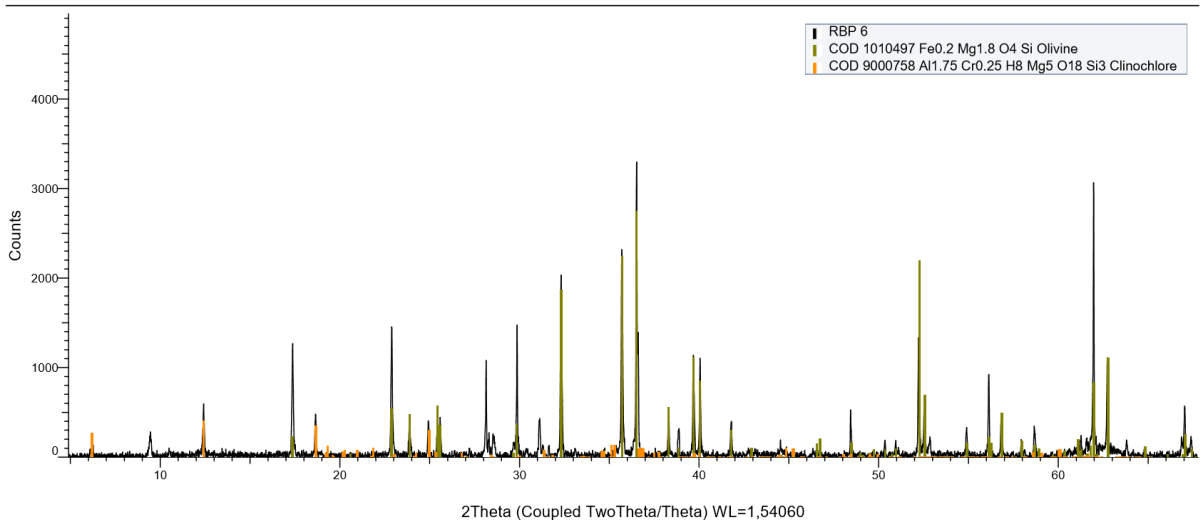

Figure 6.4.18: XRD results for sample JVS 129 (RBP 6).

JVS 218A

Sample JVS 218A Crystal represents subhedral chromite/spinel crystals from a lens at the Gusdal mine containing subhedral chromite/spinel crystals in a clinochlore matrix (Figure 6.4.3). It was collected within the chlorite veined dunite. This type of lithological element (chromitite) has not been found previously in the Almklovdalen peridotite. A photo of the sample is provided in Figure 6.4.21. The only mineral phase detected by XRD is magnesiochromite (Figure 6.4.19). Categorization of this sample will be discussed further in the discussion chapter.

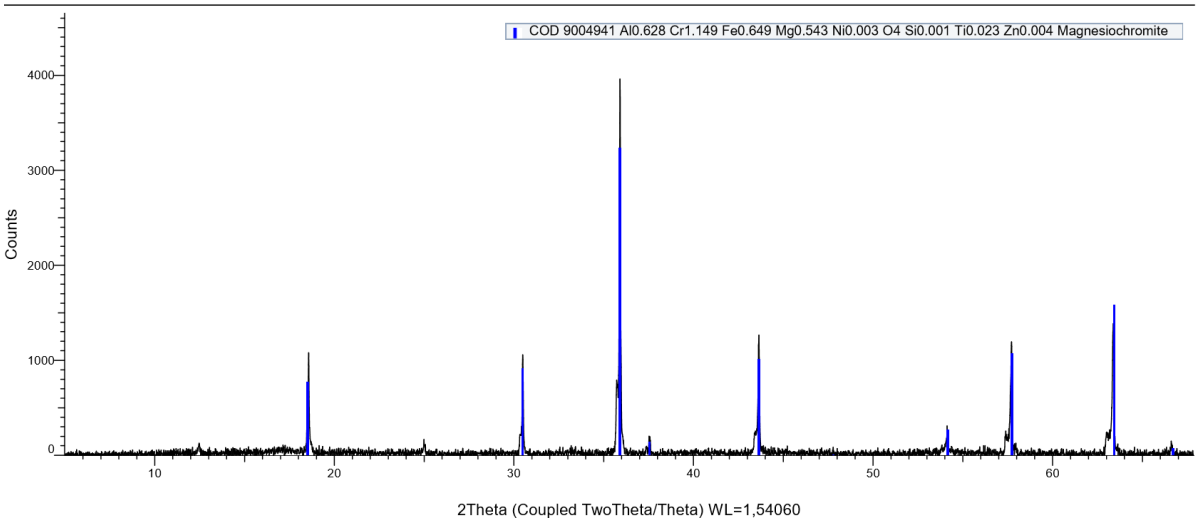

Figure 6.4.19: XRD results for sample JVS 218A Crystal (RBP 9).

JVS 218B

Sample JVS 218B represents bulk subhedral chromite/spinel crystals in a clinochlore matrix from a lens at the Gusdal mine (Figure 6.4.3). It was collected from within the chlorite veined dunite. This type of lithological element has not been found previously in the Almklovdalen peridotite. A photo of the sample is provided in Figure 6.4.21. Mineral phases detected by XRF are magnesiochromite, spinel and clinochlore (Figure 6.4.20). Categorization of this sample will be discussed further in the discussion chapter.

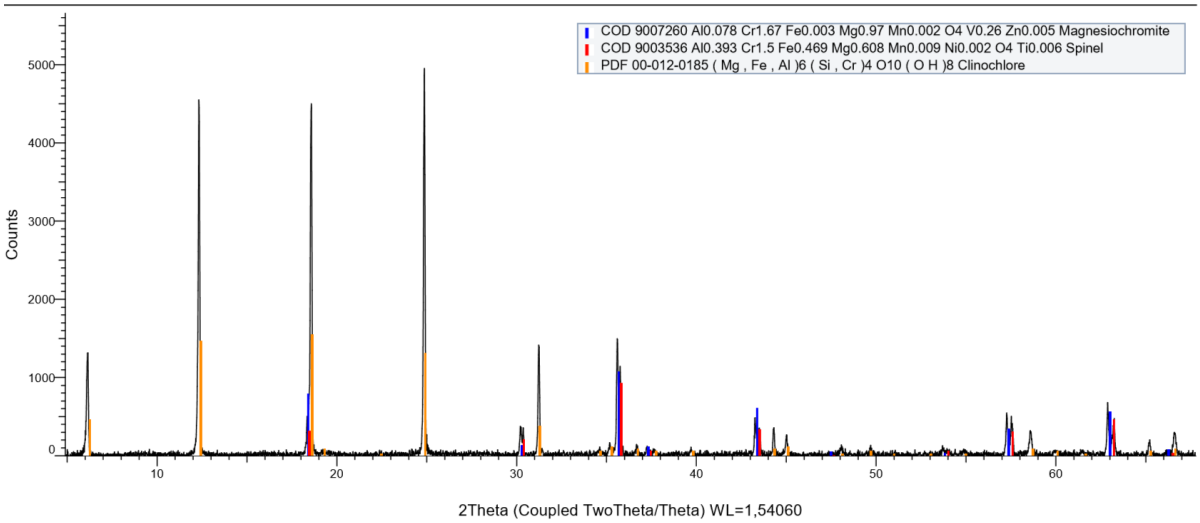

Figure 6.4.20: XRD results for sample JVS 218B Bulk (RBP 10).

Figure 6.4.21: Subhedral magnesiochromite crystal in clinochlore matrix representing sample JVS 218A and JVS 218B.

JVS 301

Sample JVS 301 represents a relatively fresh garnet pyroxenite (GPx) from a garnet peridotite lens in dunite the Gusdal mine (Figure 6.4.3). Mineral phases detected by XRD are olivine, diopside, enstatite and pyrope (Figure 6.4.22). Categorization after the ternary diagram in Figure 6.1.1 defines this sample as a garnet-bearing olivine websterite.

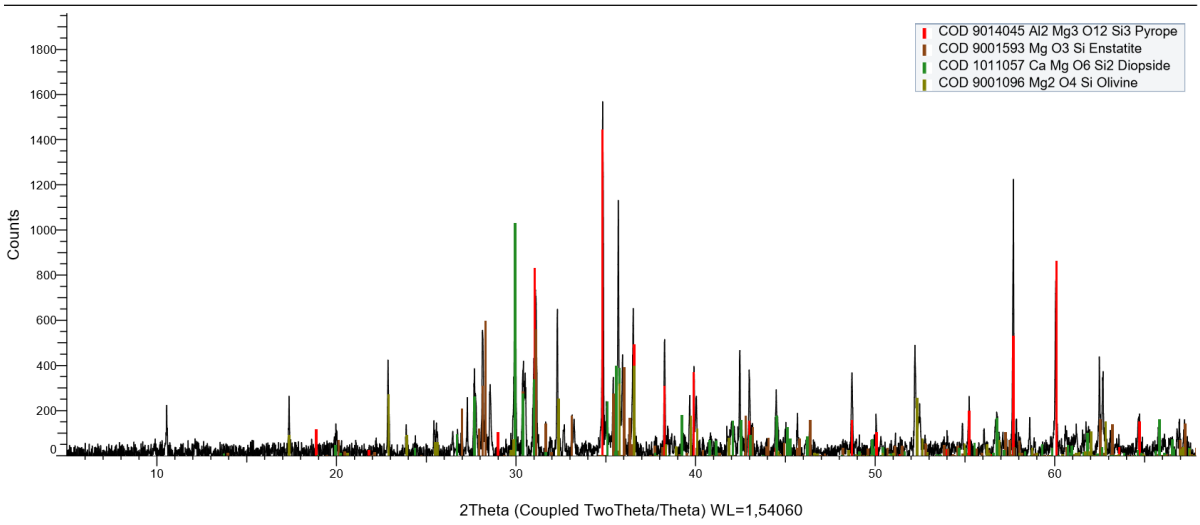

Figure 6.4.22: XRD results for sample JVS 301 (RBP 16).

JVS 303

Sample JVS 303 represents a clinochlore lens in chlorite-banded dunite and was collected at the Gusdal mine (Figure 6.4.3). Mineral phases detected by XRD are hornblende and clinochlore (Figure 6.4.23). Categorization after the ternary diagram in Figure 6.1.1 is difficult due to the high degree of alteration. The lens contains a core of enstatite embedded in amphibole and clinochlore (Figure 6.4.24). This indicates that sample JVS 303 represents an altered harzburgite.

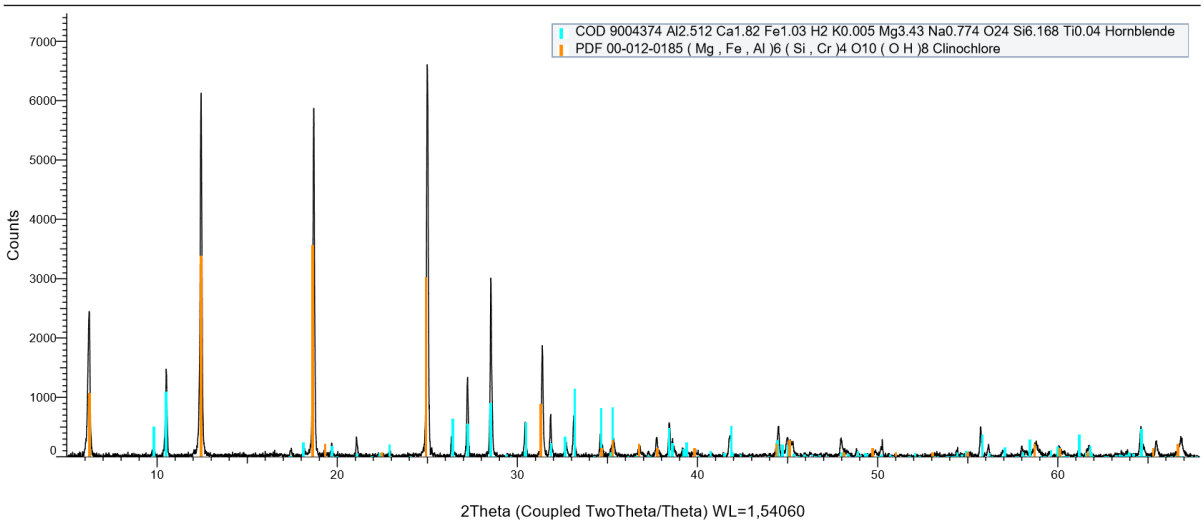

Figure 6.4.23: XRD results for sample JVS 303 (RBP 17).

Figure 6.4.24: Photo of an enstatite core embedded in amphibole and clinochlore represented by sample JVS 303.

6.5 X-ray Fluorescence Spectrometry (XRF) and X-ray Diffraction Spectrometry (XRD) analyses of samples with high chromite content

XRF and XRD analyses of sample JVS 218A and JVS 218B were done to deduce major-element abundance and mineral content in these samples. The analyses were conducted in a laboratory at the SIBELCO Nordic main office in Asker, Norway. Analytical procedures were carried out by the laboratory staff. The results are presented in table 6.5.1. This was done in order to get an indication of what minerals in these samples did not dissolve during the preparation and analytical procedure conducted during analyses done at UiB.

Table 6.5.1: XRF and XRD results from analyses of sample JVS 218A and JVS 218B conducted by the SIBELCO Nordic laboratory at the main office in Norway.

XRF		
Sample ID:	JVS 218A	JVS 218B
	wt%	wt%
SiO2	10,74	25,42
TiO2	0,55	0,16
Al2O3	12,93	14,32
Cr2O3	42,68	15,39
Fe2O3	21,68	7,38
MgO	12,83	28,53
CaO	0,1	0,07
Na2O	0,21	0,4
K2O	0	0
LOI	-0,52	0
Total	101,2	91,67
XRD		
	wt%	wt%
Chromite	92,2	
Magnesiochromite		31,8
Olivine	3,8	
Chlorite		68,2

6.6 Major- and trace elements by ICP-MS and ICP-OES

Major elements and Ni, Co, Cu and Zn were analyzed by ICP-OES (Inductively Coupled Plasma Optical Emission Spectrometry). Trace elements were analyzed by ICP-MS (Inductively Coupled Plasma Mass Spectrometry). Results for both trace elements and major elements will be used for further discussion because they were all analyzed at the UiB laboratory and correspond to each other. The results including Mg# and Cr# for each individual sample are presented in Table 6.6.1. GP is garnet peridotite, GPx is garnet pyroxenite and CPx is clinopyroxenite. Sample HH1 Gnt represents separated garnet from sample HH1A and HH1 CPx represents separated clinopyroxene from sample HH1A.

Table 6.6.1: Major- and trace-element abundances in all samples from the Almklovdalen peridotite. NA indicates not analyzed and ND indicates not detected.

ID:	HH 1 A	HH 1 B	HH 1 C	HH 1 A Grt	HH 1 A CPx	JVS 051	JVS 156	JVS 166 B	JVS 195-8 1	JVS 195-8 2	JVS 195-8 3	JVS 195-8 4	JVS 195-8 5	JVS 128	JVS 129	JVS 218A	JVS 218B	JVS 301	JVS 303
Type:	GPx	GP	GP	Garnet	CPx	GPx	GP	Clinochlore	GP	GPx	GP	Dunite	Dunite	Dunite	Dunite	Chromite	Chromite	GP	Clinochlore
	wt%	wt%	wt%	wt%	wt%	wt%	wt%	wt%	wt%	wt%	wt%	wt%	wt%	wt%	wt%	wt%	wt%	wt%	wt%
SiO2	49,11	40,07	46,12	NA	49,40	45,63	39,01	39,59	43,05	43,33	39,89	39,06	38,17	40,21	41,23	1,07	10,03	45,68	40,65
TiO2	0,13	0,02	0,20	NA	0,16	0,11	0,01	0,10	0,07	0,10	0,03	0,01	0,00	0,00	0,01	0,43	0,28	0,42	0,05
Al2O3	8,02	0,79	6,02	NA	4,51	9,35	1,97	11,53	2,88	7,37	0,96	1,67	0,15	0,28	0,40	9,53	8,70	7,70	4,99
Cr2O3	0,14	0,37	0,20	NA	0,11	0,10	0,33	0,16	0,29	0,21	0,35	0,33	0,40	0,39	0,38	NA		0,17	0,20
FeO	9,37	8,09	8,75	NA	2,39	5,10	6,51	3,33	6,56	4,55	7,02	5,94	6,45	5,96	6,16	13,88	11,32	7,96	5,03
MnO	0,16	0,09	0,16	NA	0,05	0,18	0,10	0,05	0,15	0,14	0,11	0,10	0,09	0,09	0,09	0,27	0,22	0,17	0,10
MgO	23,69	45,13	28,95	NA	18,88	19,55	40,31	28,29	34,76	25,44	43,06	43,50	46,33	50,21	47,63	10,84	17,22	26,04	30,66
CaO	7,01	1,02	5,39	NA	17,22	11,77	1,26	5,94	4,66	8,58	0,59	0,39	0,03	0,01	0,13	ND	ND	7,63	3,08
Na2O	0,50	0,21	0,80	NA	1,20	0,84	0,16	0,87	0,34	0,85	0,11	0,11	0,08	0,09	0,11	0,10	0,10	0,62	0,58
K2O	0,01	0,02	0,05	NA	0,06	0,03	0,01	0,12	0,03	0,07	0,01	0,02	0,02	0,02	0,03	0,02	0,01	0,03	0,90
P2O5	0,01	0,00	0,01	NA	0,01	0,01	0,00	0,01	0,01	0,01	0,01	0,00	0,01	ND	ND	ND	ND	0,01	0,00
NiO	0,12	0,32	0,18	NA	0,10	0,09	0,29	0,14	0,25	0,19	0,30	0,29	0,35	0,34	0,33	NA	NA	0,15	0,18
LOI	0,03	3,20	1,30	NA	1,25	1,60	6,10	7,20	6,20	4,50	5,60	6,60	10,20	0,20	0,50	0,40	3,10	0,40	10,40
Total	98,30	99,33	98,14	NA	95,32	94,36	96,06	97,32	99,25	95,33	98,03	98,01	102,28	97,81	97,01	36,53	50,97	96,98	96,81
Mg#	81,84	90,86	85,50	NA	93,36	87,24	91,70	93,81	90,43	90,88	91,62	92,89	92,76	93,75	93,24	58,20	73,05	85,36	91,57
Cr#	1,14	23,93	2,23	NA	1,63	0,71	10,06	0,92	6,39	1,91	19,60	11,82	64,53	48,40	38,42	NA	NA	1,50	2,63
	ppm	ppm	ppm	ppm	ppm	ppm	ppm	ppm	ppm	ppm	ppm	ppm	ppm	ppm	ppm	ppm	ppm	ppm	
Co	80,89	125,84	99,55	NA	33,24	43,28	109,82	45,55	107,53	75,25	117,96	106,17	129,36	107,40	108,49	NA	NA	83,80	77,97
Cu	63,69	12,92	21,66	NA	42,99	54,69	11,66	10,77	136,00	128,15	12,01	17,65	7,90	5,70	9,88	NA	NA	49,61	37,67
Cr	2181,60	1513,54	4080,74	NA	7028,36	6023,39	2833,96	11151,18	5192,99	5453,71	1984,85	4606,43	581,29	1225,10	2307,06	NA	NA	1995,56	3422,86
Ni	946,04	2614,57	1419,96	NA	772,09	689,66	2401,64	1177,64	2135,95	1536,65	2529,01	2452,31	3072,57	2670,86	2583,64	NA	NA	1201,78	1540,75
Pb	132,10	117,31	133,46	NA	141,63	123,07	115,67	117,17	129,02	121,99	122,68	117,70	124,76	112,94	114,44	NA	NA	123,64	127,76
V	156,21	28,86	161,57	NA	244,63	174,87	36,29	210,96	100,08	205,14	30,54	32,87	4,92	7,74	18,33	NA	NA	205,64	114,84
Zn	67,37	72,87	61,29	NA	17,51	18,86	48,97	22,76	43,09	24,64	50,05	49,28	45,62	39,22	43,75	NA	NA	42,04	35,53
Rb	0,12	0,07	0,56	<0.013	0,34	0,50	0,09	0,88	0,13	0,49	0,03	0,10	0,04	<0.013	0,17	0,10	0,06	0,21	15,25
Ba	33,79	8,20	74,78	13,87	18,19	37,95	7,26	34,75	48,98	33,72	6,78	5,04	6,45	0,69	5,81	12,24	7,45	35,69	740,50
Th	0,07	0,01	0,29	0,01	0,06	0,04	0,01	0,01	0,03	0,03	0,01	0,01	0,00	0,00	0,01	0,08	0,07	0,08	0,55
U	0,02	0,01	0,05	0,01	0,01	0,01	0,01	0,01	0,01	0,01	0,00	0,02	0,02	0,00	<0.0013	0,88	1,59	0,03	0,28
Nb	0,18	0,22	3,46	0,10	0,42	0,45	0,24	1,60	0,24	0,29	0,29	0,28	0,22	0,08	0,12	5,63	8,77	25,03	1,59
Sc	27,10	5,40	34,83	12,20	26,32	51,40	9,95	71,68	14,14	34,86	5,96	14,43	2,09	4,76	4,76	1,16	4,24	33,22	31,64
La	0,99	0,27	4,55	0,17	2,28	1,30	0,12	1,30	0,35	0,80	0,09	0,09	0,03	0,03	0,15	2,58	2,49	7,43	3,26
Ce	1,22	0,30	7,59	0,21	6,03	3,88	0,25	4,31	1,19	3,07	0,26	0,17	0,04	0,03	0,20	0,92	1,05	16,37	3,70
Pr	0,27	0,06	2,11	0,05	3,01	2,14	0,12	1,92	0,55	1,43	0,11	0,06	0,01	<0.005	0,04	0,06	0,07	4,61	0,87
Tb	0,08	<0.001	0,20	0,21	0,20	0,29	0,02	0,25	0,03	0,08	0,01	0,01	<0.001	<0.001	<0.001	<0.001	0,00	0,32	0,09
Sr	33,18	10,31	168,60	4,97	326,70	223,30	21,51	171,60	93,39	176,60	17,07	10,79	9,59	0,97	26,25	6,82	7,87	375,90	456,10
Nd	1,12	0,23	9,19	0,35	19,91	14,46	0,99	10,49	2,72	7,19	0,56	0,35	0,06	<0.005	0,16	0,09	0,11	18,87	3,77
Zr	2,33	0,46	4,67	4,35	9,35	7,27	0,86	8,65	1,30	3,28	0,21	0,26	0,06	0,06	0,26	2,53	4,01	12,01	5,43
Hf	0,12	0,02	0,16	0,11	0,37	0,22	0,02	0,24	0,05	0,12	0,01	0,01	0,00	0,00	0,01	0,06	0,10	0,36	0,14
Sm	0,29	0,05	1,66	0,28	3,95	3,13	0,32	2,15	0,42	1,11	0,10	0,12	0,01	<0.005	0,02	0,01	0,01	3,02	0,78
Eu	0,13	0,02	0,49	0,18	0,91	0,81	0,08	0,66	0,12	0,29	0,03	0,04	<0.005	<0.005	0,01	0,01	0,01	0,85	0,26
Ti	772,80	131,00	1231,00	575,30	1049,00	725,40	73,60	648,20	383,80	646,00	190,20	33,45	21,70	3,48	66,49	1757,00	841,50	2583,00	343,00
Gd	0,43	0,06	1,37	0,86	2,10	2,17	0,19	1,82	0,27	0,67	0,09	0,12	0,02	<0.005	0,02	0,01	0,02	2,20	0,66
Dy	0,55	0,05	1,11	1,80	0,70	1,59	0,18	1,53	0,17	0,52	0,09	0,07	0,01	<0.001	0,01	0,03	0,04	1,90	0,53
Ho	0,12	0,01	0,21	0,45	0,10	0,32	0,05	0,35	0,04	0,12	0,02	0,01	0,00	<0.001	0,00	0,01	0,01	0,39	0,11
Er	0,37	0,03	0,59	1,46	0,30	0,92	0,18	1,14	0,12	0,41	0,08	0,05	0,01	<0.001	0,01	0,03	0,04	1,20	0,35
Y	3,10	0,27	5,06	8,67	2,10	8,05	1,22	8,71	0,85	2,90	0,57	0,33	0,04	<0.025	0,05	0,18	0,24	9,37	2,75
Yb	0,38	0,03	0,51	1,57	0,13	0,79	0,22	1,17	0,09	0,40	0,07	0,08	0,01	<0.001	0,00	0,05	0,08	1,07	0,39
Lu	0,06	0,00	0,08	0,25	0,02	0,12	0,04	0,19	0,01	0,06	0,01	0,01	<0.001	<0.001	0,01	0,01	0,02	0,16	0,07

6.7 Whole-rock REE and trace-element patterns

REE and trace element patterns representing various combinations of samples are presented in Figure 6.7.1 to Figure 6.7.6. Values used in the diagrams are primitive mantle (PM) normalized and the PM values are listed in Table 6.7.1. These PM values are also used in the diagrams provided in Figure 6.7.8, Figure 6.7.9 and Figure 6.7.10.

Table 6.7.1: Primitive mantle values used for normalizing the REE and trace-elements in addition to the PM values in the individual diagrams.

Element:	Ref.:	PM values:	Element:	Ref.:	PM values:
Rb	2	0,605	Dy	1	0,711
Ba	1	6,75	Ho	1	0,159
Th	1	0,0834	Er	1	0,465
U	1	0,0218	Y	1	4,37
Nb	1	0,588	Yb	1	0,462
La	1	0,686	Lu	1	0,0711
Ce	1	1,786	Pr	1	0,27
Sr	1	20,3	Tb	1	0,105
Nd	1	1,327	Tm	1	0,0717
Zr	1	10,81	Sc	1	16,5
Hf	1	0,3	V	1	86
Sm	1	0,431	Co	1	102
Eu	1	0,162	Ni	1	1860
Ti	1	1280	Cr	1	2520
Gd	1	0,571	Mg#	3	89,3

References	
1	(Palme and O'Neill, 2003)
2	(Hofmann and White, 1983)
3	(McDonough and Sun, 1995)

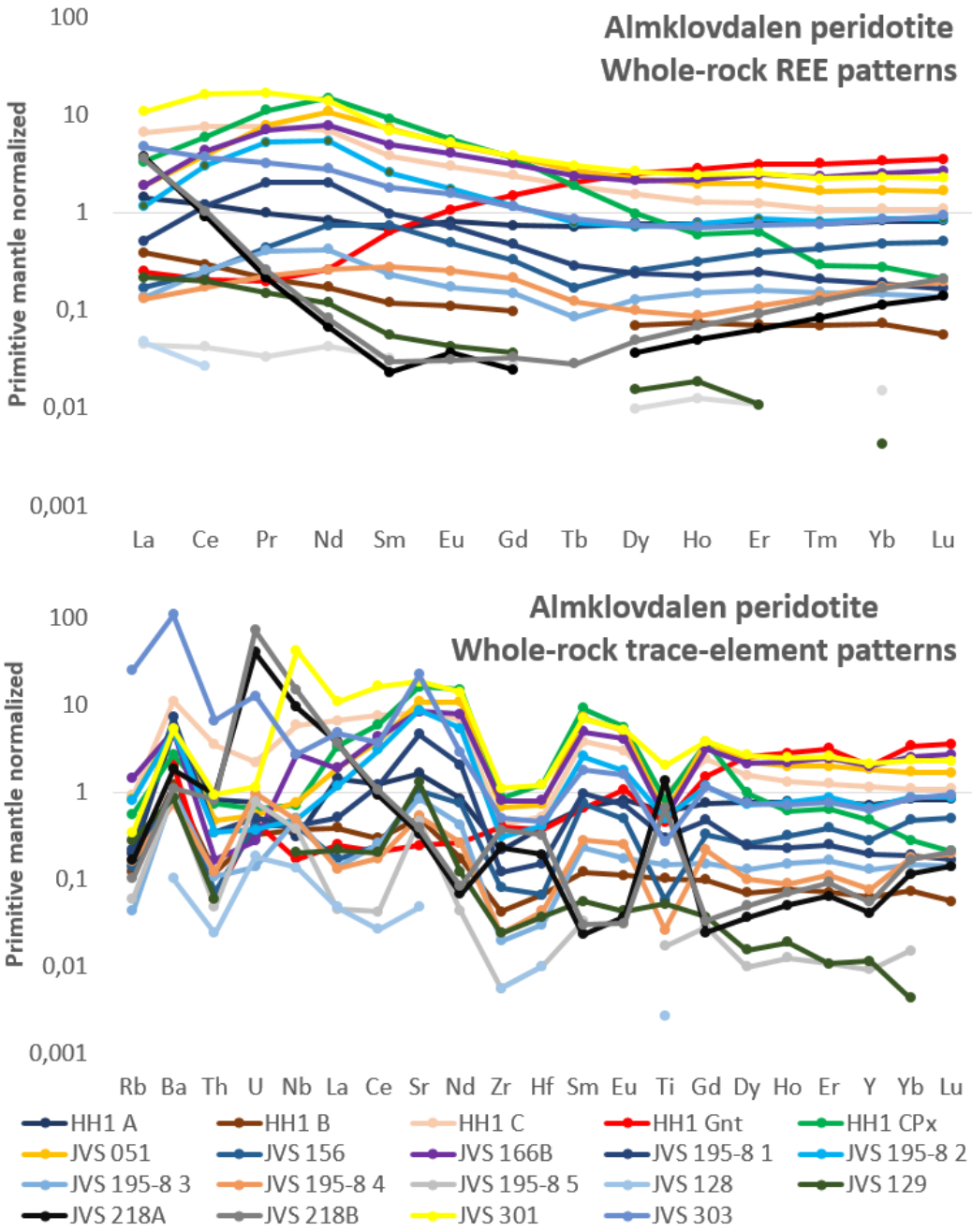

Figure 6.7.1: Whole-rock REE and trace element patterns for all samples from the Almklovdalen peridotite.

Complete sample series

Analytical results represent bulk-rock concentrations and this has to be taken into account when interpreting the distribution of elements. Diagrams in Figure 6.7.1 show enrichment or depletion in bulk-rock REE and trace-elements compared to PM for all samples. The most depleted samples have concentrations near or below the detection limit. The most enriched samples show 10 times PM in some REE and up to approximately 100 times in some trace-elements. A wide distribution of the enrichment factors is apparent in both REE and trace element patterns. Four samples display REE and trace element patterns that apparently deviate from other samples. These sample are HH1 Gnt, HH1 CPx, JVS 218A and JVS 218B and these are presented in individual diagrams. Sample HH1 Gnt and HH1 CPx are presented in Figure 6.7.5 and sample JVS 218A and JVS 218B are presented in Figure

6.7.6. Diagrams illustrating the relation between olivine-rich and garnet-bearing assemblages are provided in Figure 6.7.2 and Figure 6.7.3. Samples JVS 166B and JVS 195-8 1 to 5 represent layering/banding of clinochlore, GP and GPx in dunite. To evaluate the relationship between these layers a diagram is provided in Figure 6.7.4. Further description will be provided below each diagram. The REE will be defined in three groups in order to generally compare the relative enrichment/depletion within individual patterns. These are the LREE (Light Rare Earth Elements) including La, Ce, Pr, Nd and Sm, MREE (Middle Rare Earth Elements) including Eu, Gd, Tb and Dy and HREE (Heavy Rare Earth Elements) including Ho, Er, Tm, Yb and Lu.

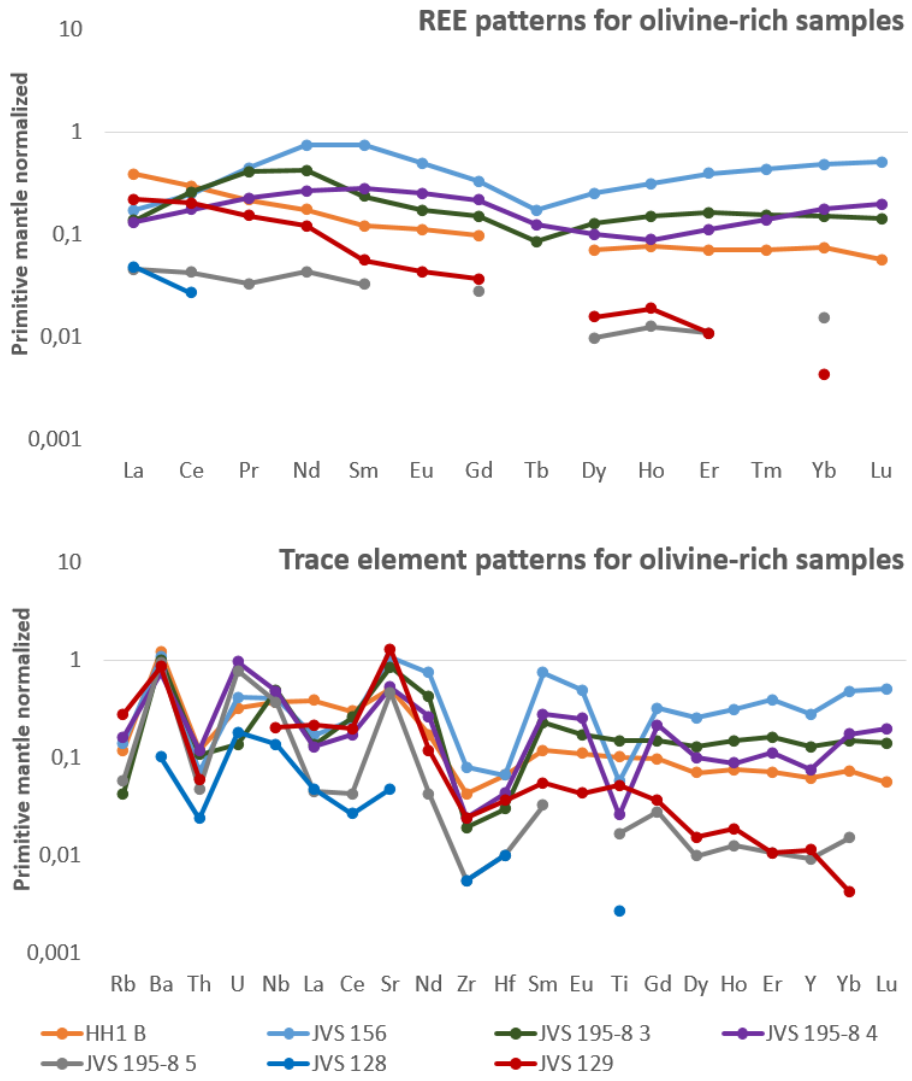

Figure 6.7.2: Whole-rock REE and trace element patterns for olivine-rich samples from the Almklovdalen peridotite.

Olivine-rich samples

The olivine-rich samples are volumetrically dominated by dunites but may also have low contents of garnet, clinopyroxene, amphibole and clinochlore. These samples are HH1 B, JVS 156, JVS 195-8 3, JVS 195-8 4, JVS 195-8 5, JVS 128 and JVS 129. REE and trace-element patterns for all olivine-rich samples are presented in Figure 6.7.2. In both REE and trace-element patterns samples JVS 156, JVS 195-8 3 and JVS 195-8 4 show similarities to the garnet-bearing assemblages in Figure 6.7.3 while

sample HH1 B is more similar to the relatively pure dunite samples. All samples are depleted in REE compared to PM. Low-garnet dunite samples are enriched in Sm, Nd and Eu in addition to HREE compared to garnet-bearing samples. Particularly samples JVS 128, JVS 129 and JVS 195-8 5, which are relatively pure dunites, show a strong depletion in HREE. Trace element patterns show generally low concentrations of Rb, Th, Zr and Hf and high concentrations of Ba and Sr in all samples. JVS 156 and JVS 195-8 4 differ from the other samples in having low concentrations of Ti. Samples JVS 128, JVS 129 and JVS 195-8 5 are the most depleted samples.

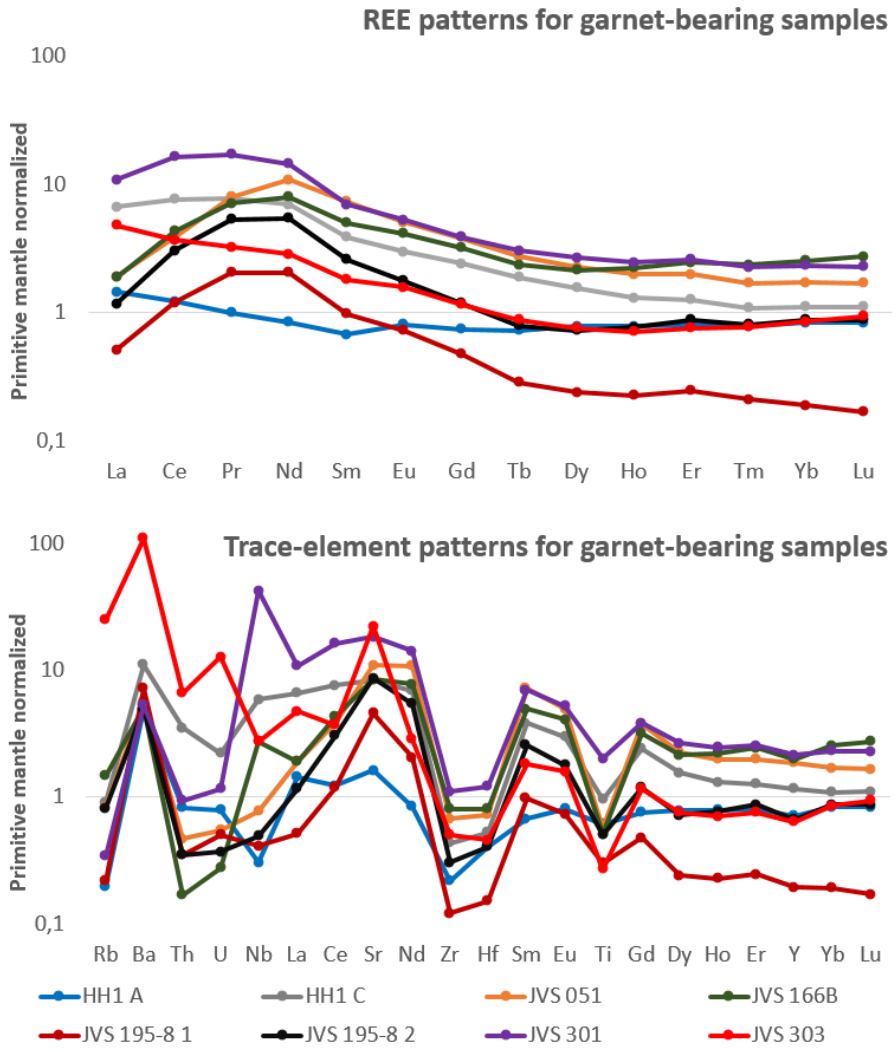

Figure 6.7.3: Whole-rock REE and trace-element patterns for garnet-bearing samples from the Almklovdalen peridotite.

Garnet-bearing assemblages

The garnet-bearing samples include garnet peridotites, garnet pyroxenites and their retrograded equivalents. These are HH1 A, HH1 C, JVS 051, JVS 166 B, JVS 195-8 1, JVS 195-8 2, JVS 301 and JVS 303. Whole-rock REE and trace-element patterns for all garnet-bearing assemblages are presented in Figure 6.7.3. These samples are uniformly high in LREE compared to HREE and PM. A minor trend of low HREE compared to the MREE is apparent. HH1 A and JVS 303 deviate by not being enriched in Ce, Pr and Nd compared to the other the samples. Sample HH1 A show a REE pattern almost parallel to PM. Trace-element patterns show a relative enrichment in Ba, Sr, Nd, Sm, Eu and to minor degree Gd compared to other elements. Relative depletion of Rb, Zr, Hf and Ti is also apparent. The HH1 A

sample shows only a slight depletion in Rb, Nb, Zr and Hf but enrichment in Ba compared to PM. The patterns of JVS 301 show a strong enrichment of Nb and the pattern of JVS 303 shows strong enrichment of Rb, Ba, Th and U compared to other samples and PM. From La to Lu the patterns show strong similarity to each other. The trace element patterns of garnet-bearing assemblages in general cluster from slightly above to slightly under PM.

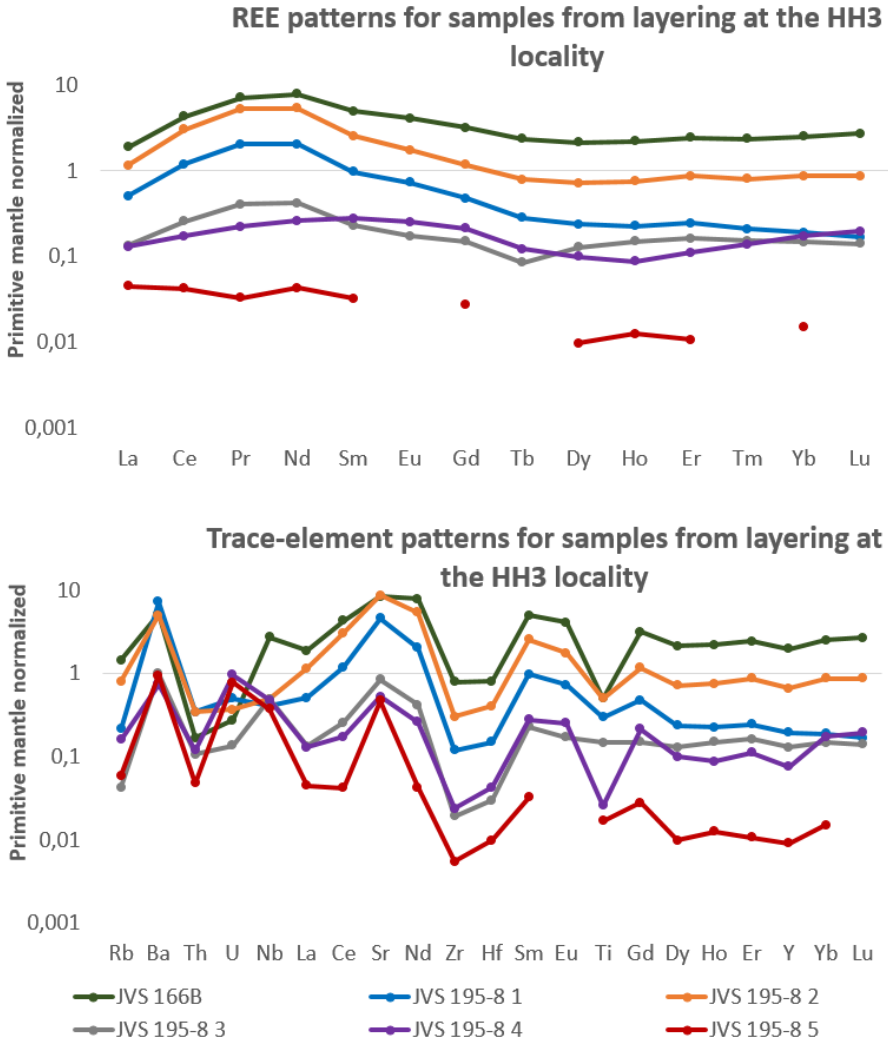

Figure 6.7.4: Whole-rock REE and trace element patterns for samples from layering at location HH3 near Helghornsvatnet.

Samples representing the HH3 locality:

JVS 166B **:** Retrograded equivalent of garnet pyroxenite (GPx)
JVS 195-8 1: Altered garnet-bearing lherzolite/wehrlite (GP)
JVS 195-8 2: Altered garnet websterite (GPx)
JVS 195-8 3: Altered garnet-bearing lherzolite/wehrlite (GP)
JVS 195-8 4: Altered garnet-bearing lherzolite/wehrlite (GP)
JVS 195-8 5: Dunite

For making interpretation easier the samples are labeled above. A gradual transition between the lithologies from which the samples derive from was observed in the field and a detailed map of the

sample locations at the HH3 locality is provided in Figure 6.7.5. REE and trace-element patterns for all samples at the HH3 locality are presented in Figure 6.7.4. REE patterns show a gradual enrichment from the depleted olivine-rich samples (JVS 195-8 3, JVS 195-8 4, JVS 195-8 5) to the garnet- and clinochlore-rich samples (JVS 166B, JVS 195-8 1, JVS 195-8 2). Compared to PM the clinochlore-rich sample JVS 166B and the garnet-bearing sample JVS 195-2 show a moderate enrichment in LREEs except La. JVS 195-8 1 display the same pattern but have approximately equal LREE content to PM and show a minor to moderate depletion in MREE and HREE. Olivine-rich samples are depleted relative to both garnet-bearing assemblages and PM.

Trace element patterns show a similar trend for all samples with a few exceptions. Rb and Th concentrations are low compared to Ba in addition to low Zr and Hf concentrations compared to Sr, Nd, Sm and Eu. Sample JVS 166B and JVS 195-8 4 are moderately depleted in Ti compared to the general trend and JVS 166B has a slightly increased content of Nd compared to all other samples which has approximately equal content of Nd.

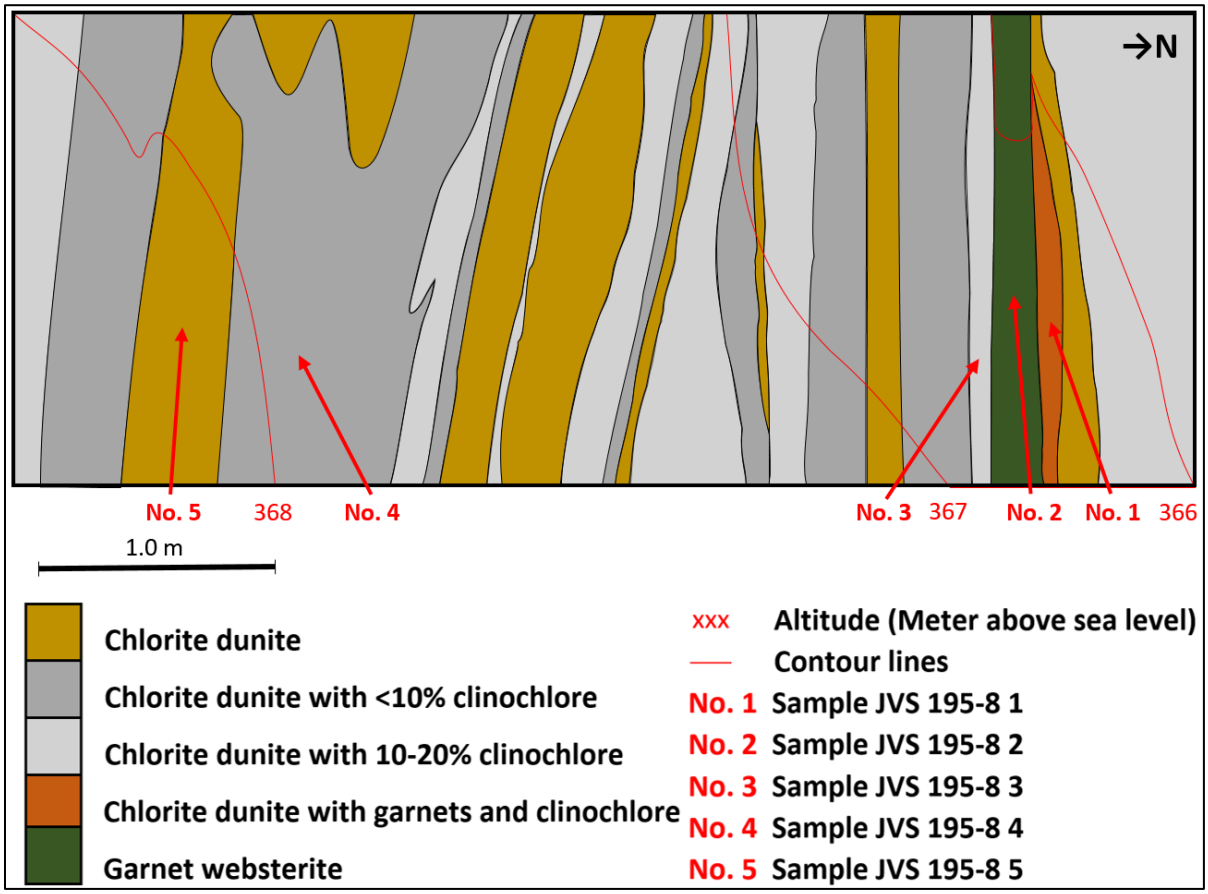

Figure 6.7.5: Detailed geological map showing sample locations for sample JVS 195-8 1 to JVS 195-8 5 from the HH3 locality near Helghornsvatnet (Figure 6.4.1).

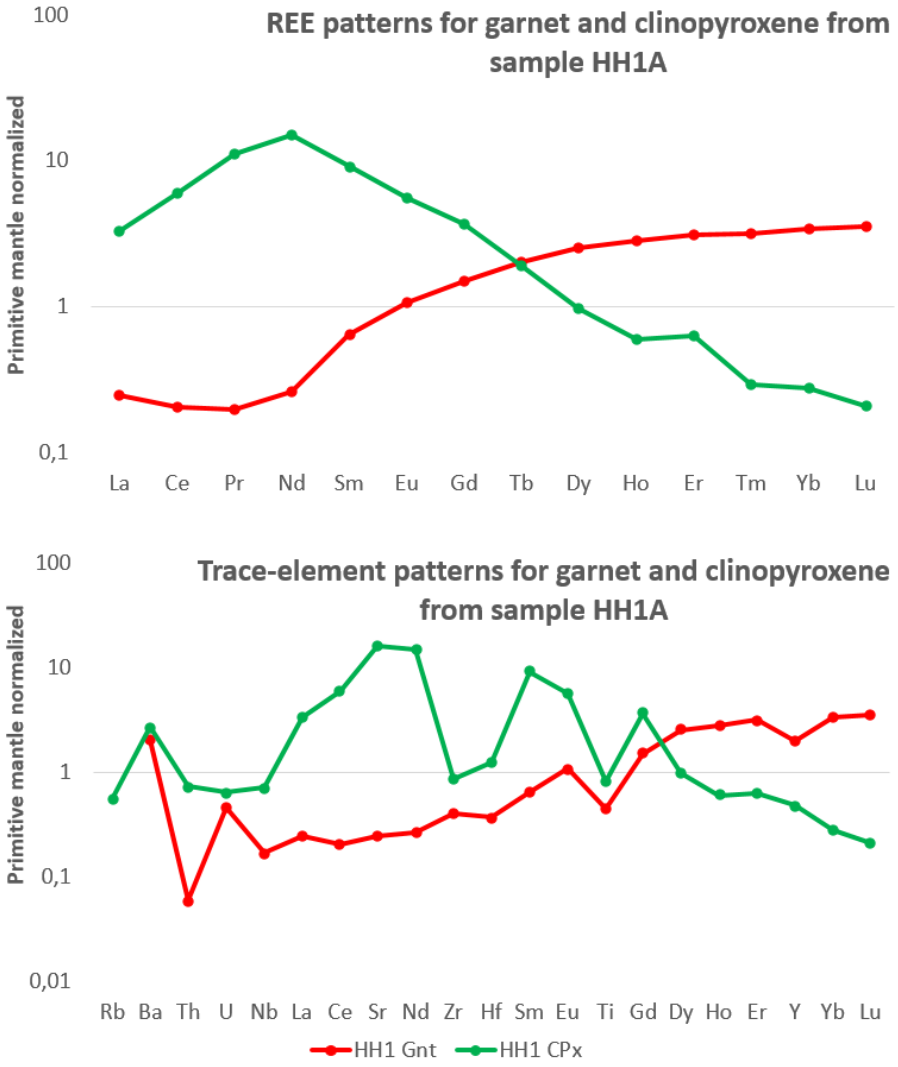

Figure 6.7.6: REE and trace-element patterns for separated garnet and clinopyroxene from sample HH1A collected at the HH1 locality near Helghornsvatnet.

Garnet and clinopyroxenite

Sample HH1 Gnt and HH1 CPx represent separated garnet and clinopyroxene respectively and their REE and trace-element patterns are provided in Figure 6.7.6. Separation was done from sample HH1A, representing a garnet pyroxenite (Figure 6.4.1). REE patterns for HH1 Gnt show depletion in LREE and enrichment of MREE (except Eu) and HREE compared to PM. HH1 CPx are enriched in LREE and MREE and depleted in HREE compared to PM. HH1 Gnt is depleted in LREE and enriched in HREE relative to HH1 CPx.

Trace-element patterns for HH1 Gnt show a strong depletion in Rb and Th and moderate to minor depletion in U, Nb, La, Ce, Sr, Nd, Zr, Hf and Sm relative to PM. Moderate to minor enrichment of Gd, Dy, Ho, Er, Y, Yb and Lu is also apparent in this sample. HH1 CPx is enriched in Ba, La, Ce, Sr, Nd, Sm, Eu and Gd compared to PM. This sample also show minor depletion in Th, U, Nb, Ho, Er and Y in addition to moderate depletion in Yb and Lu relative to PM.

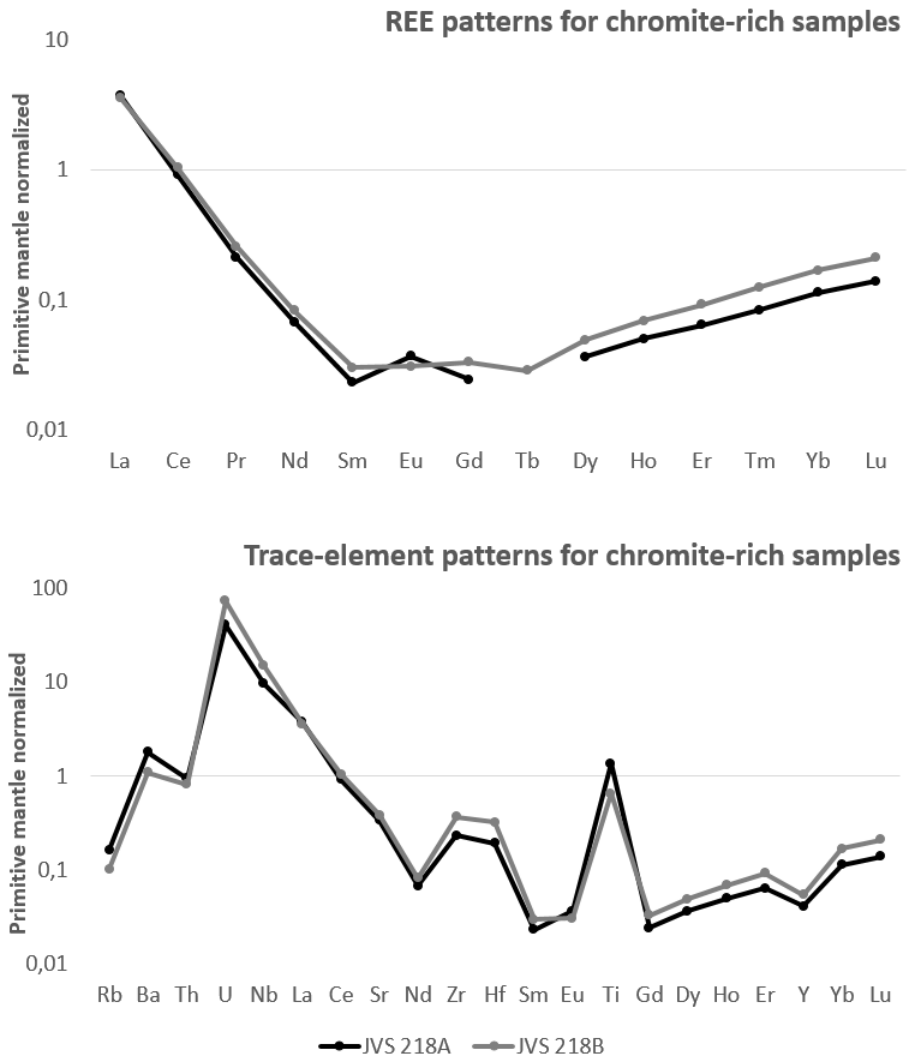

Figure 6.7.7: REE and trace-element patterns for the chromite rich samples from the Gusdal mine.

Chromite-rich samples

Analyses of sample JVS 218A and JVS 218B did not provide results of a quality good enough to provide credible data. Trace element concentrations were analyzed but by comparing the major element results from ICP-OES (Table 6.6.1) to the XRF results (Table 6.5.2) it is obvious that part of the chromite did not dissolve. The reason for including these REE and trace-element patterns is to illustrate the high U and Nb concentrations compared to PM. The concentrations are only 0.88 and 1.59 ppm respectively. Chromite-rich samples like JVS 218A and JVS 218B have not previously been found in the Almklovdalen peridotite. Another reason to include the REE and trace-element patterns of these samples is to evaluate the importance of these samples and compare their composition to the other sampled lithologies.

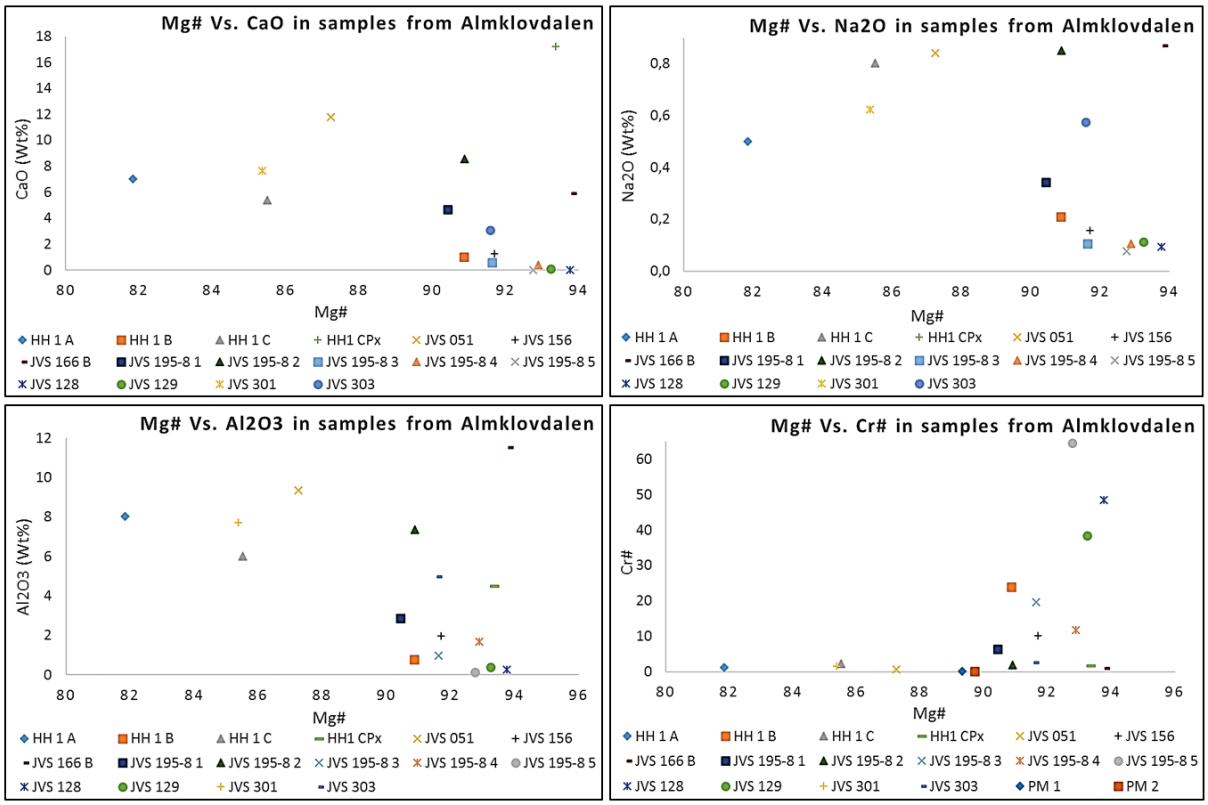

Figure 6.7.8: Diagrams showing whole-rock Mg# and major element oxides and whole-rock Mg# *vs* Cr#.

Relations between whole-rock Mg# *vs* major element oxides and Cr#.

Figure 6.7.8, in which Mg# is plotted against CaO, Na_2O, Al_2O_3 and Cr# provide an overview of the abundance of these components relative to Mg#. The concentration of basaltic components such as the lithophile elements Al, Ca, and Na in addition to the siderophile element Fe indicate either degree of partial melting or degree of enrichment. Cr is a lithophile element; it is compatible in peridotites and enter into the pyroxenes, garnet and spinel. High Mg# generally is an indication of low Fe concentration. Cr# is largely controlled by the Al and high Cr# indicates low Al concentrations. In these diagrams the samples can roughly be divided into two groups but a gradual transition is clearly detectable. Samples HH1 A, HH1 C, JVS 051, JVS 166 B, JVS 195-8 1, JVS 195-8 2, JVS 301 and JVS 303 form one group having high CaO, Na_2O and Al_2O_3 in addition to low Cr# relative to Mg#. This group corresponds to the garnet-bearing samples described in the text related to Figure 6.7.3. The other group contains samples HH1 B, JVS 156, JVS 195-8 3, JVS 195-8 4, JVS 195-8 5, JVS 128 and JVS 129 which have low contents of the basaltic components and high Cr# relative to Mg#. These samples correspond to the olivine-rich samples described in the text related to Figure 6.7.2. Sample HH1 CPx represents diopside separated from the sample HH1 A (garnet pyroxenite) and provides a reference of the degree of enrichment in the samples relative to clinopyroxene.

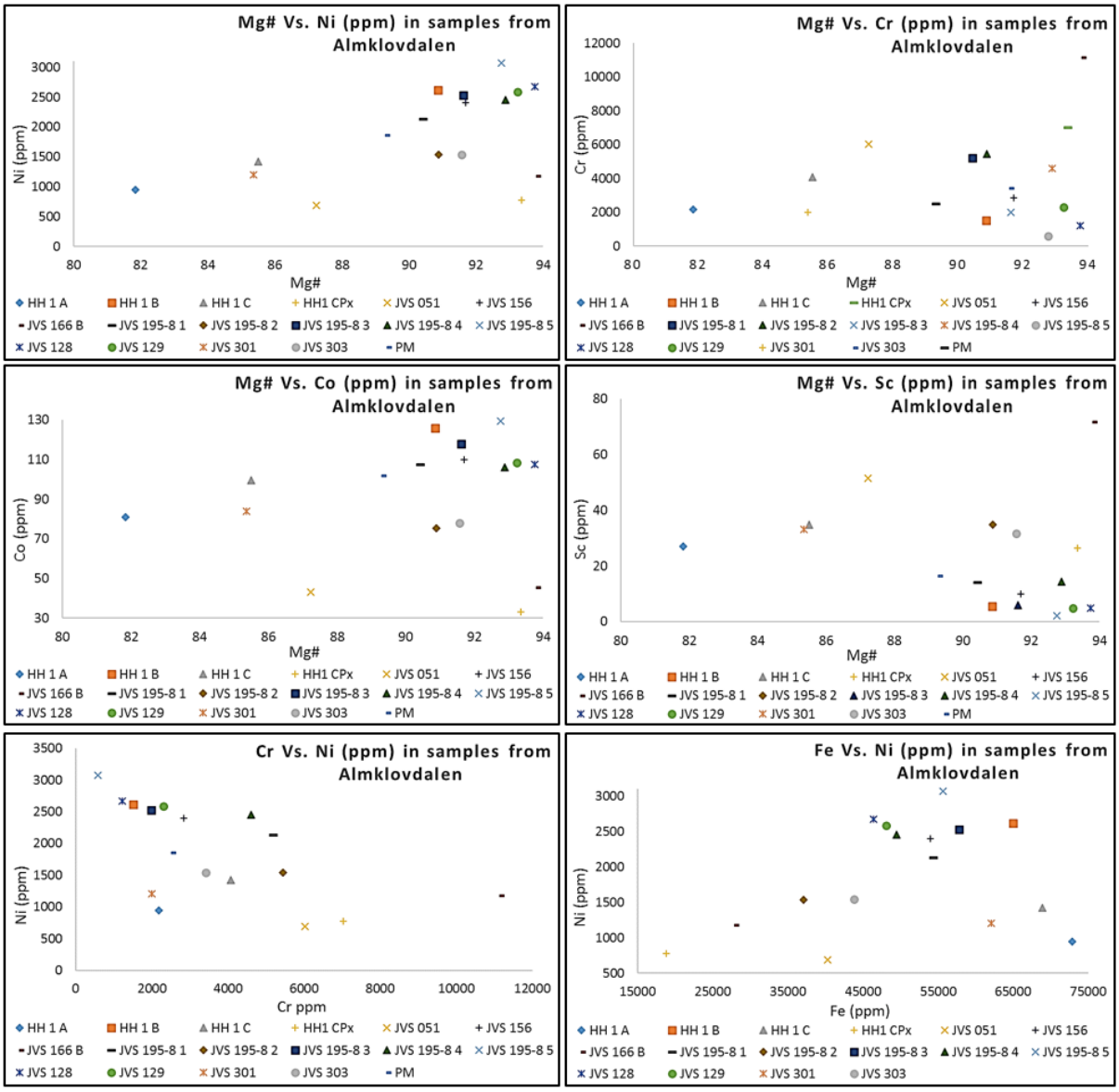

Figure 6.7.9: Diagrams showing the relations between Mg# and dominant mantle rock forming elements (MRFE). The first four diagrams show Mg# *vs* Ni, Cr, Co and Sc concentrations. The two lower diagrams show Ni *vs* Cr and Fe concentrations.

Relations between Mg#, MRFE (Mantle Rock Forming Elements) and PM (Primitive Mantle)

The diagrams in Figure 6.7.9 provide an overview of the relations between Mg#, PM (Primitive Mantle (Palme and O'Neill, 2003)) Ni, Cr, Co and Sc concentrations in addition to the relation between Ni, Cr and Fe concentrations. Ni, Cr, Co, and Sc are MRFE (Mantle Rock Forming Elements) and compatible in peridotites. The upper left diagram shows that olivine-rich samples have Ni concentrations above PM and garnet-bearing samples have Ni concentrations below PM. The upper right diagram shows that Cr concentrations vary from slightly below to approximately equal to PM for most olivine-rich samples. The garnet-bearing assemblages have Cr concentrations from approximately equal to PM to well above. JVS 051, JVS 195-8 1 and JVS 195-8 2 are close to HH1 CPx in terms of Cr concentration except for sample JVS 166B which is abnormally rich in Cr relative to the other samples. The Mg# *vs* Co plot in the middle left diagram shows that the olivine-rich samples have concentrations of Co from slightly above to approximately equal to PM concentrations. Garnet-bearing samples have Co concentrations ranging from approximately equal to PM to well below PM

concentrations. Sample HH1 CPx has very low Co concentration. The middle right diagram show Mg# *vs* Sc. This diagram shows that the garnet-bearing samples have Sc concentrations slightly above PM and the olivine-rich samples have Sc concentrations slightly below PM. JVS 166B show abnormally high Sc concentration relative to all the other samples and PM. The Ni *vs* Cr diagram (lower left) shows that the olivine-rich samples have the highest Ni and the garnet-bearing samples have the highest Cr. The abnormally high Cr concentration in sample JVS 166B relative to the other samples is apparent in the Ni *vs* Cr plot. The Fe concentrations in the samples are represented in all the diagrams by the Mg# but the Ni *vs* Fe plot (lower right) was added to show the more diverse distribution of Ni regardless of Mg concentration.

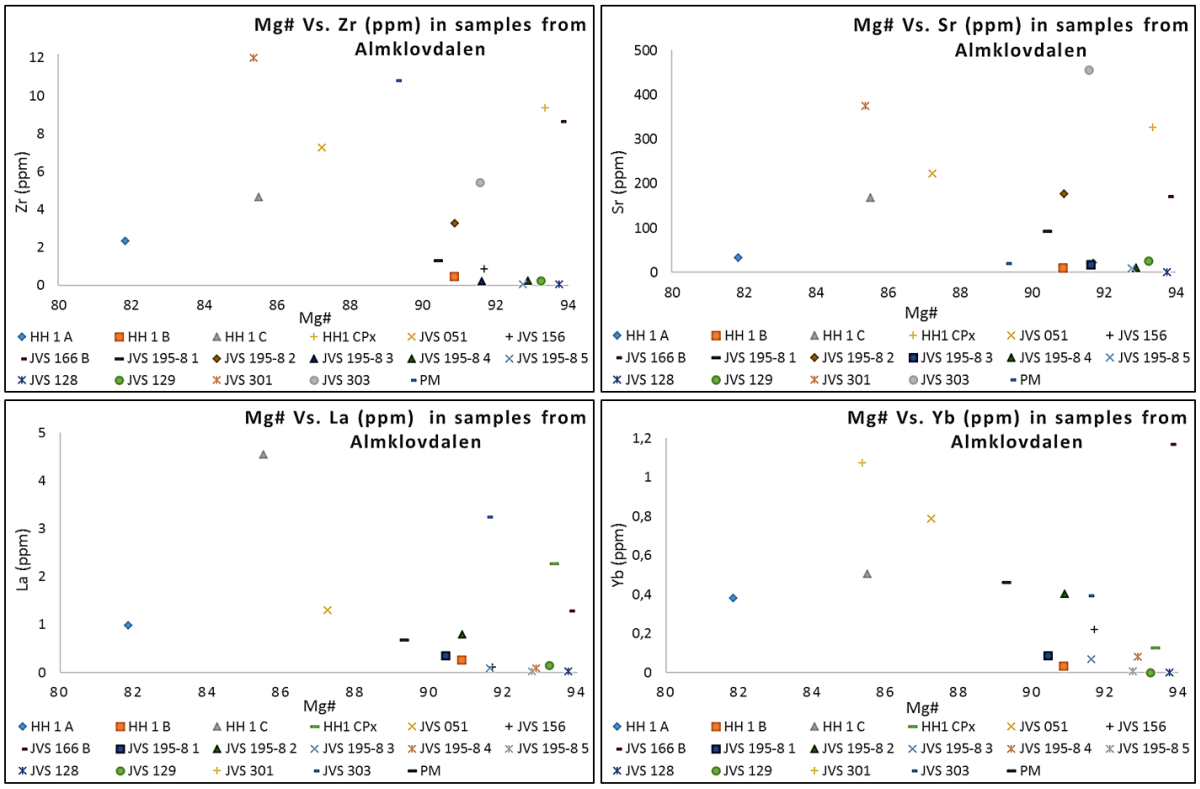

Figure 6.7.10: Diagrams showing the relations between Mg# and Zr, Sr, La and Yb compared to PM. Mg# *vs* Zr represents HFSE. Mg# *vs* Sr represents LILE abundance. Mg# *vs* La represents LREE and Mg# *vs* Yb represents HREE.

Relations between Mg# and Zr, Sr, La, Yb and PM (Primitive Mantle)

The diagrams in Figure 6.7.10 show the relations between Mg# and Zr, Sr, La and Yb. In the upper left diagram Mg# is plotted against Zr, representing the HFSE. All sample are depleted in Zr relative to PM except JVS 301 which has a Zr concentration slightly above PM. Garnet-bearing samples seem to be slightly enriched in Zr compared to the olivine-rich samples which appear to be strongly depleted in Zr (<0.5 ppm). Upper right diagram show relations between Mg# and Sr, representing the LILE. Garnet-bearing samples are all enriched in Sr relative to PM and the olivine-rich samples have Sr concentrations approximately equal or below PM. Lower left diagram shows Mg# *vs* La representing LREE. The garnet-bearing samples are variously enriched and the olivine-rich sample is depleted in La relative to PM. HH1 CPx is relatively strongly enriched in Zr, Sr and La. The lower right diagram shows Mg# plotted against Yb concentrations, representing the HREE. Yb concentrations in garnet-bearing samples are approximately equal to PM with the exception of samples JVS 051, JVS166B and JVS 301

which are enriched in Yb relative to PM. The olivine-rich samples are all depleted in Yb compared to PM.

7. Discussion

7.1 Structural analysis

Large scale regional field relation between peridotites and other lithologies in the WGR

An apparent spatial relation between the ultramafic bodies and the intrusive Sveconorwegian anorthosites can be observed on the regional geological map provided in Figure 2.2.2. This is an interesting relationship but is difficult to explain by the models presently applied for the emplacement of the peridotites. The presently accepted evolution models for the WGR only provide the deformation processes during over-thrusting of the nappe units and the subduction event during the Caledonian orogeny as possible explanations for such relationship. The large scale Nordfjord-Sogn Detachment Zone (NSDZ) could possibly have caused such apparent relationship between these lithological elements but the spatial coexistence of peridotites and anorthosites is not restricted to the area affected shear related to this event. Throughout the whole WGR large peridotites and anorthosites are located in close proximity. Reactivation of structural weak zones in the crustal gneiss might be a plausible model that can explain emplacement of these lithological elements in such consistent spatial proximity. This might account for both models for the emplacement of the peridotites. 1) Up-thrusting and emplacement of the peridotite from the Baltic SCLM during the Gothian orogeny and formation of the Baltic continental crust followed by reactivation of structurally weak zones and intrusion of anorthositic or/and gabbroic magmas during the Sveconorwegian orogeny. 2) Intrusion of anorthositic or/and gabbroic magmas during the Sveconorwegian orogeny followed by reactivation of the crustal weakness and sinking emplacement of the peridotites during the Caledonian subduction event. A few locations where the peridotites and the anorthosites occur in direct contact and where peridotites occur within anorthosites further entangle this relationship. This possibly promote the necessity for a more complex explanation and reconsideration of the model for emplacement of the peridotites and/or geological evolution of the WGR. Another solution to this problem that the ages of these elements can be different than previously suggested. The Archean zircons from Almklovdalen analyzed by Beyer et al. (2012), might represent inherited zircons from the gneiss implying that they may be Gothian as previously suggested by Sm-Nd mineral dating (Brueckner and Medaris, 1998). The drainage from which the zircons were collected passes through gneiss and sedimentary deposits before crossing the peridotite massif. The whole-rock Re-Os and sulfide Re-Os model ages still support the Archean ages (Beyer et al., 2004). If they are Archean it is still possible that Archean SCLM exists at deeper levels underneath Baltica increasing the likelihood of the up-thrusting model. The anorthosites may also be older than previously thought and the if the anorthosites were emplaced by the same process as the peridotite during the Gothian orogeny their spatial relationship, contact relation and structural similarity would be explained.

The Almklovdalen peridotite

The new geological map of the peridotite massif at Almklovdalen constructed from field observations gathered as part of this survey provide a more detailed knowledge about its extent (Figure 6.3.2 and Appendix 1). Structural features with potential important implications for the emplacement models were found and are discussed below.

An abrupt change in the strike of the contact against the gneiss was mapped at Raudekleivane (No. 11, Figure 6.2.3). Three Fe-rich eclogite boudins at this location contains evidence of high pressure metamorphism indicating that they experienced the same prograde metamorphism as the gneisses, which poses implications for the sinking intrusion model (Griffin and Qvale, 1985). Garnets in these eclogites are described to have rims with higher Mg/Fe values than the cores companied by rutile and omphacite inclusions implying that they are Fe-Ti-rich compared to the garnet pyroxenites. Griffin and Qvale (1985) further describes Cl-rich Fe-pargasite, K-feldspar, apatite, ilmenite and pyrite inclusions in the garnet cores, which is common in the eclogites in the gneiss. They suggest that this represents evidence of amphibolite-facies metamorphism that preceded prograde metamorphism to eclogite facies. This implies that the enclosing peridotite experienced high-pressure metamorphism and the same hydration as these eclogites, and the eclogites in the gneisses, prior to the UHP eclogite-facies metamorphism. It is difficult to explain the sinking intrusion model in terms of such metamorphic evolution and this provide evidence for an emplacement prior to the Caledonian subduction event. Another explanation is that these eclogites are foreign to the peridotite complex, belong to the crustal gneisses and were structurally emplaced during the Caledonian subduction event. The strike orientation of the eclogite boudins is parallel to strike of the abruptly changed contact and the close spatial (<25 m) relation to this structure might indicate that they are foreign to the peridotite complex. Both the sinking intrusion model and the up-thrusting model imply that the peridotite has moved through considerable volumes of surrounding rock of various composition. Anorthosite, gabbro and amphibolite are widespread through the WGR and it would not be unlikely that some fragments of these lithologies was incorporated into the peridotite during emplacement. Considering the present occurrence of the eclogites as boudins/lenses such foreign elements would be plausible to expect from both emplacement models. The strong similarity in texture and occurrence of the eclogites at the northern contact zone in the Gusdal mine, might imply necessity for a similar explanation. However, such emplacement of the these eclogites is structurally difficult to imagine and they are suggested to provide evidence favoring the up-thrusting model Gothian emplacement.

The outcrop of ultramafic rock north-east of Åhaug is clearly separate from the rest of the peridotite massif and has to be considered an individual body (No. 1, Figure 6.2.3). This location was mined for chrysotile for a short period and hydration is much more extensive in this body than in the relatively chrysotile free dunite at the Gusdal mine. Another individual body of peridotite approximately 500 m north of the was also mined for chrysotile and show similar evidence for higher degree of hydration (No. 2, Figure 6.2.3). Additional two smaller m^2 scale separate extensively hydrated bodies were found near the large massif, one on the path from Sunndalen to Helghornsvatnet (No. 3, Figure 6.2.3) and one south of the farm Skaret (No. 3, Figure 6.2.3). The higher degree of hydration fond in these bodies illustrate that they have experienced higher degree of deformation resulting in higher permeability and connectivity providing access for the silica-rich fluids to impose more extensive hydration. The geological map provided in Figure 2.2.2 illustrates the presence of many larger bodies of ultramafic rock throughout the region, which demonstrate that fragments of ultramafic rocks from m^2 to km^2 size are scattered through the region and a spatial relationship is apparent between these bodies. This indicates either an emplacement mechanism producing such distribution or a strong deformation process ripping apart larger units. Such deformation and dismemberment of the ultramafic bodies can be explained by both the up-thrusting model and the sinking intrusion model.

The central southern section of the contact zone just north of Eidevatnet (No. 12, Figure 6.2.3) has an irregular structure compared to the rest of the peridotite massif and is worth noting. The strike of the contact deviates strongly from the rest of the massif. Folding of the peridotite around a section of the gneiss in such a manner should have affected the main foliation which in rest of the massif shows

strong parallelism to the strike of the contact. Such parallelism is not present in the arc of this structure and a crosscutting relationship where the foliation is perpendicular to contact was observed. This structure could be generated by a remaining slice of gneiss covering the peridotite in this area but by following the depression eastwards from Eidevatnet it is apparent that gneiss is present at lower altitudes than peridotite. Another interpretation of this structure is that the peridotite is relatively thin in this area and the underlying gneiss is exposed. This could be interpreted as a contradiction of parallelism between the foliation and the strike of the contact and previous assumptions by Cordellier et al. (1981) that the peridotite occur as a cone-shaped structure. The most likely explanation is that the peridotite is simply folded around a section of the gneiss. This is supported by the strike of the contacts along this structure being parallel to the axial planes of the mesoscopic category 1 folds at the field area near Helghornsvatnet. The lack if kinematic indicators in the homogenous dunite would prevent evidence of such folding to be observed.

The field area near Helghornsvatnet

Mapping of the selected field area near Helghornsvatnet resulted in a detailed geological map (Figure 6.3.4) and a profile (Figure 6.3.5) with interpreted vertical extent and structural geometry of the lithologies within this area. Such detailed map and profile has previously not been available and indicate the spatial position of these garnet-bearing lithologies within the peridotite massif. The profile indicates that the present position of the slice of garnet-bearing peridotite is in the highest section of the massif. The present topographical position of the enriched section indicates an overturning or inversion of the massif during emplacement and/or later deformation. Similar garnet-bearing assemblages at the Gusdal mine and at Raudehaugen are also located within the highest topographical levels of the peridotite massif. At those location this could be explained by gravitational sinking assuming that they represent the lower part of the peridotite, but this has tectonic implications for the Helghornsvatnet outcrop. By combining these observations, it would be necessary to explain the area near Helghornsvatnet by transport of the basaltic magmas and metasomatic fluids throughout a section of depleted dunite and formation of a mesoscopic lens or pocket of enriched peridotite. In SCLM it is not uncommon that cumulates form as lenses near the mantle-crust boundary. Such explanation imply that the garnet peridotite represents a cumulate in which layering would be likely to form during fractional crystallization. This explains both the appearance aureoles of dunite richer in basaltic components and lack of crosscutting relations between the layering of garnet-bearing assemblages and its retrograded equivalents. It also explains why the whole area mapped as dunite containing clinochlore layers and garnet lherzolite/wehrlite are richer in basaltic component than its surrounding dunite. Such processes provide an alternative explanation compared to the enrichment model suggested by Beyer et al. (2006).

Foliation

Cordellier et al. (1981) divides the foliation within the peridotite into three categories. The S_1 foliation in relatively unaltered garnet-bearing assemblages is related to D_1 in dry conditions and the S_2 foliation in chloritized assemblages related to D_2 in hydrated conditions. By interpreting the foliation measured during field work during this survey it was not possible to detect a difference between the orientation of the foliation in garnet-bearing assemblages and their retrograded equivalents. The genetic relationship between these two mineral assemblages are discussed in the geochemical synthesis. According to Cordellier et al. (1981) S_1, S_2 and S_3 foliations are parallel at the field area near Helghornsvatnet. From the structural data acquired for this Thesis it is not possible to distinguish between neither of these foliation categories by their orientation at this location and their parallelism to the strike of the contact zone is apparent. Considering such parallelism, it seems likely that the foliations of Cordellier et al. (1981) represent the same foliation in different mineral

assemblages correspond to a gradual metamorphic retrogression from eclogite to upper amphibolite facies. Two models for the formation of this foliation are suggested. 1) The foliation is related to sinking intrusion of the mantle fragments into the Baltic crust and subsequent mesoscopic folding of the whole peridotite massif during the Caledonian subduction event. 2) Development of the foliation by gravitational sinking during the Gothian orogeny and the large scale folding of the whole peridotite massif during the Caledonian subduction event reactivated the slip system. Considering the reconstructed trajectories for high temperature foliation during the Caledonian orogeny reconstructed by Hacker et al. (2010) (Figure 2.1.10), the foliation seems to have been present in the peridotite before this deformation. The foliation in the gneiss ($S`_3$ and S_4 of Cordellier et al. (1981)) seem to have formed around the peridotite massif and a crosscutting relation between the foliation in the surrounding gneiss and the foliation in the peridotite is apparent at large sections of the peridotite. This provide a strong argument for development by the up-thrusting model (model 2)) suggested above. However, model 1) does also explain the orientation of the internal foliation in the peridotite by the sinking of the massif into the gneiss. Formation of a different orientated foliation in the surrounding gneiss can be explained by different vectors of movement in the gneiss and the peridotite during the sinking intrusion process in the subduction zone.

Lineation

The L_3 lineation form Cordellier et al. (1981) provided on the geological map in Figure 6.3.3 seems to be generally steeper plunging within the peridotite which indicate a more vertical movement compared to the surrounding gneiss. The more horizontal orientated L_4 lineation in the gneiss shows crosscutting relation to the strike of the contact against the peridotite at the same locations as the S_4 foliation. At the field area near Helghornsvatnet the L_1 and L_2 lineations are horizontally plunging towards the SW while vertically plunging lineation is dominating the surrounding dunite. Distinguishing between L_1 which and L_2 is not possible from the stereo plots (Figure 4.3.2) and they are described as subparallel by Cordellier at al. (1981). However, the L_2 lineation seem to be representing two populations. One population parallel to L_1 and one population of more steeply plunging lineation. By correlating this observation to the lineation near Helghornsvatnet (Figure 6.3.3), it would be plausible to assume that the steeply plunging population represents the more depleted dunite surrounding the chlorite-rich dunite and garnet lherzolite/wehrlite (Figure 6.3.4). More gently plunging lineation parallel to L_1 can be assumed to represent lineation within the chlorite dunite and garnet lherzolite/wehrlite. This can be taken as an indication of different structural elements at this location, which is supported by the fold axial plane and the fold axis orientations of category 3 folds at HH1 and HH2. On the other hand, fold axes of category 1 folds, the majority of category 2 folds and category 3 folds at the HH4 and HH5 seems to be subparallel to L_1 and L_2.

Folds

Category 1 folds correspond to the F_1 open folds of Cordellier et al. (1981) which they relate to the vertical trusting of Baltic SCLM into the Baltic crust during D_1 which is the earliest deformation in the up-thrusting model. From the data and field observations analyzed during this Thesis it is suggested that the category 3 fold are second order parasitic folds in the hinges of category 1 folds and formed simultaneously. Such relationship is particularly apparent at the HH1 and HH2 localities (Figure 6.3.16 to Figure 6.3.19). The slightly different orientation of these folds compared to the category 2 folds can be related to differences in rheological properties between the garnet pyroxenites and the dunite matrix. The garnet pyroxenites folded by the category 3 folds are also physically thicker than the clinochlore bands in which the category 2 folds occurs. However, it is suggested that category 2 folds formed after category 1 and category 3 folds. The category 2 folds correspond to the F_2 of

Cordellier et al. (1981) which suggested that these formed during gravitational sinking at P-T conditions corresponding to the upper amphibolite facies and in hydrated conditions during the Gothian orogeny. By considering the parallelism between the axial planes and fold axes of category 2 fold and the orientation of the dominant foliation it seems likely to suggest that these two features was generated simultaneously. This imply that hydrated conditions and the retrogression of pyroxenes to amphibole and clinochlore, which is apparent in the folded layers, also occurred during the Gothian orogeny according to the up-thrusting model. The plastic deformation mechanism combined with the apparent fold geometry of category 2 folds indicates that they developed by mylonitization which was generated by sub-simple shear during NNW-SSE shortening. This could also correspond well to the shortening direction during the Caledonian subduction event. However, it is no contradiction to the up-thrusting emplacement model to suggest that the dominant foliation and category 2 folds was generated during this event. This would explain the hydration and the resulting retrogression by percolation of subduction zone fluids. Mylonitization can also be related to the mesoscopic folding of the entire peridotite massif (S_3 of Cordellier et al. (1981)) . Considering the position of the folded area near Helghornsvatnet in relation to the mesoscopic fold geometry it is likely that such deformation occurred at this location. The mesoscopic folding event may also have relocated the category 1 and category 3 folds implying that their original orientation was different.

To explain the category 1 folds and category 3 folds by the sinking intrusion model it is necessary to relate them to the earliest deformation process of this model. Considering the relationship between category 1 and category 3 folds described above, simultaneous formation is required also in the sinking intrusion model. It is suggested that they were generated as first order folds by active folding of garnet pyroxenite layers during plastic deformation of Laurentian SCLM. This could have occurred by deformation of the mantle wedge or as part of the emplacement process from the lower hanging wall and into the subducted slab. The formation of category 2 folds is suggested to have occurred either within the mantle wedge before being scraped off and sinking into the gneiss or as described above within the gneiss. The NNW-SSE shortening direction during mylonitization which formed the category 2 folds appears to correspond to the coaxial approximately E-W stretch and the movement directions of the continental slab during the Caledonian subduction and eduction events. It seems most likely to assume that category 2 folds were generated by deformation during or after ductile intrusion into the crustal gneisses considering the nature of the hydration. In addition, the parallel foliation corresponds to the trajectories for high temperature foliation reconstructed by Hacker et al. (2010) (Figure 2.1.10).

Hydration can be related to the subduction zone fluids which explains the retrogression of pyroxenes to amphibole and clinochlore. Penetrative serpentinization is restricted to a 30-70 m thick reaction zone along the contact against the gneiss and restricted zones along the dominant foliation affected by faulting, subsequent fluid percolation and hydro-fracturing. The core of the peridotite massif seems to be relative unaffected by hydration and at the field area near Helghornsvatnet no evidence of chlorite veins or chlorite bands was found. The latter imply that the field area was less affected by hydration during the mesoscopic folding of the massif and later fluid percolation. However, this can also be interpreted as evidence for the peridotite being incorporated in the gneiss and protected from the subduction zone fluids during the whole Caledonian subduction event. If the peridotite was part of the Laurentian hanging wall it would be likely that it experienced extensive impregnation by fluids transpired from melting of the subducted felsic crust. It is hard to imagine that a fragment of the hanging wall appears to be so sparsely affected by mass transfer from metasomatic fluids and a crossing of the crust-mantle interface at UHP conditions.

All fold categories folds seem to have formed by plastic deformation mechanism, possible flexural flow or flexural shear. The rheological contrast between garnet- and pyroxenite-rich layers and the dunite matrix would provide a low viscosity slip system. Such deformation occurs at UHP conditions and it would be plausible to suggest that this occurred at mantle depths. Plastic deformation of the mantle wedge in a subduction zone during sinking into the subducted slab and during subsequent exhumation provides an environment which explains the geometry of all fold categories. An example of such plastic deformation in orogenic peridotites can be found in the Beni Bousera peridotite, northern Morocco (Palme and O'Neill, 2003). This peridotite is considered to derive from the hanging wall in a subduction zone. Isoclinal folded and boudinaged compositional layering representing zones enriched by dikes of mafic melt intrusions within the peridotite and show strong similarity to its potential equivalent at Almklovdalen. The boudinage along the northern contact of the Gusdal mine indicates presence of an extensional regime. Extension at UHP conditions could have pulled intrusive dikes into alignment and generated compositional layering such as those found at the field are near Helghornsvatnet. It is also possible to explain all fold categories by the up-thrusting model and the low influence of subduction zone metasomatism provide a strong argument for this model. Evidence of HP metamorphism in garnet cores found in eclogites further support the up-thrusting model (Griffin and Qvale, 1985). Considering the P-T conditions estimated for the Caledonian subduction event in this area of the WGR, the up-thrusting model imply that these conditions did not overprinted pre-Caledonian deformation features.

The close spatial relationship between unaltered and hydrated garnet peridotite and garnet pyroxenite represented by the structural elements discussed above raises the question of their relationship. Low access of fluids in the zones where the relatively fresh garnet-bearing assemblages occur explains low degree of retrogression and alteration to amphibole in these assemblages. Higher access to fluids causes alteration of amphibole to clinochlore. Some of the relatively fresh garnet-bearing assemblages occur in a less regular layered manner than the chloritized assemblages. This is consistent with low degree of penetrative metasomatism and hydration caused by the subduction fluids. Internal crosscutting relations can to a minor extent be observed and show similarity to layering/banding but they can also be interpreted as dike-like intrusions with penetrative enrichment aureoles developed by metasomatic processes. Crosscutting relationships in addition to deviating fold axial plane and fold axis orientations are to a minor degree apparent at the HH1 locality (Figure 6.3.13) and at the HH4 locality. No crosscutting relation was observed between chloritized bands during field mapping.

The garnet-bearing and clinochlore-rich layers serve as kinematic indicators within relatively homogeneous dunite. This raises the question of the extent of strain within the peridotite massif. It can be assumed that the whole massif experienced the same deformation and lack of kinematic indicators is the reason why the folding is not detectable in the dunite. This explain the lack of well exposed deformation features such as those at the outcrops near Helghornsvatnet. The magnitude of strain may vary among the lithological elements due to differences in rheological properties. One open fold is described at Raudekleivane (No. 11, Figure 6.2.3) (Griffin and Qvale, 1985) and at Raudehaugen (Figure 6.2.3), another one open fold is described in a garnet peridotite layer similar to the ones at Helghornsvatnet (Carswell, 1981). The descriptions indicate that these folds correspond to the F_1 of Cordellier et al. (1981) and the category 1 folds of this survey. The isoclinal to open folding of garnet-bearing assemblages (category 3 folds) can also be found in an outcrop at Raudehaugen which seems to represent an lithological equivalent to the field area near Helghornsvatnet. Such folds are not known from other locations; neither are the isoclinal to tight folds in clinochlore-rich layers (category 2 folds).

Other structural elements

Cleavage observed in the fold core of category 1 folds (Figure 6.3.21 and 6.3.22) show strongest parallelism to the dominant foliation but can also be considered as axial plane cleavage. By field observation the cleavage is most similar to axial plane cleavage and the orientation is perpendicular to the general shortening direction. Orientation of the fold axial plane may vary due to influence of variation in geometry which provide a plausible explanation for the slightly different orientation of the axial plane and the axial plane cleavage. A slightly radiating appearance that can be seen in the cleavage orientation at the photo in Figure 6.3.21 contradicts that it simply represents foliation, which would be parallel at such short distance.

Orientation of the abrupt change in orientation of the clinochlore layering occurring at approximately the same location show strong parallelism to the cleavage regarding orientation but has the characteristics of simple shear or sub-simple shear. It seems more likely that this feature was generated by shearing of garnet peridotite layers during formation of the category 1 folds than that it is related to the cleavage. The texture of the clinochlore (Figure 6.3.20) indicate that elongation and retrogression occurred during both sinistral and dextral ductile shear with access of fluids. Alteration of pyroxene to clinochlore is particular apparent in lower left photo in Figure 6.3.20 where remnants of diopside can be observed within the clinochlore matrix. Evidence of such simple shear was just found at a few locations and the photo series in Figure 6.3.20 further illustrates the complexity of the deformation and geometry that dominate the layering/banding. This geometry can be considered as an indication for that the clinochlore are not simply layering but more likely stretched veins/dikes of fertile magma intrusions. This is particularly apparent in the lower right photo but such deformation can still be explained by non-symmetrical macroscopic folding accompanied ductile shear. However, no crosscutting relations was fond between these layers and they show striking similarity to layering in cumulates.

7.2 Geochemical Synthesis

The sinking intrusion model is most consistent with evidence of an Archean depletion event in the peridotite at Almklovdalen (Beyer et al., 2004; Beyer et al., 2012; Beyer et al., 2006). Average Mg# 93.2 for the most olivine-rich samples analyzed as part of this Thesis confirms the high degree of depletion. This corresponds to other analytical results (av. Mg# 93.1 from Griffin et al. (2009) and av. Mg# 93.0 from Beyer et al. (2006)). The low abundances of basaltic components in the dunites were documented both during this survey and by Beyer et al. (2006) and are considered as further evidence of high degrees of partial melting. As no evidence of Archean crust or SCLM underneath Baltica is currently known, a Laurentian provenance is suggested (Beyer et al., 2012). The average Mg# of 93.1 described from dunite xenoliths found in basaltic dikes in Eastern and Western Greenland (Bernstein et al., 2006; Bernstein et al., 1998; Bernstein et al., 2007; Griffin et al., 2009) provide a strong indication of highly depleted Archean SCLM beneath Laurentia. These xenoliths also show an increase in Cr above 0.6 wt% Al_2O_3 in addition to varying Al contents which is suggested to be related to refertilization. Their Mg# in addition to the Cr-Al relation and Al variation show strong similarity to the same aspects documented in the garnet peridotite at Almklovdalen.

Geochronological, geochemical and geothermobarometric data indicate that garnet-bearing peridotites at Almklovdalen represent rare assemblages of subcontinental lithospheric mantle emplaced into the crust by tectonic orogenic processes (Griffin and Qvale, 1985; Sun and McDonough, 1989). Intrusion of melts while the peridotite protoliths where located at mantle depth are suggested to have generated the dike-like bodies of garnet bearing wehrlite, websterite, eclogite

and pyroxenite surrounded by garnet peridotite (Brueckner and Medaris, 1998; Medaris Jr, 1984; Osland, 1997). Both field observations and analyzes conducted as part of this Thesis confirm that enrichment by more fertile magmas is likely but also provides evidence that the layering of garnet pyroxenite and its retrograded equivalents show strong similarity to such assemblages in magma cumulates. At locality HH1 (Figure 6.3.15) and HH2 (Figure 6.3.17) fertile aureoles around garnet pyroxenite layers/dikes interlayered with dunite are well exposed and can be explained both by enrichment and fractional crystallization in magma cumulates. It is also possible that both processes have occurred and such combination will explain the field relations, compositional variation and possible also the strong gradient in degree of alteration.

Olivine-rich samples

REE patterns of the olivine-rich samples show depletion in all elements compared to PM (Figure 6.7.2). The highly depleted samples are most depleted in HREE and MREE, indicative of melt residues affected by later enrichment in LREE. In the REE patterns for the garnet-bearing assemblages this trend is consistent with the high LREE relative to PM (Figure 6.7.3). The LREE are incompatible elements and would partition into silica-rich melts. Such trends can therefore be taken as indications of metasomatic enrichment by melts rich in LREE represented by the garnet pyroxenite and eclogite dikes. Trace-element patters for the olivine-rich samples (Figure 6.7.2) show low concentrations of HFSE (High Field Strength Elements) Zr, Hf and Ti relative to PM. The patterns also reveal low Rb relative to Sr and high Nb relative to La and Th, which is typical of depleted dunites (Palme and O'Neill, 2003). Further evidence is provided by trace-element patterns for garnet-bearing samples that show strong enrichment in Ba, Sr and Nd relative to most other elements (Figure 6.7.3); these elements concentrated in the CPx that accompanies the garnet in most samples. Irregular patterns of U, Nb, La and Ce were detected in both the olivine-rich and the garnet-bearing samples. The volumetrically dominant dunite do clearly represent a depleted residues after high degrees of partial melting. This is further confirmed by the high Mg# >93 for the most olivine-rich samples, low bulk concentration of basaltic components and high concentration of Ni and Co.

Garnet-bearing samples

All garnets at the Almklovdalen peridotite are considered metamorphic prophyroblastic pyrope garnets with minor Cr and Ca substitutions. Enstatite and diopside crystallization are also considered as metamorphic. Crystallization occurred in eclogite facies P-T conditions and retrogression in hydrated condition during subsequent eduction and exhumation resulted in the amphibole and chlorite minerals. The garnet-bearing samples all have higher abundances of CaO, Na_2O and Al_2O in addition to high Cr# relative to Mg# compared to the olivine-rich samples (Figure 6.7.8). Peridotites highly depleted in basaltic components such as Fe, Al, Ca, Ti and Na are commonly explained by extraction of mafic melts from a primitive mantle sources (Beyer et al., 2006). High concentrations of basaltic components in garnet-bearing assemblages compared to PM can be explained by refertilization of depleted residues but fractional crystallization in magma cumulates can also produce similar trends. The concentration of basaltic components does not by itself provide a conclusive answer to the question of which of these processes has produced such trends in the peridotite at Almklovdalen. The high concentrations of Ni and Co in the olivine-rich samples and the high Cr and Sc concentrations in the garnet-bearing samples (Figure 6.7.9) further support the trends detected from the major element oxides and the variation of Cr# *vs* Mg#. The diagrams also show enrichment and depletion of MRFE compared to PM concentrations. This gives indications of which mineral phases each individual element is compatible and which mineral phase has highest affinity for each individual element under the conditions these samples represent. Ni, Cr, Fe and Co are compatible both in olivine and pyroxenes while Sc is compatible in pyroxenes, to a lesser degree in

garnet, but not in olivine. Ni, Fe and Co are siderophile elements and Cr and Sc are lithophile elements. It is apparent from these diagrams that the sample series represent a gradual enrichment of from highly depleted dunite to enriched garnet pyroxenites relative to PM.

A few irregularities in the trace-element patterns of sample JVS 301 and JVS 303 has to be mentioned. These samples represent the northern contact zone at the Gusdal mine (Figure 6.4.3). JVS 301 shows particularly strong enrichment in the lithophile elements Rb, Ba Th and U relative to other samples. This sample represents a highly altered dike which differs strongly from the other lithologies found in the peridotite. The high degree of alteration is evident from the high content of clinochlore and amphibole incorporating small pods of less altered to fresh material rich in enstatite (Figure 6.4.24). The high orthopyroxene content indicates a relation to harzburgite while the other lithologies at this location are rich in clinopyroxene and related to lherzolite. The harzburgite dike stretches continuously for more than 100 m and is approximately 0.5 m wide. Other dikes found in the same area are strongly boudinaged, do not have the same continuity, and in appear less altered. Eclogite boudins seem not to have aureoles of fertile dunite but on the contrary show abrupt contacts between the two lithologies (Figure 6.4.3). The composition of these eclogites differs from the garnet pyroxenites by a higher omphacite content at the expense of diopside. This is evident by higher Fe, Ca and Na abundances (Griffin and Qvale, 1985). Some of the eclogite boudins have amphibole rims, from 2 cm to 50 cm thick, while the garnet pyroxenite dikes have low amphibole, no rims and appear relatively fresh. Alteration of the eclogite assemblages appears to have been caused by retrogression in hydrous conditions from eclogite to upper amphibolite facies. Unaltered garnet pyroxene cores remain in most amphibolite assemblages. Eclogite boudins also show large variations in garnet/pyroxene ratios. Eclogites along the northern contact at the Gusdal mine ranges from those almost entirely composed of garnet to some almost entirely composed of pyroxene. These differences indicate that the garnet- and pyroxene-bearing assemblages can be divided into three distinct groups. Variations in composition and style of alteration indicate possible compositional differences of the magma sources and may imply different times of emplacement. Such irregularities can be interpreted as indication of several enrichment events from slightly different magma sources but are more likely to have been caused by compositional differences and differences in partitioning between the mineral assemblages. This is an important observation these three types of garnet-bearing assemblages can provide valuable evidence regarding emplacement and provenance.

The HH3 sample series

The sample series representing the HH3 locality (Figure 6.7.4) confirms a genetic relationship between the garnet-bearing and the more olivine-rich assemblages. These samples represent a gradual enrichment over a range of 5 m and development of compositional banding. Penetrative relative enrichment occurs as sequential compositional banding near garnet pyroxenites, representing zones with more fertile lherzolitic composition. The range of compositions from garnet pyroxenite to depleted dunite are clearly apparent from their REE and trace-element patterns. The map of this location provided in Figure 6.4.3 and Figure 6.7.5 visualizes the compositional banding. This location also demonstrates the strong gradient in retrogression from relatively fresh garnet websterite to clinochlore bands within 1 cm. REE and trace-element patterns in the clinochlore are comparable to these patterns in garnet pyroxenites. Beyer et al. (2006) concluded that the garnet peridotites including their retrograded equivalents have a consistent close relationship to garnet pyroxenites, websterites, wehrlites and the eclogites. Field observations of the clinochlore banding provided indications of retrogression of both garnets and diopside to clinochlore. This can be taken as evidence for a genetic relation between the garnet-bearing assemblages, clinochlore-rich bands and the volumetrically dominant depleted dunites.

HH1 Gnt and HH1 CPx

REE and trace-element patterns for the samples HH1 Gnt and HH1 CPx (Figure 6.7.6) document the partitioning of the individual elements between garnet (pyrope) and clinopyroxene (Cr-diopside). Garnet has a strong affinity for HREE and clinopyroxene has strong affinity for LREE, Eu and Gd. Trace-element patterns show that clinopyroxene has strong affinity for Th, Nb, la, Ce, Sr, Nb, Sm and Eu compared to the garnet. This explains the slightly different REE pattern of samples HH1 A representing garnet websterite and the most garnet-rich sample. JVS 303 also shows a REE pattern similar to HH1 A but the differences in trace-element patterns between these samples, in addition to field observations, indicate a different explanation for the patterns of JVS 303. This may be related to the clinochlore and enstatite content of sample JVS 303.

Chromite-rich samples

The chromite-rich samples show distinct REE and trace-element patterns compared to all other samples (Figure 6.7.7). JVS 218A represents separated magnesiochromite and JVS 281B represents bulk-rock magnesiochromite in a clinochlore matrix (Figure 6.4.21). These samples are particularly interesting with regard to PGE (Platinum Group Elements) which will be concentrated in the chromite in this geological setting. Strong depletion in Pr, Nd, Sm, MREE and HREE relative to PM characterize these samples. Trace-element patterns show enrichment in the lithophile elements Ba, Th, U, Nb, La, Zr, Hf and Ti relative to the other elements in strong contrast to the rest of the sample series. These samples were found approximately 180 m from the contact against the gneiss, which is much further from the contact than any of the known garnet-bearing assemblages in this area. The location is approximately in the center of the Gusdal mine (Figure 6.4.3) and no similar lithology has previously been found during the mining activity or in other peridotites. This raises the question of origin, timing and process of emplacement and relationship to the other lithological elements in the peridotite for these assemblages. The strong similarity in composition of these samples indicate either that the clinochlore are retrograded magnesiochromite or that the magnesiochromite crystallized from the clinochlore. From the similarity in composition it seems likely that the clinochlore is retrograded magnesiochromite. It is plausible that a partitioning of elements between the two phases would occur if the magnesiochromite crystallized from the clinochlore. The magnesiochromite occurs as subhedral octahedral crystals in the clinochlore matrix and a retrogression would not leave the crystal shape intact. This observation suggests a third possibility which includes both processes; the magnesiochromite was partly retrograded to clinochlore and a change in access of fluids and/or change in P-T conditions allowed for recrystallization of the magnesiochromite crystals. The latter seems to be the most realistic explanation for both the similarity in composition and the occurrence of magnesiochromite as subhedral crystals. Samples JVS166B, which is from HH5 locality, have Cr concentrations close to twice the concentrations in the other garnet-bearing samples. This sample show similarity in texture and field relation but the REE and trace-element patterns provide evidence that it is to be considered a retrograded pyroxenite.

Geochemical implications

The relatively homogenous olivine-rich samples are by Beyer et al. (2006) considered to represent residues after high degree of partial melting which is consistent with the result from this survey. Evidence that the garnet-bearing samples and their retrograded equivalents represents basaltic dikes infecting penetrative enrichment aureoles in the surrounding dunite matrix is not conclusive. The mixing trends apparent in all diagrams (Figure 6.7.8, Figure 6.7.9, Figure 6.7.10) strongly support metasomatic enrichment in basaltic components, including REE and trace-elements but such trends

can also occur in ultramafic magma cumulates by fractional crystallization. Further support for the cumulate model is provided by the sequential occurrence of pyroxene and forsterite later exposed to UHP metamorphism. The eclogite boudins and dike-like veins with abrupt contact towards the surrounding depleted dunite support the enrichment model. The strong similarity of the REE and trace-element patterns between most samples and the gradual enrichment from well below to well above PM is evidence of a genetic relationship between these assemblages. This relationship along with apparent compositional layering and no crosscutting relations supports the cumulate model. If such a relationship were formed by a partial melting event, the close spatial relationship between fertile garnet-bearing assemblages and highly depleted dunites would imply unrealistically high temperature gradients so this can be ruled out. A post-depletion enrichment event is the presently accepted model and consistent the genetic relationship in terms of Fe, Ca, Na, Al, Ni, Cr, Co and Sc concentration, whole-rock Mg# and Cr#, REE and trace-element patterns. The apparent mixing trends may provide important implications for the origin of the melts that resulted in these trends. An internal origin of the melts can most likely be excluded and it can be assumed that these melts derived from a deeper level of the same or similar part of the SCLM as the depleted dunites. This further implies that all internal lithological elements in the peridotite at Almklovdalen have the same provenance. Comparison of the average concentrations in mantle xenoliths, lherzolites and dunite/harzburgites on an international scale revealed a strong similarity between mantle xenoliths from Greenland and the massive peridotites in WGR (Griffin et al., 2009). This explains the Laurentian provenance suggested by Beyer et al. (2004), the Proterozoic enrichment event suggested by Beyer et al (2006) and the Archean ages of the depleted protolith suggested Beyer et al. (2012). The compositional banding without crosscutting relation has to be explained by extensional ductile deformation pulling the dikes into alignment. Enrichment is no contradiction to the up-thrusting model of Cordellier et al. (1981) discussed above.

7.3 Uplift and retrogression

The layering of the fresh garnet pyroxenites and their retrograde equivalents at the field area near Helghornsvatnet raises the question of their relationship. From the structural data and field observations it is apparent that these elements are related by strain and share all deformation features. Their compositional genetic relationship and occurrence of both garnet and diopside prophyroblasts partly retrograded to clinochlore strongly indicate that the clinochlore-rich layers have simply been exposed to a higher degrees of alteration in hydrous conditions. All elements are not necessarily formed simultaneously and the Proterozoic ages related enrichment are all from relatively fresh garnet pyroxenites and garnet peridotites and the clinochlore bands/layers has not been dated. If the peridotite massif was part of the hanging wall during the Caledonian subduction event, it would be expected that the composition of the metasomatic fluids may have been changing over time. This could have resulted in a minor compositional diversity in the hydrated zones that further facilitated the variation in alteration. No large variation in the analytical results contradicts such variation but the results representing bulk-rock composition which may obscure compositional variations that changes physical properties and susceptibility to alteration. The close spatial close relationship between these elements also seems inconsistent with the nature of dike intrusions. It is unlikely that no irregularity or crosscutting relations would have occurred during such intrusion event. Dike swarms intruded by repetitive magma pulses would most likely have created a more complex pattern.

Alteration processes occurring during late stages of the Scandian phase was cause by silica-rich fluids. As the subducted slab of the Baltic continental crust was educted to shallower levels in the subduction zone, decompression melting in the felsic gneisses could generate such silica-rich fluids.

These fluids penetrated the outer rim of the peridotite massifs and percolated along fault systems. This caused the penetrative serpentinization of the contact zone and development of serpentine selvedges on fault planes within the entire peridotite massif. The penetrative serpentinization is restricted to the outer rim of the peridotite massif and along mesoscopic fault zones crosscutting the dominant foliation (Figure 6.2.2 and Figure 6.3.2). These faults can be interpreted as channels increasing permeability and connectivity and facilitation fluid percolation to the internal parts of the peridotite massif. The dominant foliation provided an internal slip system along which extensive faulting has occurred, which further increased the permeability and connectivity. An extensive fault and fracture system developed at distances > 5 cm apart, parallel to the dominant foliation, which further lowered the structural competence of the peridotite massif. Silica-rich fluids percolated along these fault and fracture plains accessing the entire peridotite massif. This is suggested to have caused the widespread internal occurrence of chlorite, serpentine and talcum. Minor concentrations of fibrous minerals also may have developed by this hydration and are restricted to this permeable system. Decreasing degrees of penetrative serpentinization towards the core of the peridotite indicate that the fluids concentrated along the contact of the peridotite, which still represents a highly permeable zone. Bands of chlorite developed by penetrative fluid percolation along the dominant foliation (Figure 6.1.2). Minor faulting and fracturing also developed locally in a more complex pattern, crosscutting the dominant foliation and minor rims of serpentine and talc are found on these fault and fracture planes. These systems show evidence of hydro-fracturing which generated veins of chlorite (Figure 6.1.3). The penetrative chloritization along the dominant foliation and veins of chlorite generated by hydro-fracturing illustrates that the fluids entered under relatively high pressure conditions. Rare euhedral to subhedral forsterite crystals indicate that faulting also occurred in the stability field of forsterite crystal growth (Figure 6.3.23). Crystalline forsterite occurs in pockets along faults parallel to the dominant foliation. Continuous hydration and cooling of the peridotite has partly retrograded these crystals to talc and serpentine.

The fault breccia located at the Gusdal mine shows evidence of carbonate mineralization indicating that the percolating fluids at some stage contained carbon dioxide (CO_2) (Figure 6.3.23). The brittle nature of the fault breccia and development of carbonate mineralization as rims on the surfaces of the fragments are interpreted as indication of low-pressure fluid percolation. No apparent faulting occurred in the gneiss, which is well exposed at this location. The fault breccia only affected the peridotite and ends abruptly at the contact against the gneiss. This can be explained by P-T conditions in which the felsic gneisses were still in the ductile regime and the peridotite was in the brittle regime. Feldspar is ductile above approximately 450-500°C, corresponding to approximately 20-30 km depth, and olivine is brittle below approximately 600°C, down to approximately 50 km (Fossen, 2016). These estimates are highly dependent on pressure and whether the deformation occurred in wet or dry conditions. Such brittle deformation in the serpentinized peridotite and ductile deformation in the gneiss correspond to depths of approximately 30-40 km and this represents late Scandian phase. Above 20 km depth the peridotite is in dry low P-T conditions and no significant mineralization.

8. Conclusions

- The orogenic peridotite massif at Almklovdalen represent well preserved SCLM which formed and provide unique possibilities for future geochemical research related to mantle processes. Field work conducted during this survey located one new lithological element, represented by sample JVS 218A and JVS 218B, which not have been found previously at any of the peridotites in WGR. Further research will be concentrated on this lithology and it will be analyzed for PGE (Platinum Group Elements).
- The compositional layering exposed at the selected field area near Helghornsvatnet differs from the volumetrically dominant dunite in the rest of the Almklovdalen peridotite due to layers of less depleted composition. The less depleted composition is represented by garnet-bearing assemblages and its retrograded equivalents. These assemblages provided rheological contrasts that governed the development of strain in this area. Kinematic indicators provided by the compositional layering allows for deformation features to be studied in the field. The same deformation processes probably affected the entire peridotite massif but developed a different strain geometry in the homogenous dunite due to the lack of rheological contrast. These deformation features is not detectable for field studies due to lack of such kinematic indicators.
- A genetic relationship between the depleted dunites, garnet-bearing assemblages and the clinochlore-rich layers is consistent with the mixing trends between whole-rock Mg-number, major-element oxides and Cr-number. The genetic relationship is further documented by mixing trends between whole-rock Mg-number and Ni, Cr, Co, Sc, Zr, Sr, La and Yb concentrations relative to primitive mantle. Such relationship is further documented by REE and trace-element patterns. Field observations of clinochlore-rich layers containing remains of un-altered diopside and garnets provide physical evidence that these assemblages represent retrograded equivalents of garnet pyroxenes and garnet peridotites.
- Garnet pyroxenites and garnet peridotites at the selected field area near Helghornsvatnet represent Proterozoic interaction between depleted Archean subcontinental mantle residues and fertile magmas. Two models for formation of these lithological elements are suggested: 1) Intrusions of basaltic dikes imposing enrichment on depleted mantle residues by metasomatic fluids followed by extensional deformation pulling the dikes and their enriched aureoles into alignment. 2) Accumulation of fertile magma-reservoirs within the depleted residue resulting fractional crystallization that developed compositional layering within the cumulates. The clinochlore layers/bands are the retrograded equivalents of the garnet-bearing assemblages.
- The dunites are depleted and the garnet-bearing assemblages are enriched relative to primitive mantle composition.
- Both emplacement models do appear to be credible according to field observations and data analyzed. The structural data can be applied to the sinking intrusion model as well as the up-thrusting model. Folds at the field area near Helghornsvatnet were generated by active folding during dominant N-S to NNW-SSE shortening in a plastic to ductile regime. Petrological analyses of lithological elements also provide evidence of a geological evolution which coincides with both models.

9. References

Andersen, T.B. and Austrheim, H., 2008. The Caledonian Infrastructure in the Fjord-ergion of Western Norway: With Special Emphasis on Formation and Exhumation of High-and Ultrahigh-pressure Rocks, Late-to Post-orogenic Tectonic Processes and Basin Formation. publisher not identified.

Andersen, T.B. and Jamtveit, B., 1990. Uplift of deep crust during orogenic extensional collapse: A model based on field studies in the Sogn-Sunnfjord Region of western Norway. Tectonics, 9(5): 1097-1111.

Austrheim, H., Corfu, F., Bryhni, I. and Andersen, T.B., 2003. The Proterozoic Hustad igneous complex: a low strain enclave with a key to the history of the Western Gneiss Region of Norway. Precambrian Research, 120(1): 149-175.

Barth, N.C., Hacker, B.R., Seward, G.G., Walsh, E.O., Young, D. and Johnston, S., 2010. Strain within the ultrahigh-pressure Western Gneiss region of Norway recorded by quartz CPOs. Geological Society, London, Special Publications, 335(1): 663-685.

Bernstein, S., Hanghøj, K., Kelemen, P.B. and Brooks, C.K., 2006. Ultra-depleted, shallow cratonic mantle beneath West Greenland: dunitic xenoliths from Ubekendt Ejland. Contributions to Mineralogy and Petrology, 152(3): 335-347.

Bernstein, S., Kelemen, P.B. and Brooks, C.K., 1998. Depleted spinel harzburgite xenoliths in Tertiary dykes from East Greenland: restites from high degree melting. Earth and Planetary Science Letters, 154(1): 221-235.

Bernstein, S., Kelemen, P.B. and Hanghøj, K., 2007. Consistent olivine Mg# in cratonic mantle reflects Archean mantle melting to the exhaustion of orthopyroxene. Geology, 35(5): 459-462.

Beyer, E.E., Brueckner, H.K., Griffin, W.L., O'Reilly, S.Y. and Graham, S., 2004. Archean mantle fragments in Proterozoic crust, Western Gneiss Region, Norway. Geology, 32(7): 609-612.

Beyer, E.E., Brueckner, H.K., Griffin, W.L. and O'Reilly, S.Y., 2012. Laurentian provenance of Archean mantle fragments in the Proterozoic Baltic crust of the Norwegian Caledonides. Journal of Petrology: egs019.

Beyer, E.E., Griffin, W.L. and O'REILLY, S.Y., 2006. Transformation of Archaean lithospheric mantle by refertilization: evidence from exposed peridotites in the Western Gneiss Region, Norway. Journal of Petrology, 47(8): 1611-1636.

Brueckner, H. and Medaris, L., 1998. A tale of two orogens: the contrasting TPt history and geochemical evolution of mantle in high-and ultrahigh-pressure metamorphic terranes of the Norwegian Caledonides and the Czech Variscides. Schweizerische Mineralogische und Petrographische Mitteilungen, 78(2): 293-307.

Brueckner, H.K., 1972. Interpretation of Rb-Sr ages from the Precambrian and Paleozoic rocks of southern Norway. American Journal of Science, 272(4): 334-358.

Brueckner, H.K., 1998. Sinking intrusion model for the emplacement of garnet-bearing peridotites into continent collision orogens. Geology, 26(7): 631-634.

Brueckner, H.K., Carswell, D.A. and Griffin, W.L., 2002. Paleozoic diamonds within a Precambrian peridotite lens in UHP gneisses of the Norwegian Caledonides. Earth and Planetary Science Letters, 203(3–4): 805-816.

Brueckner, H.K., Carswell, D.A., Griffin, W.L., Medaris Jr, L.G., Van Roermund, H.L.M. and Cuthbert, S.J., 2010. The mantle and crustal evolution of two garnet peridotite suites from the Western Gneiss Region, Norwegian Caledonides: An isotopic investigation. Lithos, 117(1–4): 1-19.

Carswell, D., 1968. Possible primary upper mantle peridotite in Norwegian basal gneiss. Lithos, 1(4): 322-355.

Carswell, D.A., 1981. Clarification of the petrology and occurrence of garnet lherzolites, garnet websterites and eclogite in the vicinity of Rødhaugn, Almklovdalen, West Norway. Norsk Geologisk Tidskrift, 61: 249-260.

Cawood, P.A., McCausland, P.J. and Dunning, G.R., 2001. Opening Iapetus: constraints from the Laurentian margin in Newfoundland. Geological Society of America Bulletin, 113(4): 443-453.
Chauvet, A. and Seranne, M., 1989. Microtectonic evidence of Devonian extensional westward shearing in Southwest Norway. The Caledonide Geology of Scandinavia: 245-254.
Cordellier, F., Boudier, F. and Boullier, A., 1981. Structural study of the Almklovdalen peridotite massif (southern Norway). Tectonophysics, 77(3): 257-281.
Cuthbert, S., Harvey, M. and Carswell, D., 1983. A tectonic model for the metamorphic evolution of the Basal Gneiss Complex, Western South Norway. Journal of metamorphic Geology, 1(1): 63-90.
Davidson, C.F., 1943. The Archaean rocks of the Rodil district. South Harris, Outer Hebrides.
Davidson, C.F., 1944. II.—The Archæan Rocks of the Rodil District, South Harris, Outer Hebrides. Transactions of the Royal Society of Edinburgh, 61(01): 71-112.
Dobrzhinetskaya, L.F., Eide, E.A., Larsen, R.B., Sturt, B.A., Trønnes, R.G., Smith, D.C., Taylor, W.R. and Posukhova, T.V., 1995. Microdiamond in high-grade metamorphic rocks of the Western Gneiss region, Norway. Geology, 23(7): 597-600.
Eskola, P., 1921. On the eclogites of Norway. Рипол Классик.
Finstadt, K. and Heier, K., 1972. The distribution of some elements between the metal and silicate phases obtained in a smelting reduction process of dunite from Almklovdalen, West Norway. Earth and Planetary Science Letters, 16(2): 209-212.
Fossen, H., 2010. Extensional tectonics in the North Atlantic Caledonides: a regional view. Geological Society, London, Special Publications, 335(1): 767-793.
Fossen, H., 2016. Structural geology. Cambridge University Press.
Gautneb, H. and Flem, B., 2001. Karakterisering av olivin med hovedvekt på gitterbundne elementer.
Gordon, S.M., Whitney, D.L., Teyssier, C., Fossen, H. and Kylander-Clark, A., 2016. Geochronology and geochemistry of zircon from the northern Western Gneiss Region: Insights into the Caledonian tectonic history of western Norway. Lithos, 246: 134-148.
Griffin, W., O'Reilly, S.Y., Ryan, C., Gaul, O. and Ionov, D., 1998. Secular variation in the composition of subcontinental lithospheric mantle: geophysical and geodynamic implications. Structure and evolution of the Australian continent: 1-26.
Griffin, W., O'Reilly, S. and Ryan, C., 1999. The composition and origin of sub-continental lithospheric mantle, Mantle petrology: field observations and high-pressure experimentation: a tribute to Francis R.(Joe) Boyd. The Geochemical Society Houston, pp. 13-45.
Griffin, W., O'reilly, S.Y., Afonso, J.C. and Begg, G., 2009. The composition and evolution of lithospheric mantle: a re-evaluation and its tectonic implications. Journal of Petrology, 50(7): 1185-1204.
Griffin, W. and Qvale, H., 1985. Superferrian eclogites and the crustal origin of garnet peridotites, Almklovdalen, Norway. The Caledonide orogen-Scandinavia and related areas: Chichester, Wiley: 803-812.
Grønlie, G. and Rost, F., 1974. Gravity investigation and geological interpretation of the ultramafite complex of Åheim, Sunnmøre, western Norway. Norsk Geologisk Tidsskrift, 54: 367-373.
Hacker, B.R., Andersen, T.B., Johnston, S., Kylander-Clark, A.R., Peterman, E.M., Walsh, E.O. and Young, D., 2010. High-temperature deformation during continental-margin subduction & exhumation: The ultrahigh-pressure Western Gneiss Region of Norway. Tectonophysics, 480(1): 149-171.
Hofmann, A.W., 1988. Chemical differentiation of the Earth: the relationship between mantle, continental crust, and oceanic crust. Earth and Planetary Science Letters, 90(3): 297-314.
Hofmann, A.W. and White, W.M., 1983. Ba, Rb and Cs in the Earth's mantle. Zeitschrift für Naturforschung A, 38(2): 256-266.
Jacobsen, S. and Wasserburg, G., 1980. Nd and Sr isotopes of the Norwegian garnet peridotites and eclogites. Eos, 61: 389.
Jamtveit, B., Carswell, D. and Mearns, E., 1991. Chronology of the high-pressure metamorphism of Norwegian garnet peridotites/pyroxenites. Journal of metamorphic Geology, 9(2): 125-139.

Kostenko, O., Jamtveit, B., Austrheim, H., Pollok, K. and Putnis, C., 2002. The mechanism of fluid infiltration in peridotites at Almklovdalen, western Norway. Geofluids, 2(3): 203-215.
Labrousse, L., Jolivet, L., Agard, P., Hébert, R. and Andersen, T., 2002. Crustal-scale boudinage and migmatization of gneiss during their exhumation in the UHP province of western Norway. Terra Nova, 14(4): 263-270.
Lappin, M., 1966. The field relationships of basic and ultrabasic masses in the basal gneiss complex of Stadlandet and Almklovdalen, Nordfjord, southwestern Norway. Norsk Geologisk Tidsskrift, 46(4): 439-496.
Lappin, M., 1974. Eclogites from the Sunndal-Grubse ultramafic mass, Almklovdalen, Norway and the TP history of the Almklovdalen masses. Journal of Petrology, 15(3): 567-601.
Li, Z., Li, X., Kinny, P. and Wang, J., 1999. The breakup of Rodinia: did it start with a mantle plume beneath South China? Earth and Planetary Science Letters, 173(3): 171-181.
McDonough, W.F. and Sun, S.-S., 1995. The composition of the Earth. Chemical geology, 120(3): 223-253.
Mearns, E.W., 1986. Sm・Nd ages for Norwegian garnet peridotite. Lithos, 19(3): 269-278.
Medaris Jr, L., 1984. A geothermobarometric investigation of garnet peridotites in the Western Gneiss Region of Norway. Contributions to Mineralogy and Petrology, 87(1): 72-86.
Mercy, E. and O'Hara, M., 1965a. Chemistry of some garnet-bearing rocks from south Norwegian peridotites. Norsk Geologisk Tidsskrift, 45: 323-332.
Mercy, E. and O'Hara, M., 1965b. Olivines and orthopyroxenes from garnetiferous peridotites and related rocks. Nor Geol Tidsskr, 45: 457-461.
Norton, M., 1987. The Nordfjord-Sogn Detachment, W. Norway. Norsk Geologisk Tidsskrift, 67(2): 93-106.
Osland, R., 1997. Modelling of variations in Norwegian olivine deposits. Doktor Ingeniør Thesis, Norwegian Univ. of Science and Technology.
Palme, H. and O'Neill, H., 2003. Treatise on Geochemistry, Vol. 2. The Mantle and Core.
Piñán Llamas, A., Andersson, J., Möller, C., Johansson, L. and Hansen, E., 2015. Polyphasal foreland-vergent deformation in a deep section of the 1 Ga Sveconorwegian orogen. Precambrian Research, 265: 121-149.
Pisarevsky, S.A., Murphy, J.B., Cawood, P.A. and Collins, A.S., 2008. Late Neoproterozoic and Early Cambrian palaeogeography: models and problems. Geological Society, London, Special Publications, 294(1): 9-31.
Ramberg, I.B., Nøttvedt, A., Bryhni, I., Solli, A. and Nordgulen, Ø., 2006. Landet blir til: Norges geologi. Norsk geologisk forening.
Roberts, D. and Gee, D., 1985. An introduction to the structure of the Scandinavian Caledonides. The Caledonide orogen: Scandinavia and related areas. The Caledonide Orogen: Scandinavia and Related Areas (DG Gee & BA Sturt, eds.). Wiley, Chichester, UK (55-68).
Robinson, P., 1995. Extension of Trollheimen tectono-stratigraphic sequence in deep synclines near Molde and Brativag, Western Gneiss Region, southern Norway. Norsk Geologisk Tidsskrift, 75(4): 181-197.
Roermund, V., 1998. Ultra-high pressure (P> 6 GPa) garnet peridotites in Western Norway: exhumation of mantle rocks from> 185 km depth. Terra Nova, 10(6): 295-301.
Roffeis, C. and Corfu, F., 2014. Caledonian nappes of southern Norway and their correlation with Sveconorwegian basement domains. Geological Society, London, Special Publications, 390(1): 193-221.
Root, D., Hacker, B., Gans, P., Ducea, M.N., Eide, E. and Mosenfelder, J., 2005. Discrete ultrahigh-pressure domains in the Western Gneiss Region, Norway: implications for formation and exhumation. Journal of Metamorphic Geology, 23(1): 45-61.
Root, D.B., Hacker, B., Mattinson, J. and Wooden, J.L., 2004. Zircon geochronology and ca. 400 Ma exhumation of Norwegian ultrahigh-pressure rocks: an ion microprobe and chemical abrasion study. Earth and Planetary Science Letters, 228(3): 325-341.

Seljebotn, J.V. and Soldal, J., 2014. Report from geological mapping of Gusdalen mine at Åheim, Norway.
SkÅr, Ø. and Pedersen, R.B., 2003. Relations between granitoid magmatism and migmatization: U–Pb geochronological evidence from the Western Gneiss Complex, Norway. Journal of the Geological Society, 160(6): 935-946.
Slagstad, T., Davidsen, B. and Daly, J.S., 2011. Age and composition of crystalline basement rocks on the Norwegian continental margin: offshore extension and continuity of the Caledonian–Appalachian orogenic belt. Journal of the Geological Society, 168(5): 1167-1185.
Spengler, D., Brueckner, H.K., van Roermund, H.L., Drury, M.R. and Mason, P.R., 2009. Long-lived, cold burial of Baltica to 200 km depth. Earth and Planetary Science Letters, 281(1): 27-35.
Sun, S.-S. and McDonough, W., 1989. Chemical and isotopic systematics of oceanic basalts: implications for mantle composition and processes. Geological Society, London, Special Publications, 42(1): 313-345.
Terry, M.P. and Robinson, P., 2003. Evolution of amphibolite-facies structural features and boundary conditions for deformation during exhumation of high-and ultrahigh-pressure rocks, Nordøyane, Western Gneiss Region, Norway. Tectonics, 22(4).
Tucker, R., Krogh, T. and Råheim, A., 1990. Proterozoic evolution and age-province boundaries in the central part of the Western Gneiss Region, Norway: Results of U-Pb dating of accessory minerals from Trondheimsfjord to Geiranger. Mid-Proterozoic Laurentia-Baltica, 38: 149-173.
Tucker, R., Råheim, A., Krogh, T. and Corfu, F., 1987. Uranium-lead zircon and titanite ages from the northern portion of the Western Gneiss Region, south-central Norway. Earth and Planetary Science Letters, 81(2-3): 203-211.
Tucker, R.D., Robinson, P., Solli, A., Gee, D.G., Thorsnes, T., Krogh, T.E., Nordgulen, Ø. and Bickford, M., 2004. Thrusting and extension in the Scandian hinterland, Norway: new U-Pb ages and tectonostratigraphic evidence. American Journal of Science, 304(6): 477-532.
van Roermund, H., 2009. Mantle-wedge garnet peridotites from the northernmost ultra-high pressure domain of the Western Gneiss Region, SW Norway. European Journal of Mineralogy, 21(6): 1085-1096.
Van Roermund, H., Drury, M., Barnhoorn, A. and De Ronde, A., 2001. Relict majoritic garnet microstructures from ultra-deep orogenic peridotites in western Norway. Journal of Petrology, 42(1): 117-130.
van Roermund, H.L., Carswell, D.A., Drury, M.R. and Heijboer, T.C., 2002. Microdiamonds in a megacrystic garnet websterite pod from Bardane on the island of Fjørtoft, western Norway: Evidence for diamond formation in mantle rocks during deep continental subduction. Geology, 30(11): 959-962.
Vrijmoed, J., Van Roermund, H. and Davies, G., 2006. Evidence for diamond-grade ultra-high pressure metamorphism and fluid interaction in the Svartberget Fe–Ti garnet peridotite–websterite body, Western Gneiss Region, Norway. Mineralogy and Petrology, 88(1-2): 381-405.
Wain, A., 1997. New evidence for coesite in eclogite and gneisses: Defining an ultrahigh-pressure province in the Western Gneiss region of Norway. Geology, 25(10): 927-930.
Walsh, E.O., Hacker, B.R., Gans, P.B., Grove, M. and Gehrels, G., 2007. Protolith ages and exhumation histories of (ultra) high-pressure rocks across the Western Gneiss Region, Norway. Geological Society of America Bulletin, 119(3-4): 289-301.
Wang, Q., XIA, Q.K., O'REILLY, S., Griffin, W., Beyer, E. and Brueckner, H.K., 2013. Pressure-and stress-induced fabric transition in olivine from peridotites in the Western Gneiss Region (Norway): implications for mantle seismic anisotropy. Journal of Metamorphic Geology, 31(1): 93-111.
Young, D.J., Hacker, B.R., Andersen, T.B. and Corfu, F., 2007. Prograde amphibolite facies to ultrahigh-pressure transition along Nordfjord, western Norway: Implications for exhumation tectonics. Tectonics, 26(1).

10. References to web pages

http://www.dplot.com/mt/mt-search.cgi?blog_id=1&tag=triangle%20plot&limit=20. Accessed: 15.12.2016

http://geo.ngu.no/kart/berggrunn/, Accessed: 18.09.2015

http://geo.ngu.no/kart/berggrunn/, Accessed: 13.10.2015

http://geo.ngu.no/kart/berggrunn/, Accessed: 17.10.2015

(http://www.norgeskart.no/#4/502779/7157838, accessed: 18.09.2015

(http://www.norgeskart.no/#15/9210/6910009/-land/+flybilder, accessed: 20.03.2016).

(http://www.norgeskart.no/#8/39258/6913899, accessed: 22.10.2015).

11. Appendix 1

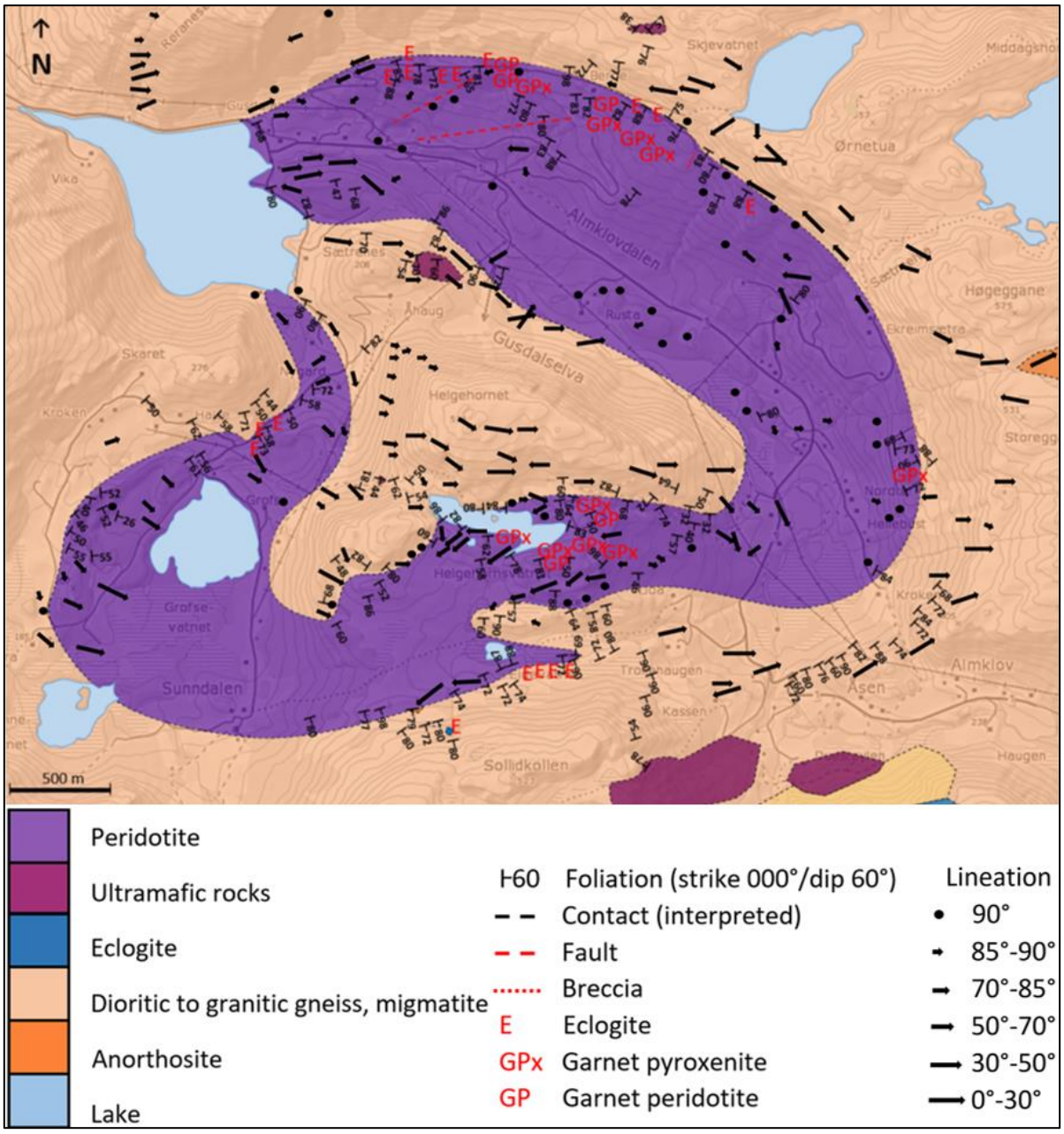

Figure 11.1: Complete geological map of the Almklovdalen peridotite.